Measurements of the form factors in $K^+ \rightarrow \pi^0 \mu^+ \nu$ decay

Youichi Igarashi

1 9 9 7

Measurements of the form factors
in $K^+ \to \pi^0 \mu^+ \nu$ decay

Youichi IGARASHI

A dissertation submitted to the Doctoral Program in Physics,
the University of Tsukuba in partial fulfillment of requirements
for the degree of Doctor of Philosophy (in Science)

September, 1997

Abstract

The form factors of $K_{\mu 3}$ decay $K^+ \rightarrow \pi^0 \mu^+ \nu$ have been obtained by measuring its kinematics distribution. The form factors are the parameters which characterize the behavior of kaon weak decay. On the theoretical side, the kaon is a simple system which is researched by QCD. The measurement of form factors can test models realizing low energy long-distance QCD. In this connection, the Chiral Perturbation Theory(CHPT) which is one of the calculation schemes of low energy QCD has made the prediction from first principles (thus model independent) of the slope of kaon form factors.

In order to obtain the kaon form factors, the distribution of the kinematics was used. $K_{\mu 3}$ kinematics was decided by the energies of π^0 and μ^+. Both of the measured energies were plotted as a two dimensional histogram, and the values of form factor were obtained by fitting this histogram. The measurement was performed using stopped K^+ method. A super-conducting toroidal spectrometer in conjunction with a CsI(Tl) photon detector was used for the experiment at K5 beam line of KEK-PS proton synchrotron. The energy of π^0 was measured by the CsI(Tl) photon detector which was constructed with 768 modules, and the energy of μ^+ was measured by the spectrometer which was constructed with a Toroidal Magnet and three MWPCs.

The obtained results were

$$\lambda_+ = 0.034 \pm 0.007(sta) \pm 0.012(sys)$$

and

$$\xi(0) = -0.40 \pm 0.08(sta) \pm 0.07(sys)$$

where sta means a statistics error and sys means a systematic error. These values are consistent with the results of previous experiments within errors. And the present measurement was most precise one among so far   performed experiments. They agree with the prediction of CHPT.

Contents

Chapter 1

Introduction

1.1 Physics Motivation

There are several good reasons motivating the study of K meson decays within the standard model. They are

- to do high precision experiments at rare K decays to obtain the fundamental information of the Electroweak interaction.

- to test Quantum Chromo Dynamics (QCD) at low energies.

The understanding of QCD effects at K decays is significantly important not only for its own importance or interest but also for extracting the genuine information of the electroweak interaction, since in most of K decays the QCD contributions, which is called as "long distance contribution" would mask the electroweak information (which is called, in contrast, "short distance contribution".) Also the study of QCD at K decays would give unique features, as explained below.

1.2 QCD at very low energy

The study of QCD can be divided into three regions of energy. We are all aware of the applications of perturbative QCD to the high energy region. As one comes down in energy, we enter a region where perturbative QCD is no longer applicable. Here we do not know how to calculate (apart from the lattice computer calculations), and we are reduced to making models such as quark models, Skyrme models, ... etc. There are not good approximation in the sense of predicting powers. However, at very low energy, say $E \leq 1$ GeV or so, we again enter a region where a controlled approximation is possible, using symmetry, which is called "chiral symmetry".

1.3 What is Chiral Symmetry ?

Suppose the case that the u, d, s quarks are massless. For each quark, there is a left-handed helicity state (spin antiparallel to the momentum) and a right-handed helicity state. QCD

interactions are the same for left and right helicity and do not flip helicity. Under these conditions left handed massless particle will always stay left-handed and right-handed will stay right-handed. Since each flavor is massless and has the same QCD coupling, there exists a separate flavor $SU(3)$ invariance in each world. It is called $SU(3)_L \times SU(3)_R$. This is the chiral symmetry.

Now consider the quark masses. It is clear that we can not maintain the separate left-handed and right-handed invariance. If one has a massive left-handed particle, one can always boost to the frame moving with other direction, such that left-handed particle is now right-handed. Now we can not separate the left-handed and right-handed. However, if the mass is small, the original $SU(3)_L \times SU(3)_R$ symmetry could also be an approximate symmetry, and the mass could be treated as a perturbation. This is a main idea of "Chiral Perturbation Theory (CHPT)".

CHPT is one of the gauge theory, based on the spontaneous symmetry breaking. It is known that if the spontaneous symmetry breaking occurs (namely, the real vacuum is not the potential minimum), it produces the massless Goldstone bosons. In CHPT, the Goldstone bosons appearing from spontaneous $SU(3)$ symmetry breaking are pseudo-scalar mesons, like πs, Ks and η.

CHPT is a theory to use the effective chiral Lagrangian directly at the level of pseudo-scalar mesons. Since it is an effective theory, it introduces new coupling constants at each order of the expansion of mass or four-momentum transfer squared. So, it is a non-renomalizable quantum field theory. CHPT is, however, in a certain sense, the standard model at the mesonic level. Once the coupling constants are determined experimentally, it has strong predictive powers. If any discrepancies between CHPT and the experimental results appear, they imply at least possible consequences of new physics beyond the standard model.

1.4   Why K decays ?

The reason why the K decays provide the best testing grounds of CHPT is as follows;

- K decays involved only pseudo-scalar mesons or leptons, and no baryons (which have masses above the Λ_{QCD}).

- Typical momentum transfer squre is smaller than $\Lambda_{QCD} \sim 1$ GeV.

The effective Lagrangian is expanded in terms of the momentum transfer squre, p^2. In the effective Lagrangian of $O(p^4)$, there are 12 effective coupling constants, which are refered as $L_1, L_2, ...L_{12}$. They are determined experimentally, as shown in Table 1.1.

Now it is interesting to know which of the low-energy couplings occurs in the matrix elements for the semileptonic kaon decays. This information is given in Table 1.2.

1.5 K_{l3} Decays

In the present study, the semileptonic K decays are chosen to test CHPT. The decay mode considered here is

Table 1.1: Renormalized phenomenological coupling constants and source for them.

coupling constant	source
L_1	K_{e4}, $\pi\pi \to \pi\pi$
L_2	K_{e4}, $\pi\pi \to \pi\pi$
L_3	K_{e4}, $\pi\pi \to \pi\pi$
L_4	Zweig rule
L_5	F_K, F_π
L_6	Zweig rule
L_7	Gell-Mann-Okubo, L_5, L_8,
L_8	$M_{K^0} - M_{K^+}$
L_9	$< r^2 >_{em}^\pi$
L_{10}	$\pi \to e\nu\gamma$

Table 1.2: Occurrence of the low-energy coupling constants L_i in the semileptonic kaon decays

	L_1	L_2	L_3	L_4	L_5	L_9	$L_9 + L_{10}$
$K \to l\nu\gamma$							X
$K \to l\nu l\bar{l}$						X	X
$K \to \pi l\nu$						X	
$K \to \pi l\nu\gamma$						X	X
$K^+ \to \pi^+\pi^- e^+\nu$	X	X	X	X	X	X	
$K^+ \to \pi^0\pi^0 e^+\nu$	X	X	X	X	X	X	
$K^0 \to \pi^0\pi^- e^+\nu$			X		X	X	

$$K^+ \to \pi^0 \mu^+ \nu \quad (K_{\mu 3}) \tag{1.1}$$

As shown in Table 1.2, it is sensitive to the coupling constant L_9.

1.5.1 Matrix elements and kinematics of $K_{\mu 3}$ decay

Assuming that only the $V - A$ interaction contributes to the decay $K^+ \to \pi^0 l \nu$, its matrix element can be written as

$$
\begin{aligned}
M \quad &\propto \quad [f_+(q^2)(P_K + P_{\pi^0}) + f_-(q^2)(P_K - P_{\pi^0})][\bar{u}_l \gamma_\lambda (1 - \gamma_5) u_\nu] \tag{1.2} \\
&= \quad f_+(q^2)(P_K + P_{\pi^0})\bar{u}_l \gamma_\lambda (1 - \gamma_5) u_\nu + f_-(q^2) m_l \bar{u}_\mu (1 - \gamma_5) u_\nu \tag{1.3}
\end{aligned}
$$

where $f_+(q^2)$ and $f_-(q^2)$ are dimensionless form factors of K_{l3} as a function of momentum transfer squared q^2. They are assumed to be given as $f_\pm(q^2) = f_\pm(0)[1 + \lambda_\pm(q/m_\pi)^2]$. P_K and P_π are the four momenta of K^+ and π^0, respectively. Eq.(1.2) is obtained by using the momentum conservation relation of $P_K = P_{\pi^0} + P_{l+} + P_\nu$ and the Dirac equation.

1.5.2 Decay rate

The Dalitz distribution of K_{l3} is given as [Par96]

$$\rho(E_l, E_{\pi^0}) \propto f_+(q^2)^2 [A + B\xi(q^2) + C\xi(q^2)^2] \tag{1.4}$$

where

$$
\begin{aligned}
\xi(q^2) \quad &= \quad f_-(q^2)/f_+(q^2), \tag{1.5} \\
A \quad &= \quad m_K(2E_l E_\nu - m_K E'_{\pi^0}) + m_l^2(E'_{\pi^0}/4 - E_\nu), \tag{1.6} \\
B \quad &= \quad m_l^2(E_\nu - E'_{\pi^0}/2), \tag{1.7} \\
C \quad &= \quad \frac{1}{4} m_l^2 E'_{\pi^0}, \tag{1.8} \\
E'_{\pi^0} \quad &= \quad (m_K^2 + m_\pi^2 - m_l^2)/(2m_K) - E_{\pi^0}. \tag{1.9}
\end{aligned}
$$

E_{π^0}, E_l, and E_ν are energies of pion, lepton and neutrino, respectively, while m_K, m_l, and m_ν are masses of K^+, lepton and π^0, respectively. A typical Dalitz density plot of $K_{\mu 3}$ obtained from Eq.(1.4) is shown in Fig.1.1.

If we would include the exotic interactions such as the tensor and the scalar coupling, they can contribute to the hadronic current of the K_{l3} matrix element. Thus, we get the following matrix element [Pai57, Mac62, Par96].

$$
\begin{aligned}
M \quad \propto \quad &[f_+(q^2)(P_K + P_{\pi^0}) + f_-(q^2)(P_K - P_{\pi^0})][\bar{u}_l \gamma_\lambda (1 - \gamma_5) u_\nu] \tag{1.10} \\
+ \quad &2m_K f_S \bar{u}_l (1 - \gamma_5) u_\nu \\
+ \quad &(2f_T/m_K)(P_K)_\lambda (P_{\pi^0})_\mu \bar{u}_l \sigma_{\lambda\mu} (1 - \gamma_5) u_\nu
\end{aligned}
$$

where f_S and f_T are the scalar and tensor form factors, respectively.
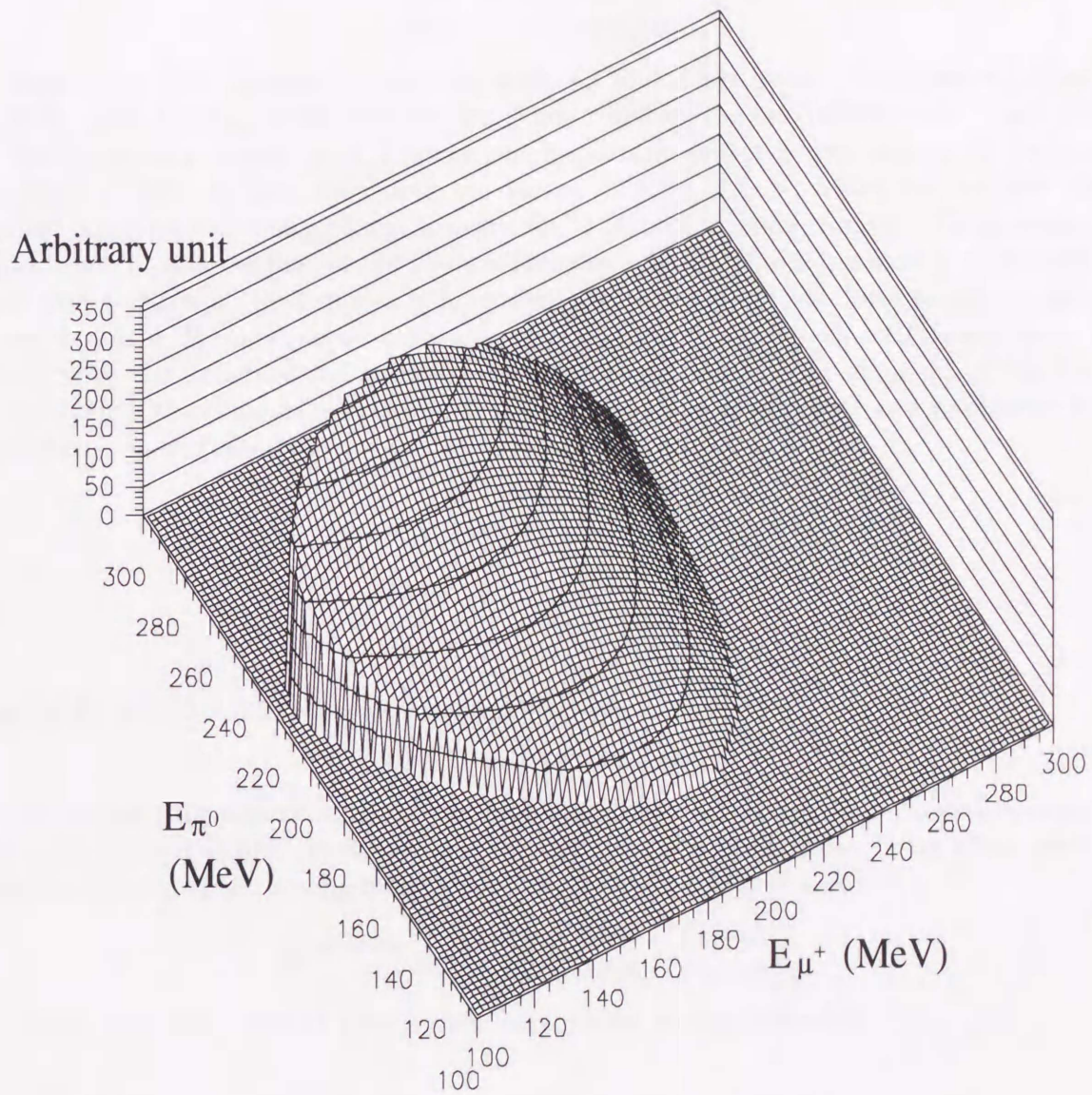
Figure 1.1: The Dalitz distribution obtained by assuming the $V - A$ interaction.

1.5.3 $\lambda_+, \xi(0)$ parameterization

Most $K_{\mu 3}$ data are adequately described by Eq.(1.11) for f_+ and a constant $f_-(i.e.\lambda_- = 0)$.

$$f_\pm = f_\pm(0)[1 + \lambda_\pm(t/m_\pi^2)]. \qquad (1.11)$$

Analysis of $K_{\mu 3}$ data often introduce the ratio of the two form factors.

$$\xi(t) = f_-(t)/f_+(t), \qquad (1.12)$$
$$\xi(0) = f_-(0)/f_+(0). \qquad (1.13)$$

Assuming time reversal invariance, both $f_\pm$ and ξ are real. Furthermore, usually $\lambda_- = 0$. Then the $K_{\mu 3}$ decay distribution is described by the two parameters λ_+ and $\xi(0)$.

In the physics related to $K_{\mu 3}$ decay, one important aspect is represented by the measurement of form factors describing the vertex $< \pi|\bar{u}\gamma_\mu s|K >$, which can severely test models realizing low energy long-distance QCD [Gas85, Don89, Sha90]. Of paramount importance in this context is the Callan-Treiman relation [Cal66], which is a prediction from first principles (thus model independent) of the slope of the form factor, in terms of the π and K leptonic decay constants (F_K, F_π) which have been well established. In detail, with the experimental value of the ratio F_K/F_π and of the slope λ_+ of the form factor $f_+(q^2)$, the slope parameter λ_0 of K_{l3} form factor was obtained as a parameter free prediction. λ_0 is defined as

$$\lambda_0 = \lambda_+ + a\xi(0),$$
$$a = \frac{m_\pi^2}{(m_K^2 - m_\pi^2)}. $$
$$(1.14)$$

For $F_k/F_\pi = 1.22 \pm 0.01$, the prediction is [Gas85]

$$\lambda_0^{theory} = 0.017 \pm 0.004, \qquad (1.15)$$

which is in nice agreement with the old high-statistics SLAC experiment [Don74], reporting $\lambda_0 = 0.019 \pm 0.004$. However, the present situation is far from being clear, as one observes discrepancies among more recent experimental data [Par96],

$$\lambda_0^{experiment} = \begin{cases} 0.004 \pm 0.007, & from K_{\mu 3}^+ \\ 0.025 \pm 0.006, & from K_{\mu 3}^0 \end{cases}$$

Thus, from this point of view, a new experiment is very desirable.

1.6 Measurement of the $K_{\mu 3}$ form factors

These form factors can be determined by the following three different methods.

A) studying the Dalitz plot or the pion spectrum of $K_{\mu 3}$ decay.

B) measuring the $K_{\mu 3}/K_{e3}$ branching ratio and comparing it with the theoretical ratio.

C) measuring the muon polarization in $K_{\mu 3}$ decay.

The present study has been performed by using Method A.

1.7 Previous measurement

The most precise values of the $K_{\mu 3}$ form factors obtained so far from the single experiment are as follows.

$$\lambda_+ = 0.050 \pm 0.013$$
$$\xi(0) = -0.57 \pm 0.24$$

The value of λ_+ is measured by Whitman's experiment in 1980 [Whi80]. And the value of $\xi(0)$ is measured by Merian's experiment in 1974 [Mer74].

The world averaged values quoted by the Particle Data Group are as follows [Par96].

$$\lambda_+ = 0.033 \pm 0.008,$$
$$\xi(0) = -0.35 \pm 0.015.$$

Chapter 2

Experimental Setup

In order to make a precise measurement of the $K_{\mu 3}$ Dalitz plot which is given by a correlation between energies of μ^+ and π^0, a spectrometer and a photon detector were used. The spectrometer was constructed with a super-conducting toroidal magnet, multi-wire proportional chambers and a ring-shape plastic scintillating counter system. The momentum of μ^+ was measured by the spectrometer. The photon detector was made of Tl doped CsI scintillators. The π^0 decays into two γ's with a life time of 8.4×10^{-17} sec. The energy of π^0 were measured by detecting both photons with use of $CsI(Tl)$ photon calorimeters.

One of the advantages in this experiment is to use K^+ decay at rest. The use of stopped K^+ decay means that we can use the measured energy of μ^+ (E_{μ^+}) and π^0 (E_{π^0}) without any conversion of the coordinate system. In the case of the in-flight experiment, K^+ momentum must be determined precisely for the determination of the μ^+ and π^0 energies. Therefore finite emittance and momentum dispersion of the beam would deform the Dalitz plot. On the other hand, we can deal with perfectly isotropic decays without any influence from the K^+ beam history.

The experiment were performed at the K5 beam channel of 12GeV proton synchrotron in High Energy Accelerator Research Organization (KEK-PS). Overview of this experiment is shown in Fig.2.1.

In this chapter, the experimental details will be shown.

2.1   KEK-PS Proton Synchrotron

A schematic view of the KEK-PS 12 GeV Proton Synchrotron is shown in Fig. 2.2. H^-ions were extracted from the ion source at a rate of 20 Hz and were accelerated up to 750 keV in the Pre-Injector which is a Cokcroft-Walton accelerator. Then they were accelerated up to 40 MeV by the Proton Linac which is an Alvarez-type linac. And then, they were injected into a Booster Synchrotron which is operated in 20Hz rapid cycle. Accelerated up to 500 MeV in the Booster Synchrotron, the H^-ions were injected into the main ring, i.e. the 12 GeV Proton Synchrotron, through a thin carbon foil which strips off the electrons of the H^-ions. The 12 GeV proton beam was then introduced to experimental halls through the slow extraction lines. Normally, we used a 3 sec repetition cycle with a pulse duration of 0.7 sec. A typical proton beam intensity was 2×10^{12}
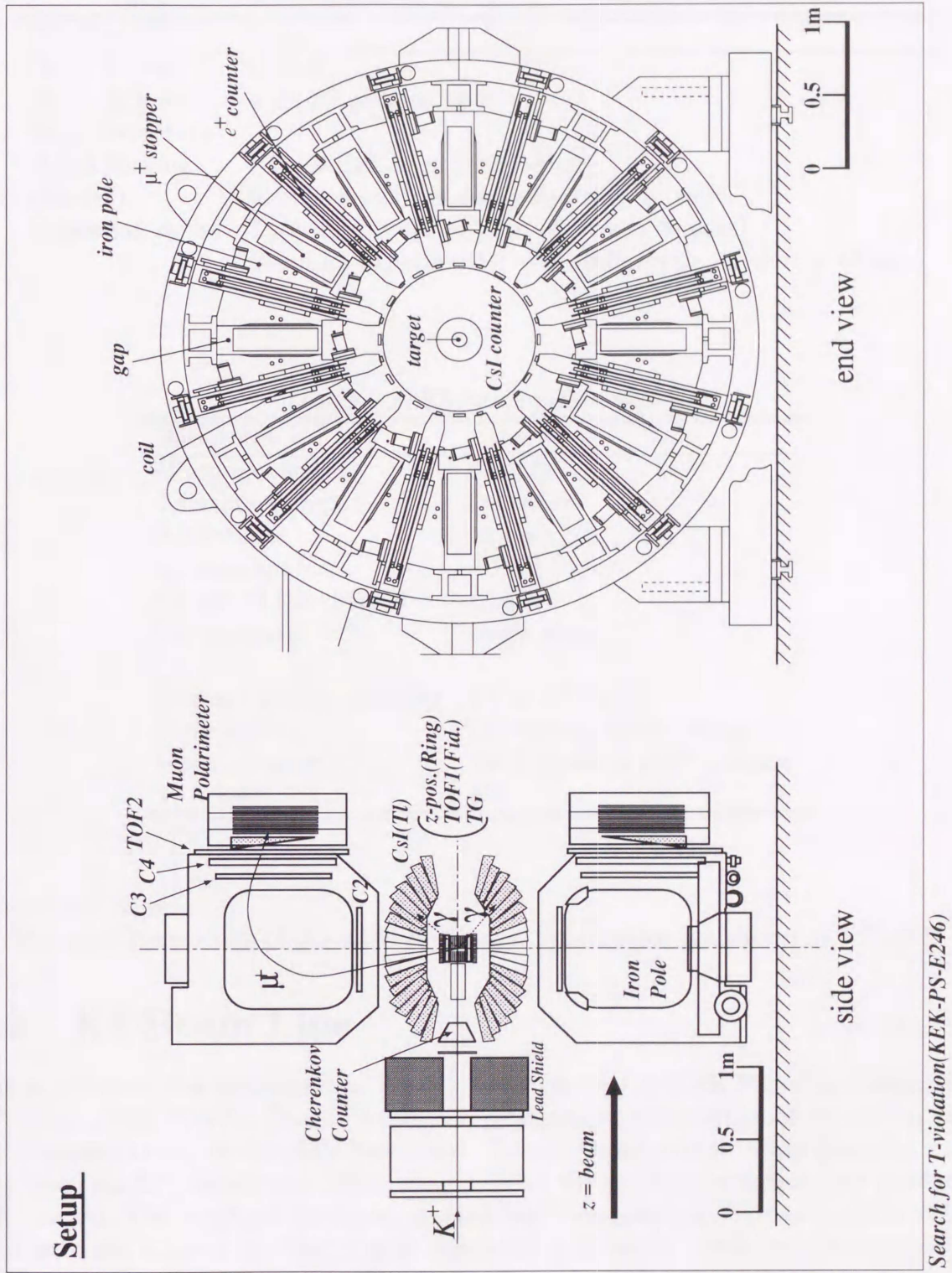
Figure 2.1: The experimental set up of the measurement of $K\mu_3$ decay

Table 2.1: Main parameters of the KEK-PS Proton Synchrotron

Parameter	Value
Beam Energy	$12 GeV$
Beam Intensity	4×10^{12} protons/spill
Beam Structure	
Beam Sharing	EP1(N-Hall) v.s. EP2(E-Hall)
(Modes)	Simultaneous/pulse to pulse/shift to shift
Operation cycles	Typically 12 cycles/year, (1cycle = 3weeks)
	Beam for experiments: $\sim$40 shifts/cycle, (1 shift = 8hours)

Table 2.2: K5 beam parameters

Parameter	Value
Beam momentum	660 MeV/c
Extraction angle	0 degree
Acceptance	10 mstr
Momentum bite	$\pm 2.5\%$
Length of the channel	12.3 m
DC separator	single stage
Primary proton intensity	2.7×10^{12}/pulse
Duty factor	0.7 sec-on/ 3.0 sec-repetition
Kaon intensity	100 k incident /10^{12} protons
π/K ratio	6:1

protons per pulse.

The main parameters of the KEK-PS Proton Synchrotron are shown in Table2.1.

2.2 K5 Beam Line

The experiment was performed at the K5 beam channel of KEK-PS using a separated K^+ beam of 660 MeV/c. The K^+ beam was produced by the reaction of the proton with the platinum target on the EP1 beam-line. The extracted proton beam from the main ring went via EP1 beam line. Then, they collided the production target, and produced a K^+ beam. The length of the beam channel had been made as short as possible (12m) with only one stage of an electrostatic separator in order to increase the intensity of K^+ beam. The channel has a large acceptance at the 0 degree extraction angle with a momentum bite of $\Delta p/p = \pm 2.5\%$. Basic parameters of the beam are summarized in Table 2.2. A schematic view of the K5 beam line is shown in Fig.2.3.

N - Hall
(North Counter Hall)

Slow extraction EP1

To BSF
(Booster Science Facility)

12-GeV Proton Synchrotron

Intensity : 4×10^{12} protons/spill
Repetition cycle : 4.0 s
Spill duration : 2.0 s

Slow extraction EP2

E - Hall
(East Counter Hall)

Booster Synchrotron
500 MeV   10 µA
Rapid cycle synchrotron

Proton Linac
40 MeV   10 µA
Alvarez-type linac

Pre-Injector
750 keV
Cockcroft-Walton

0   50 m

Figure 2.2: Layout of the accelerator complex of the KEK 12 GeV Proton Synchrotron. The K5 beam line is located in the North Counter Hall.
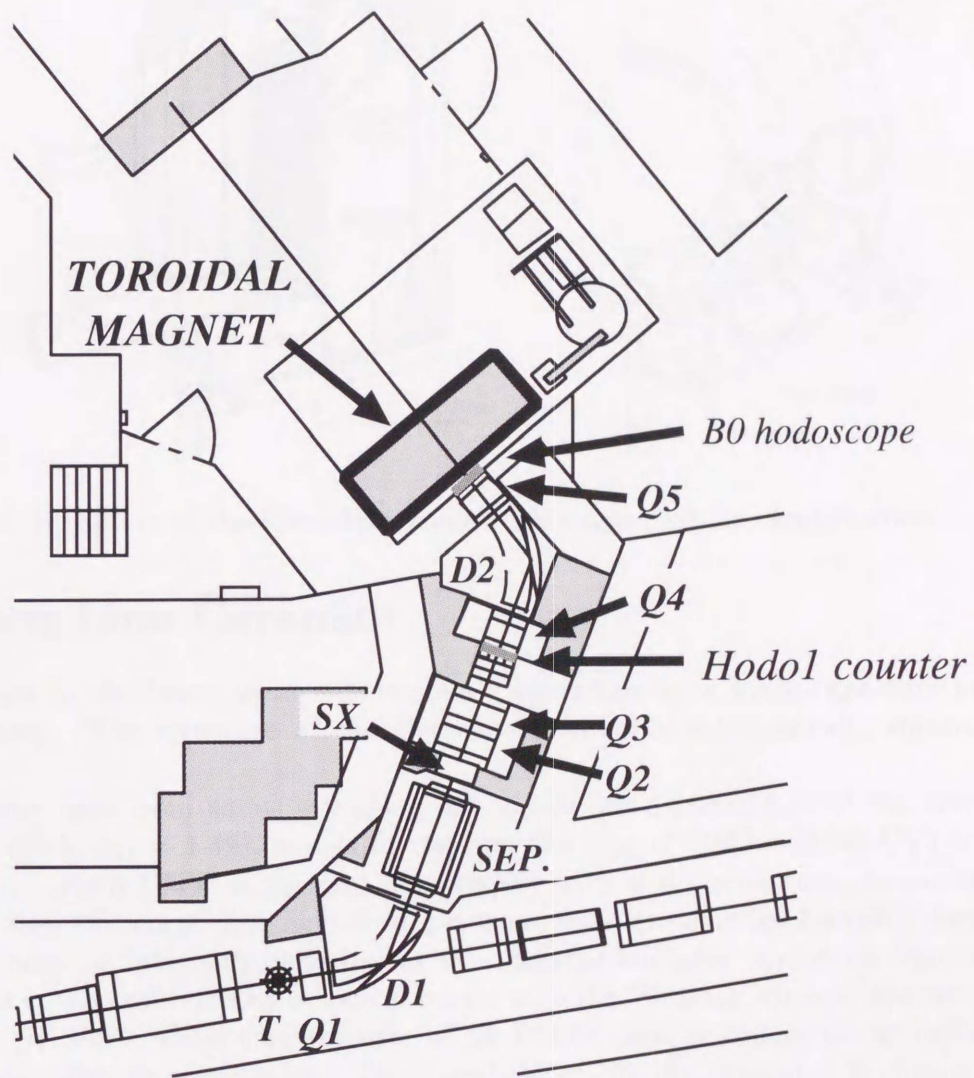
Figure 2.3: Layout of the K5 beam line
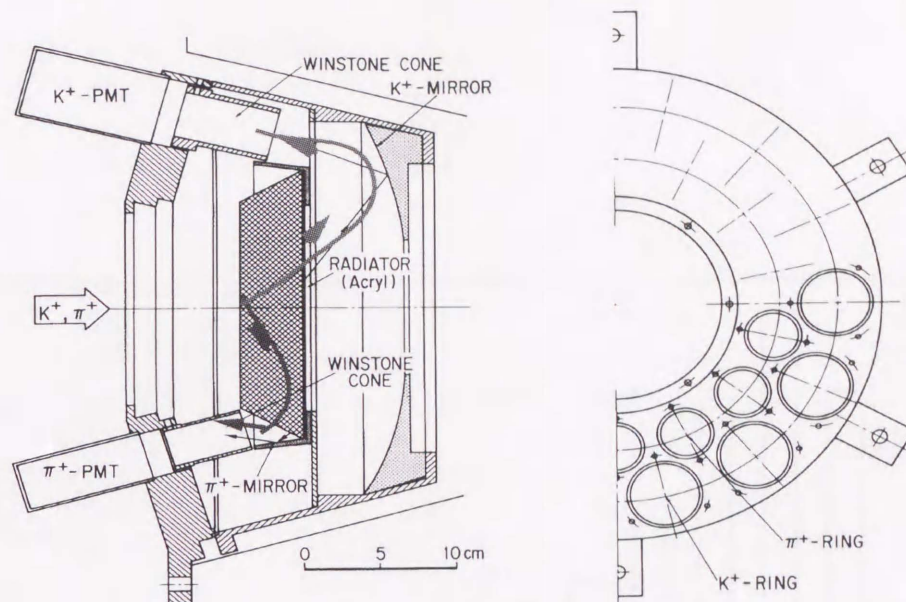
Figure 2.4: Structure of the Čerenkov counter for beam particle identification.

2.3 Beam Line Čerenkov

Kaons and pions in the beam were independently identified by a Fitch-type threshold Čerenkov counter. The structure of the Čerenkov counter is schematically shown in Fig.2.4.

The Čerenkov light from kaons is coming out of the downstream face of the acrylic radiator (4cm thick, $n_D = 1.49$), and is focused on the ring of PMTs (R580 UV) by a parabolic mirror. Each PMT of the ring is equipped with a Winston cone, to increase the light collection efficiency. The light from pions, whose Čerenkov light angle is larger than that of kaons, is internally reflected at the radiator surfaces, and exits from the conical edge. It is then reflected by a conical mirror into the Winston cones of the second ring of PMTs (R1398). Each ring consists of 14 PMTs, and is connected to LeCroy multiplicity logic after discrimination. The threshold of the discriminator is chosen so that it is equivalent to 2 photoelectrons. The multiplicity spectra of the kaon ring and the pion ring, respectively, are shown in Fig. 2.5.

We required the multiplicity of the kaon ring to be 7 or more, and the pion ring to be 6 or more. With this setting, the probability of tagging a pion as a kaon was less than 0.02%, and the total efficiency of the Čerenkov counter for kaons was better than 99.98%.

A timing for kaons and pions was measured by the B0 hodoscope which was placed upstream of the Čerenkov counter. The hodoscope is finely segmented and each finger is fed to a pipeline time-to-digital converter (TDC) after discrimination. Thus, we were able to monitor the B0 activity for up to 20μsec. This information was indispensable for
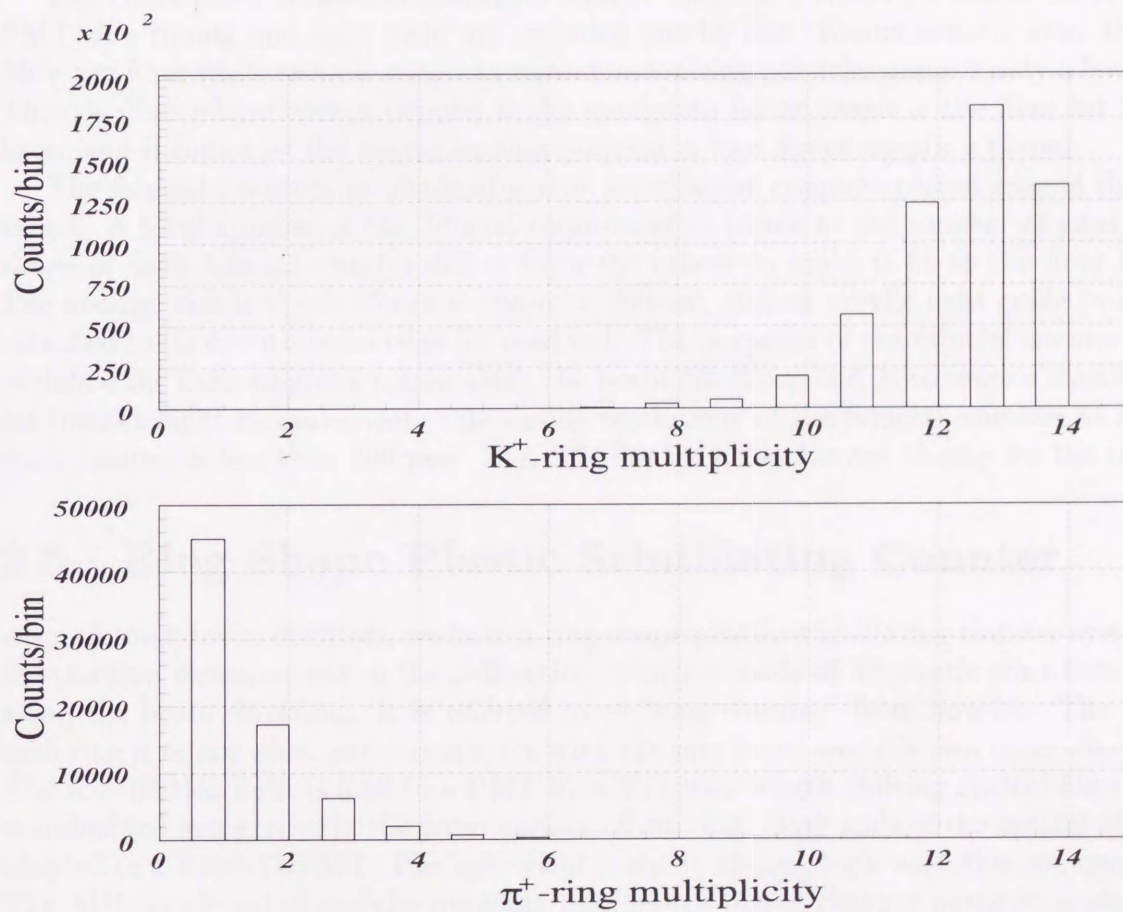
Figure 2.5: Multiplicity spectra of the Čerenkov counter: top) kaon ring spectrum for a kaon beam, and bottom) pion ring spectrum for a kaon

the rejection of the background originated at beam particles in the photon detector.

2.4 Active Fiber Target

A kaon stops in the active target after it is slowed down by the degrader. The active target is made of 256 scintillating fibers in order to obtain the proper position of the kaon decay vertex and to make the energy loss correction for outgoing charged particles. A schematic picture of the target assembly is shown in Fig. 2.6.

Each fiber has a dimension of 5mm × 5mm × 2m, and is read by a Hamamatsu H1635 PMT. It's timing and light yield are recorded one by one. Kaons deposit more than 15 MeV per fiber while radially outgoing minimum ionizing particles deposit only a few MeV. Thus, a fiber whose energy deposit is the maximum for an event is the fiber hit by the kaon, and it indicates the kaon stopping position in two dimensions(x-y plane).

The fiducial counters are made of plastic scintillation counters placed around the fiber target. A total number of the fiducial counters is 12 (same as the number of gaps). The shape of each fiducial counter differs from the others to make it fit to the fiber target. The average size is about 25mm × 10mm × 200mm, and an acrylic light guide ($\sim$2 m) is attached to its down stream edge for read out. The purposes of the fiducial counter are 1) to define the kaon stopping region along the beam direction, and 2) to sense a start-timing for time-of-flight measurement. The timing resolutions of the fiducial counters as a TOF start counter is less than 200 psec. Fig. 2.7 shows a typical event display for the target.

2.5 Ring Shape Plastic Scintillating Counter

Around the fiducial counters, we have a ring-shape plastic scintillating counter system for the position measurement in the z-direction, which is made of 32 plastic scintillator rings along the beam direction. It is referred to as "ring counter" from now on. The size of each ring is 6 mm wide, and 5 mm thick with 118 mm inner and 128 mm outer diameters. The scintillation light is lead to a PMT by a Y11 wavelength shifting optical fiber which is embedded in a groove in the outer surface of the ring. Both ends of the optical fiber are coupled to a R580-17 PMT. The light yield is about 46 p.e./MeV with this configuration. The ADC spectrum of radially outgoing minimum ionizing charged particles is shown in Fig. 2.8.

The discrimination threshold was set around $2 \sim 3$ photoelectrons, and thus the intrinsic efficiency was close to 100%. However, due to dead spaces between the rings, an overall efficiency was 98% or so. A time resolution of 1.0 nsec was also obtained.

2.6 Toroidal Magnet

The spectrometer for charged particles is constructed with a super-conducting toroidal magnet and three MWPCs (Multi Wire Proportional Chambers). The toroidal magnet is cylindrically symmetric with twelve air gaps and it obtains a large acceptance ($\sim 10\%$

Ring Counter

Fiducial Counters

Active Fiber Target

End View

Side View
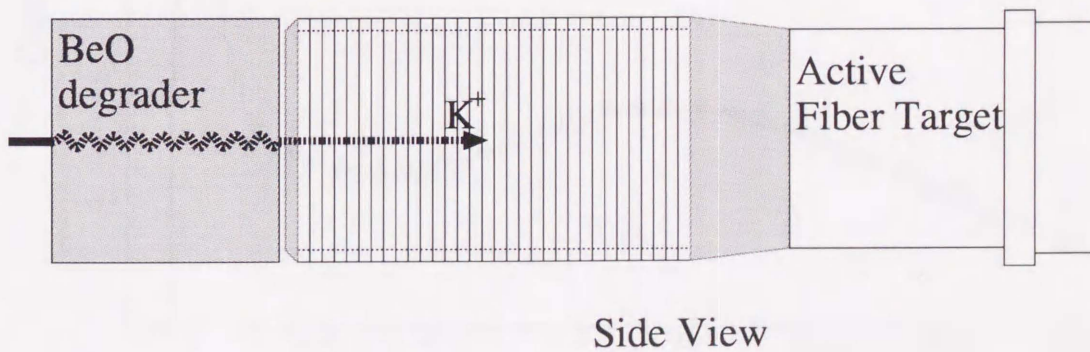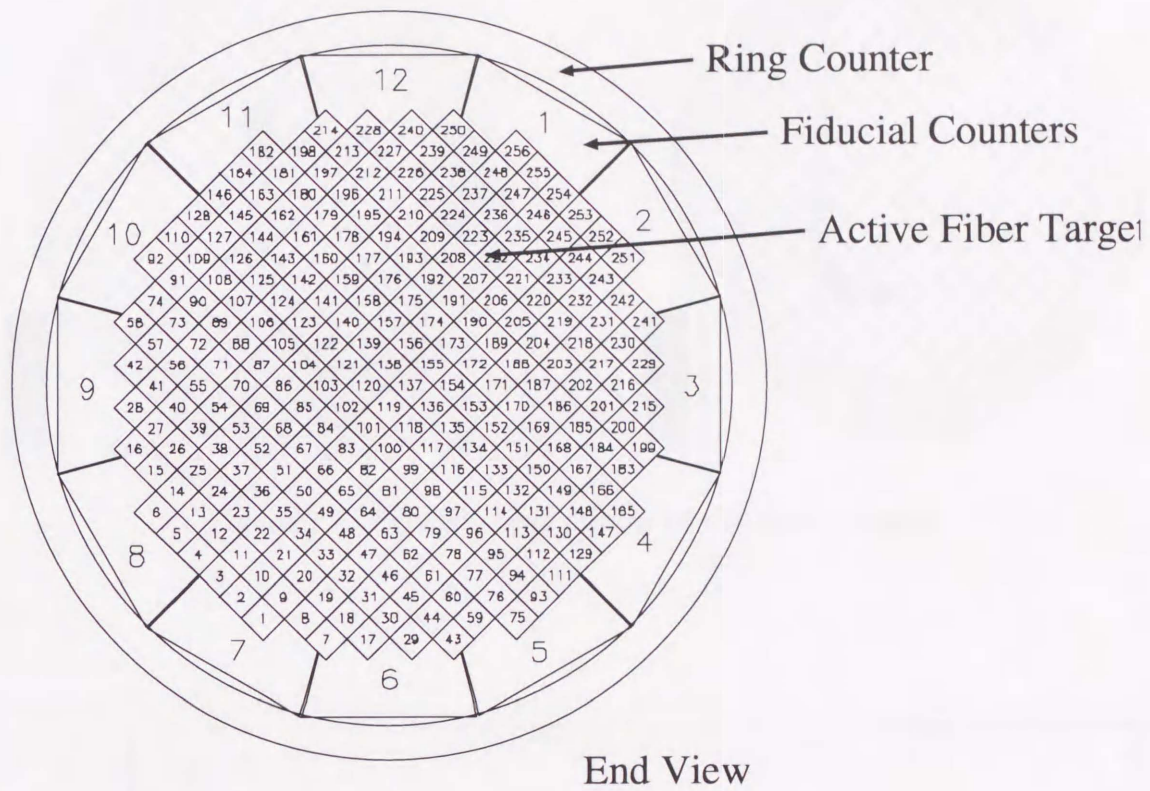
Figure 2.6: The Schematic picture of the K^+ stopping active target peripherals.
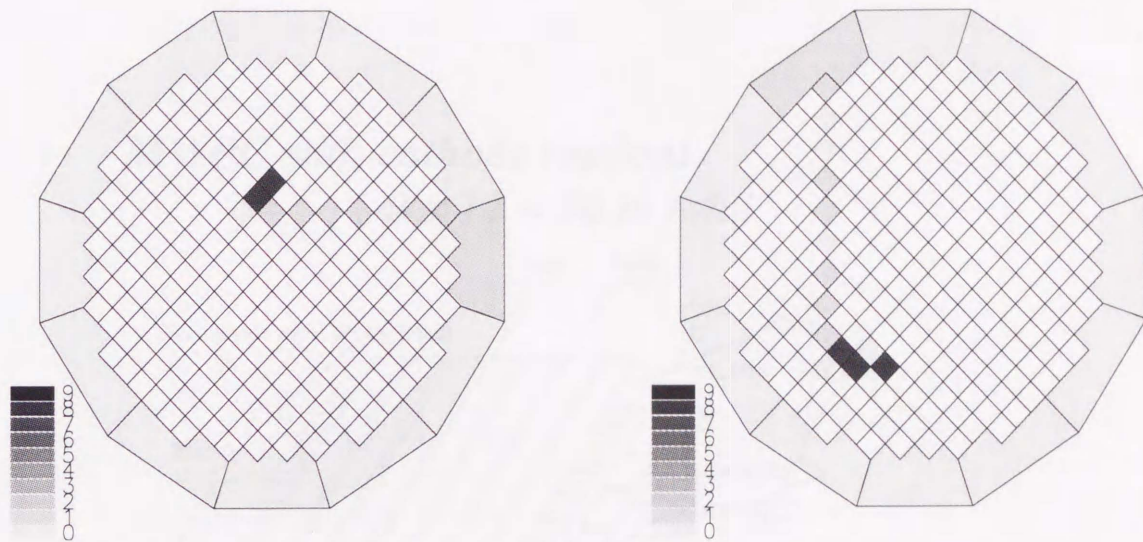
Figure 2.7: Typical event display of the active target.
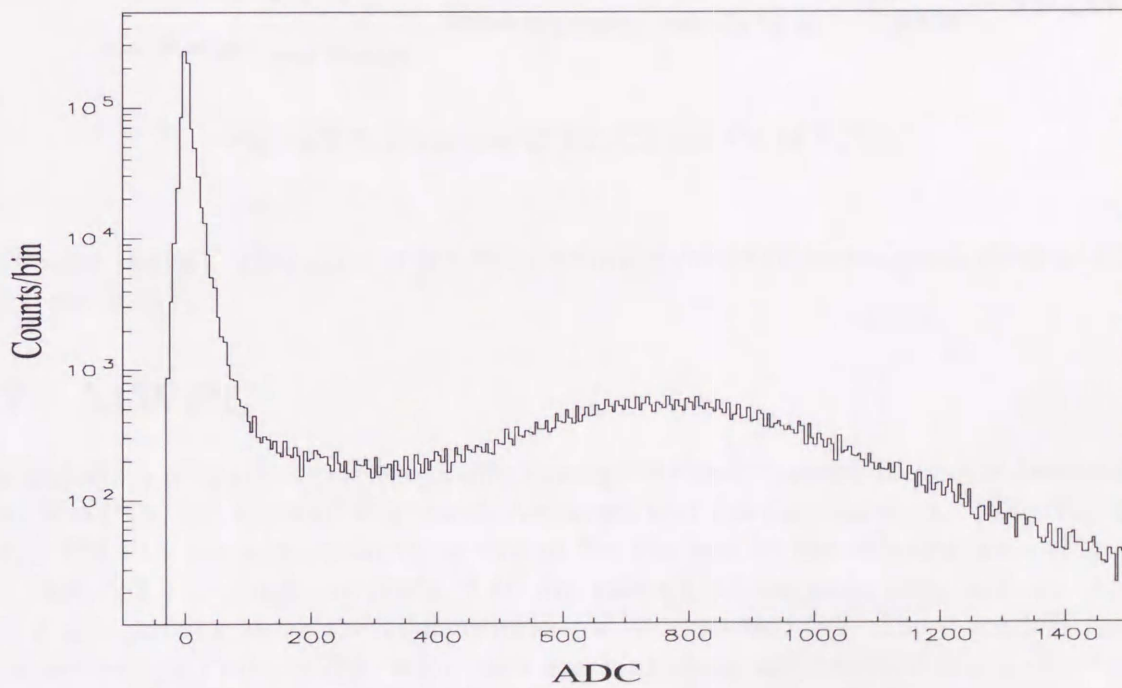
Figure 2.8: ADC spectrum of the ring counter by radially outgoing minimum ionizing particles.

MWPC with cathode readout
3 x 12 = 36 in total
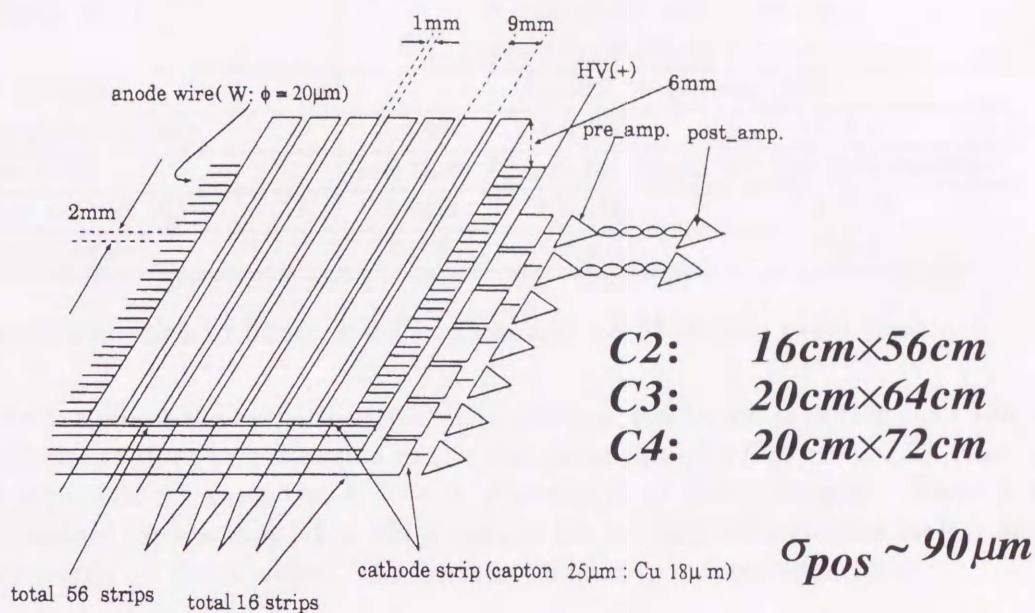
Figure 2.9: Structure of C2, C3 and C4 MWPCs.

of 4π solid angles). This experiment was performed under three magnetic fields of 0.9T, 0.65T and 0.45T.

2.7 MWPC

The trajectory of charged particle passing through the spectrometer magnet is detected by three MWPCs, C2, C3, and C4, the active target and the ring counters. The structures of the MWPCs are almost identical except for the size of the effective area (Fig. 2.9 and Table 2.3). Anodes are made of 20 μm gold-plated tungsten wire, and are strung with 2 mm spacing along the momentum-sensitive direction (x). There are two planes of cathode strips (9mm width, with 1mm spacing) along orthogonal x and y directions. The gap between the cathode and the anode is 6mm. The gas is a mixture of Ar and ethane (50%:50%). Signals are read out from cathode strips on the both planes. They are amplified and differentiated by a hybrid current amplifier, and they are transmitted by twisted pair ribbon cables, then received by a post-amplifier. The analog outputs from 6 post-amplifiers are summed and fed to an ADC. We determine a hit position from the

Table 2.3: Parameters of the C2, C3 and C4 MWPCs

	C2	C3	C4
Effective area ($x \times y$ mm^2)	560×160	640×200	720×200
Half gap		6 mm	
Anode wire		gold plated tungsten, $\phi = 20\mu m$	
Anode pitch		2 mm	
Cathode strip		9 mm width and 1 mm gap	
		$18\mu m$ Cu on $35\mu m$ Kapton film	
Gas mixture		Ar 50% + Ethane 50%	
Operation voltage	3.9 kV	4.0 kV	4.0 kV
Resolution		less than $700\mu m$ for up to 40° inclined incident	
Single rate at K5†	3 kHz	0.7 kHz	0.7 kHz
Current draw†	$2\mu A$	$0.5\mu A$	$0.5\mu A$

† with normal condition of E246: 300 k of kaon and 1.8 M of pion per 0.7 sec.

charge distribution on the cathode strips. The intrinsic resolution is better than 700 μm.

Fig. 2.10 shows the χ^2 distribution in the case of tracking by C2, C3 and C4 chambers for a well identified π^+ from the $K^+ \rightarrow \pi^+\pi^0 decay(K_{\pi2})$ event samples. There is one degree of freedom for tracking. The main part of the χ^2 distribution more or less agrees with the expected χ^2 distribution. The tracking efficiency is more than 95%.

2.8 TOF counters

The time-of-flight (TOF) analysis is performed by using the fiducial counters as a start counter and the TOF counter at the magnet exit as a stop counter in conjunction with the information on particle momentum (p) and the flight path length obtained from tracking. Fig. 2.11 shows the correlation between the square of analyzed particle mass m^2 and p. Muons and positrons in the momentum spectrum below the $K_{\pi2}$ peak ($p = 205$ MeV/c) are from $K^+ \rightarrow \pi^0\mu^+\nu K_{\mu3}$ and $K^+ \rightarrow \pi^0 e^+\nu$ (K_{e3}) decay, respectively. The separation of the K_{e3} from the $K_{\mu3}$ events is accomplished with this TOF analysis. It is also possible to use dE/dx information of the TOF stop counter as shown in Fig. 2.12. Thus, the contamination of K_{e3} can be suppressed to much less than 1% from this analysis alone.

2.9 CsI(Tl) Electromagnetic calorimeter

Energies and directions of the two photons from π^0 decay are measured by an array of 768 CsI(Tl) crystals (Fig. 2.13). It covers 75% of the total solid angle around the kaon stopping target with 12 holes for outgoing μ^+ and two holes for the beam entrance and exit. Each crystal has a length of 25 cm (13.5 radiation lengths), and a coverage of 7.5° along the polar and azimuthal directions except 48 crystals nearest to the beam axis (15°
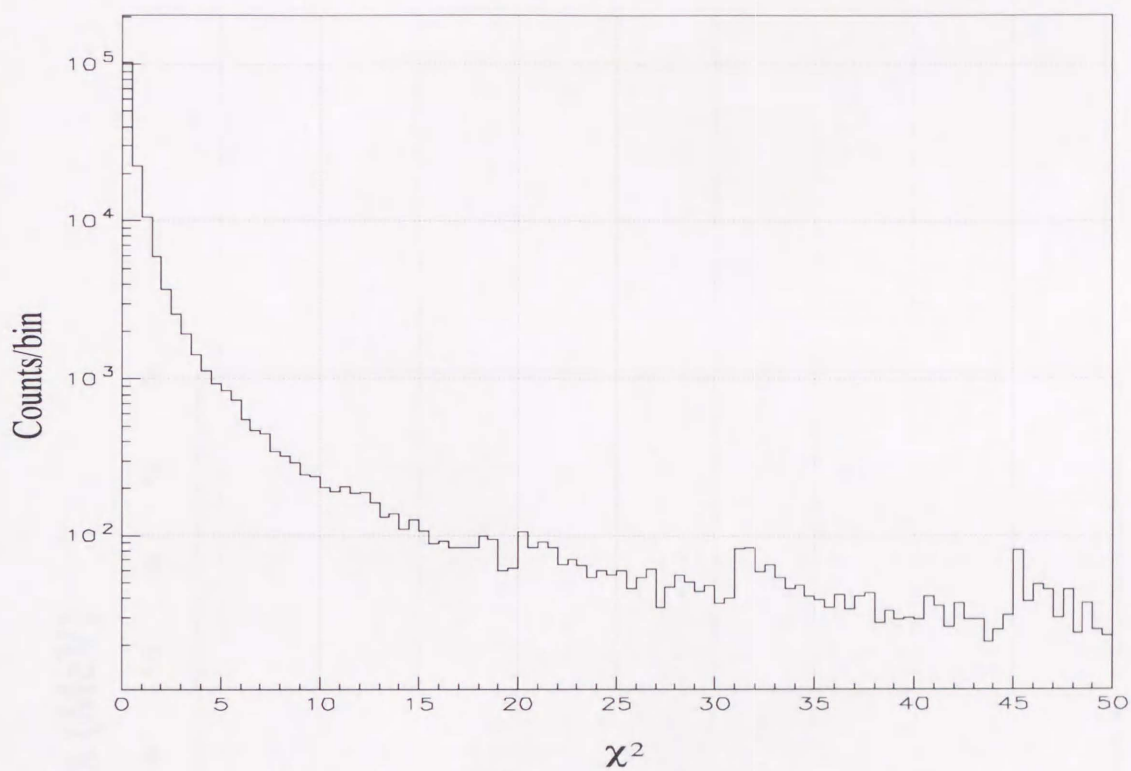
Figure 2.10: χ^2 distribution of the π^+ track from $K_{\pi 2}$ decay measured by C2, C3 and C4.
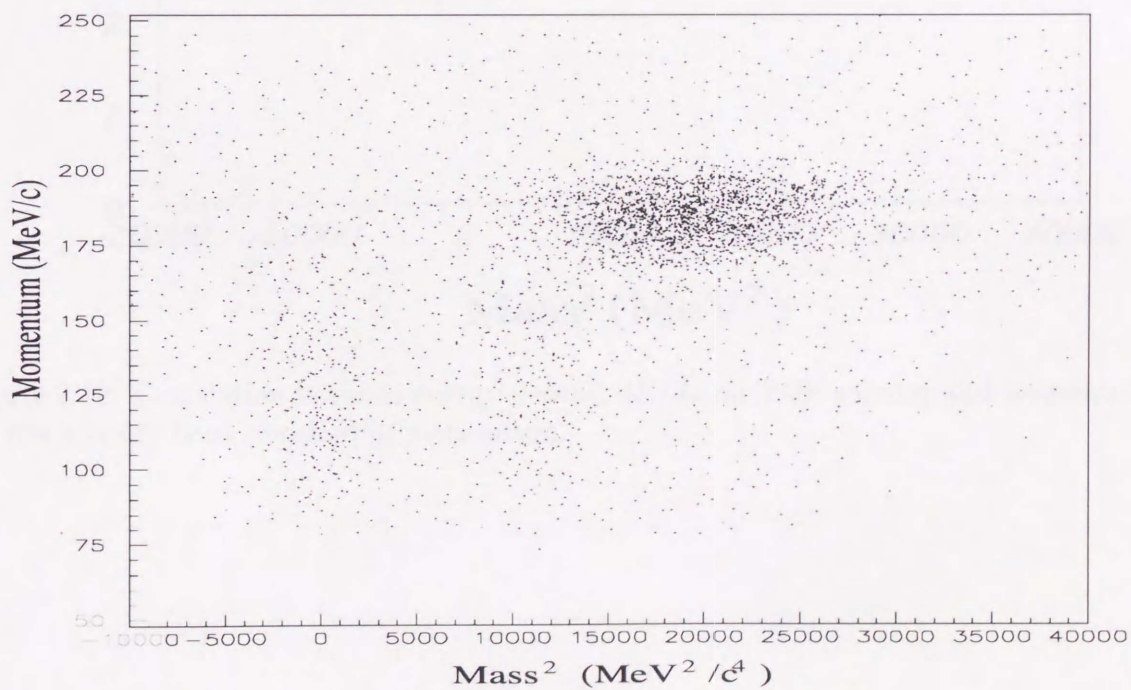
Figure 2.11: Correlation between m^2 and momentum from TOF analysis.
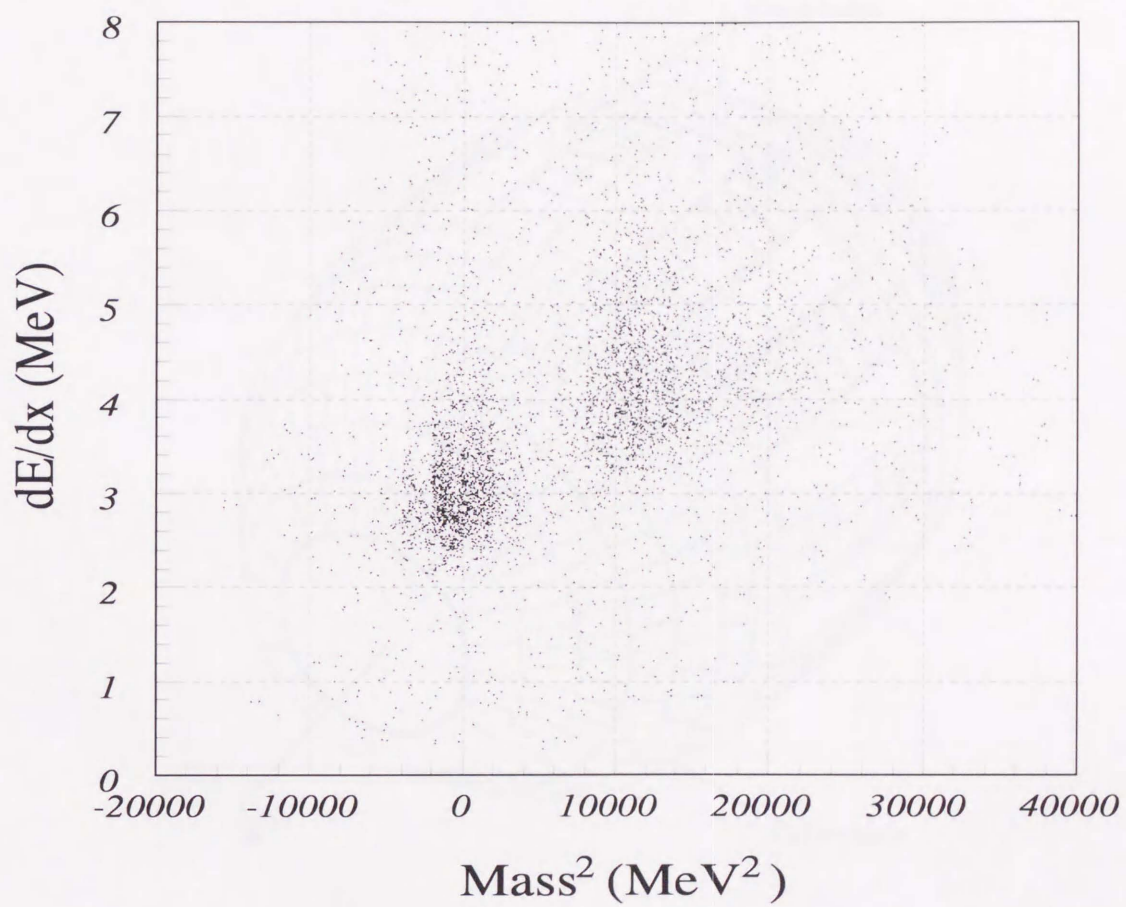
Figure 2.12: Correlation between energy deposit dE/dx on TOF counter and momentum. π^+ has already been removed in momentum.
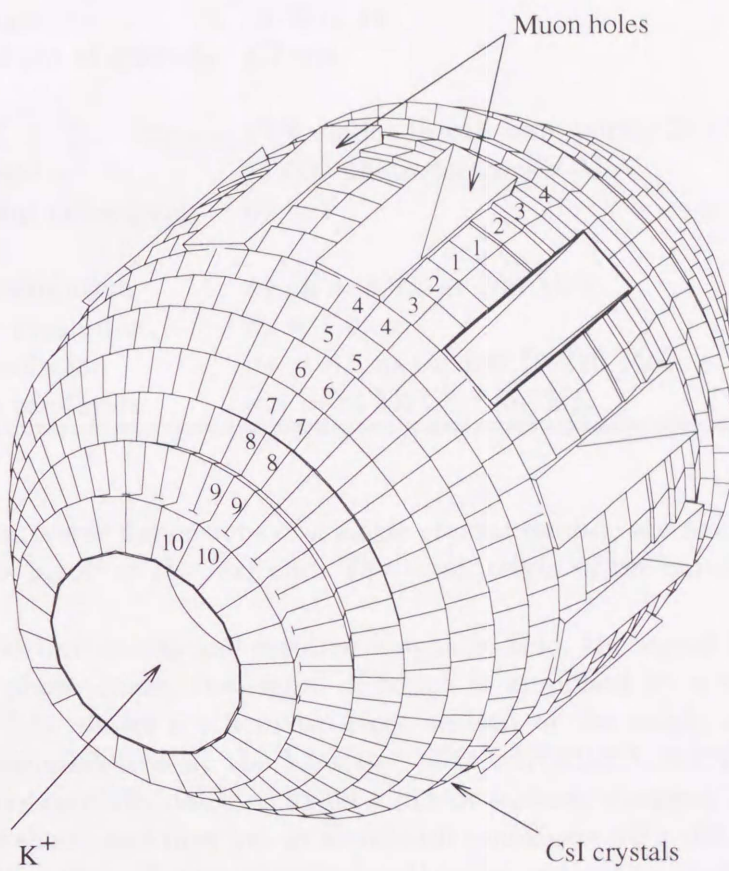
Figure 2.13: Three dimensional views of CsI(Tl) π^0 detector.

Table 2.4: Main parameters of the CsI(Tl) π^0 detector

Parameter	value
Segmentation	$\Delta\theta = \Delta\phi = 7.5°$ (partly $\Delta\phi = 15°$)
Number of crystals	768
Length of crystals	25 cm (13.5 X_0)
Inner radius	20 cm
Outer radius	50 cm
Solid angle	75 % of 4π
Total weight of crystals	1.7 ton
Readout	PIN diode (18×18 mm, partly 28×28)
Light yield	11,000 photoelectrons / MeV
Equivalent noise level	65 keV
Energy resolution	$\sigma_E/E = 3.0\%$ at 200 MeV
Position resolution	$\sigma_p = 1.0$ cm
Time resolution	$\sigma_T = 6.5$ ns for E= 10-220 MeV
π^0 mass resolution	$\sigma_{\pi^0} = 14$ MeV/c^2 for $K_{\pi 2}^+$

in azimuth). The transverse dimensions of a single crystal module are about 3×3 cm^2 at the front end and 6×6 cm^2 at the rear end. The total weight of the calorimeter is about 1.7 tons.

Due to the spatial limitations and residual magnetic field, the signal from CsI(Tl) is read out by a PIN photo-diode, the signal of which is amplified by a charge sensitive pre-amplifier. Fig. 2.14 shows a schematic cross section of the single crystal module. The crystals were manufactured by the Kharkov "MONOKRISTALREAKTIV" factory in Ukraine. They were carefully polished to get a mirror surface, wrapped in 300 μm thick white Millipore filter sheet, and then put in aluminum containers with 100 μm thick walls. PIN photo-diodes ($18 \times 18mm^2$) were attached to the rear end of the crystal with silicone glue. The charge sensitive pre-amplifiers were mounted right behind the PIN photo-diode in the aluminum container. A gain of the pre-amplifier is 0.5 V/pC, it's time constant is 600μsec, and the bias voltage to PIN photo-diode is chosen to be 45V. Each module has very high performance in light yield and low noise characteristics[Kud92].

After differentiating the signal with pole-zero-cancellation to a time constant of 44 μsec, it was transferred to the electronics hut by twisted pair ribbon cables. Then, it is shaped with a time constant of 1μsec and is fed to ADC, TDC (after discrimination by CFD).

The total energy resolution was measured to be

$$(\frac{\Delta E}{E})^2 = (2.38\%)^2 + (\frac{0.298\%}{E(GeV)})^2 + (\frac{0.866\%}{\sqrt{E(GeV)}})^2 \qquad (2.1)$$

from a beam test of 30 crystals. The position resolution is about 1cm in r.m.s. A light
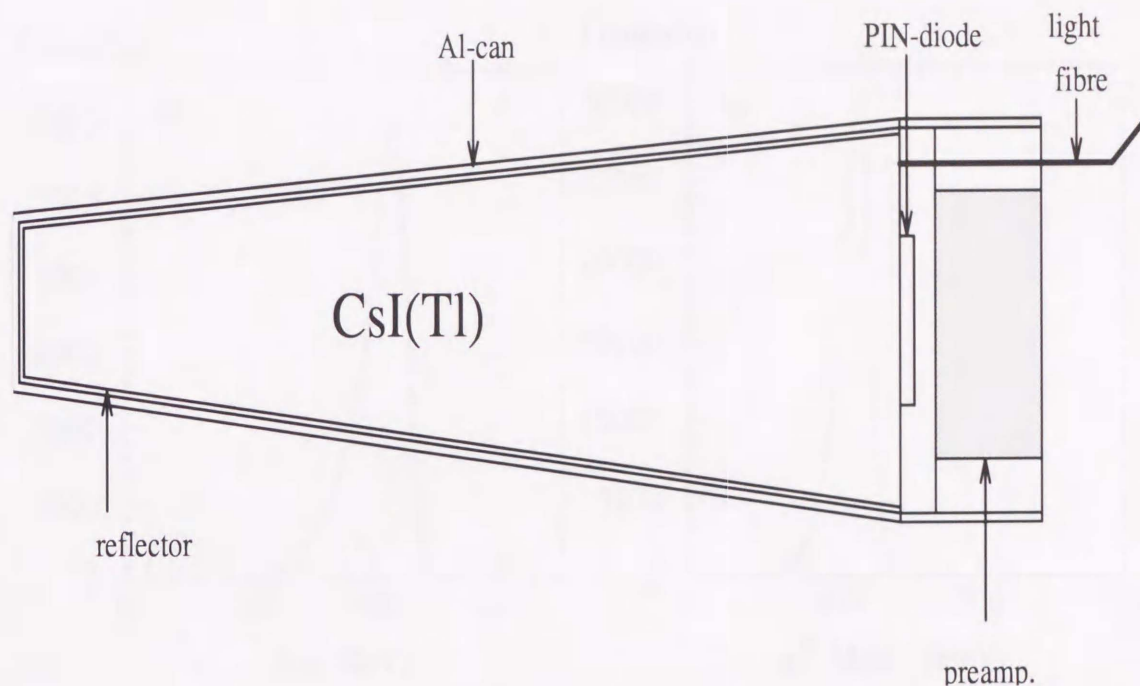
Figure 2.14: Schematic cross section of a CsI(Tl) crystal module.

from a Xe lamp is fed to each module via an optical fiber. The gain drift can be frequently checked. No significant light-yield degradation has been found since the start of operation. The temperature within the detector housing is controlled at $20 \pm 1°C$, and the humidity is typically kept at lower than 16%. Fig. 2.15 shows spectra of a) two-photon energy sum and b) reconstructed π^0 mass from the $K_{\pi 2}$ decay ($K^+ \rightarrow \pi^+ \pi^0$).

The overall actual energy resolution of the barrel is somewhat worse than the estimated performance from the prototype because of lateral shower leakage, mainly from the 12 muon holes. The low energy tails of the $M_{\gamma\gamma}$ and $E_{\gamma\gamma}$ spectra are due to this leakage. However, both $M_{\gamma\gamma}$ and $E_{\gamma\gamma}$ spectra are free from background and thus π^0 identification is satisfactory. This is partially because of the good time resolution ($\sigma_T = 6.5$ nsec) of the crystals. The π^0 mass resolution is slightly different between the $K_{\pi 2}$ and $K_{\mu 3}$ decays because of the difference in the decay kinematics and photon energy dependence of the shower leakage.

Fig. 2.16 shows the distribution of a total number of clusters.

2.10   Run conditions

The experimental runs were done with several conditions of the toroidal magnetic field and the K^+ intensity, as shown in Table 2.5. The measurements were done under three different magnetic field, to accept a wide momentum range of μ^+. Therefore, the systematic effect coming from the acceptance of toroidal magnet spectrometer and from the magnetic field can be checked . Also the K^+ beam intensity was changed to study an
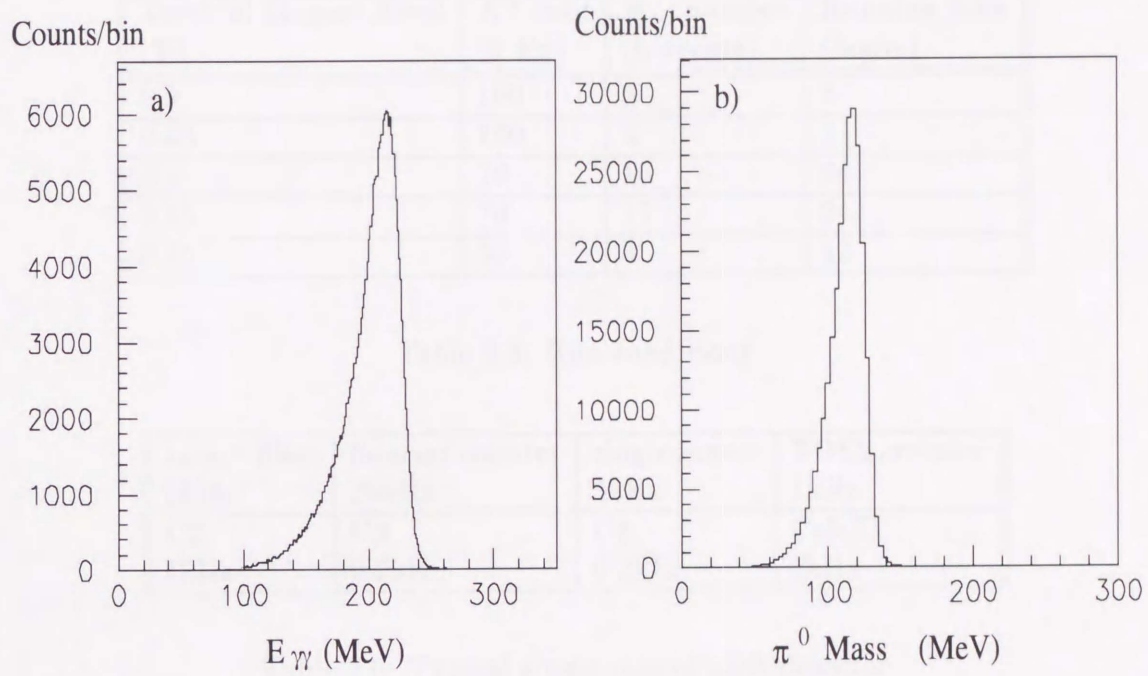
Figure 2.15: a) total energy sum of two photons from π^0 in $K_{\pi 2}$ decay, and b) reconstructed π^0 mass from $K_{\pi 2}$ decay.
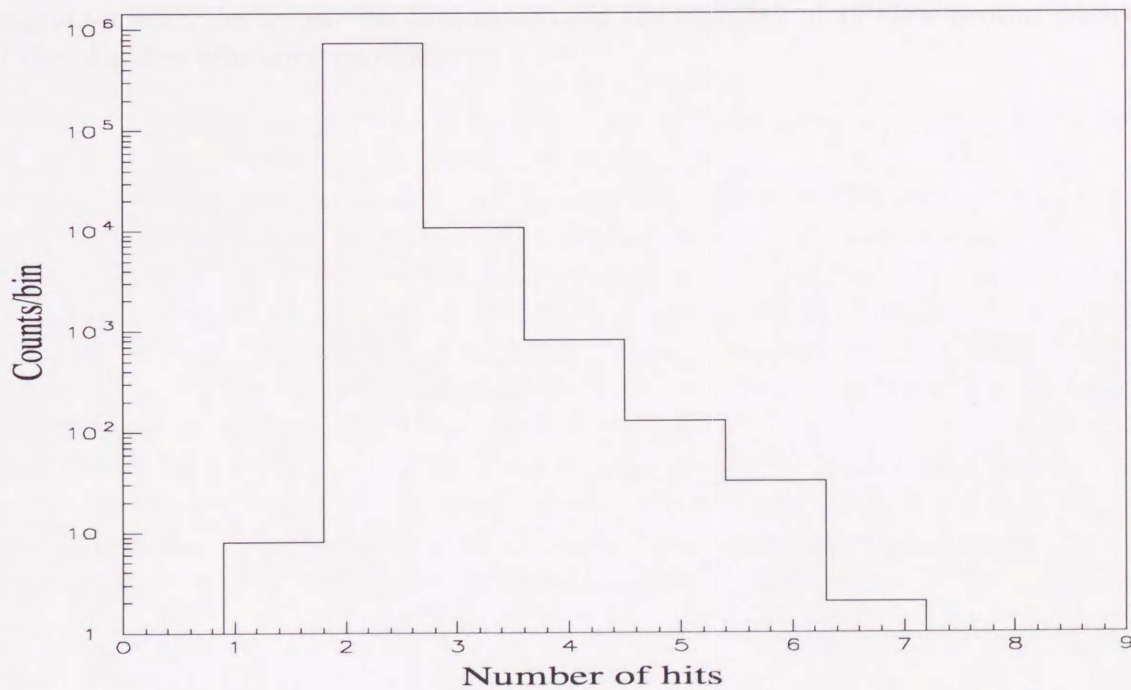
Figure 2.16: Number of photon clusters

Toroidal Magnet Field (T)	K^+ rate (k Hz)	$K_{\mu 3}$ number (k events)	Running time (hours)
0.9	100	3	5
0.65	100	3	5
0.9	70	16	24
0.65	70	17	24
0.45	30	3	12

Table 2.5: Run conditions

target fiber 1kHz	fiducial counter 20kHz	ring counter 5kHz	TOF2 counter 1kHz
C2 1kHz	C3 0.2kHz	C4 0.2kHz	CsI(Tl) 2kHz

Table 2.6: Typical single rate of each detector

effect of the beam backgrounds on the CsI(Tl) detector. We collected 42K $K_{\mu 3}$ events totally, which is 7 times higher statistics than the previous experiment [Mer74]. A typical single rate of each detector was shown in Table 2.6. During the run time, a single rate of the CsI(Tl) photon detector was kept to be less than 5kHz, in order to suppress the background from the beam. We also monitored the stability of 12 GeV proton intensity and the chamber efficiency carefully.

Chapter 3

Data Acquisition

3.1 Trigger

A schematic view of the trigger system is shown in Fig.3.1.

The trigger system consists of multiple levels. The first level trigger is defined as

$$\check{C}_K \otimes \sum_{i=1}^{12}(\text{FID}_i \otimes \text{TOF}_i), \tag{3.1}$$

where $\check{C}_K$ is a hit of the kaon Čerenkov counter with multiplicity larger than 6. FID_i is a hit of the i-th fiducial counter or its adjacent gaps and TOF_i is a hit of the TOF stop counter in i-th gap. $\otimes$ means AND logic.

Namely, the 1st level trigger requires that a kaon comes to the detector as an incident and its daughter particle from K-decays hits the fiducial counter and then passes through the toroidal magnet gap and the TOF stop counter.

The 1st level trigger rate was about 200/beam-spill per gap, i.e. 2.4k/pulse in total, for 300k incident kaons/beam-spill with a π/K ratio of 6.

The second level trigger required hits in the CsI(Tl) photon detector. Analog signals from CsI(Tl) crystals were discriminated by a constant fraction discriminator (CFD) with an energy threshold of 5 MeV, and then the existence of at least one discriminated signal within a coincidence time window of 150nsec is required. If the crystals surrounding the muon hole through which muon goes went, got a hit, events were vetoed in order to suppress the events where muon was scattered off the crystals around the muon hole. A rejection factor at the 2nd level trigger was about 1.7.

All events which did not satisfy the 2nd level trigger by 20μsec after the 1st level trigger were deleted. As a consequence, about 110 events out of 2.4k 1st level triggers (from 300k kaons/pulse) survived, and 100 events were recorded on the tape for the later off-line analysis. The reduction factors of the trigger rate are summarized in Table 3.1.

3.2 Data Acquisition

DAQ system was designed as a parallel processing system united by crates, and the online analysis system was designed as a distributed system based on networks.
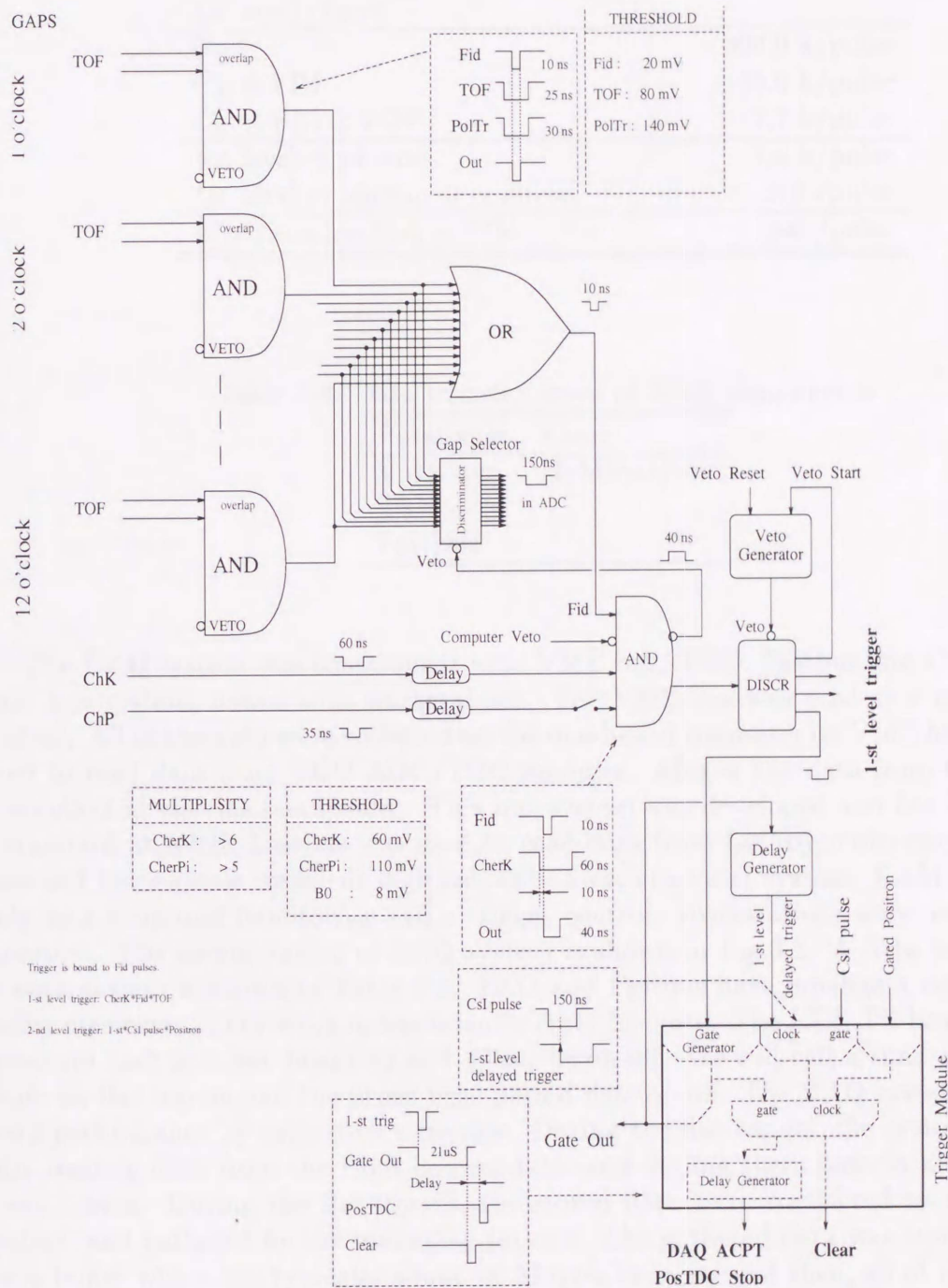
Figure 3.1: Block diagram of the trigger scheme

Table 3.1: Break down of the total 12 gap trigger rate

	3×10^{12} protons/pulse
1st level trigger	
$\check{C}_K$	300.0 k/pulse
$\check{C}_K \otimes \text{FID}$	125.0 k/pulse
$\check{C}_K \otimes \text{FID} \otimes \text{TOF}$	7.7 k/pulse
1st level $\otimes$ photon	1.4 k/pulse
1st level $\otimes$ photon $\otimes$ positron	110 /pulse
Live time fraction = 90%	100 /pulse

Table 3.2: Data transfer speed of DAQ components

Parameter	Value
VME bus	10 Mbyte/sec
TKO	
FastBus	

The DAQ system was constructed with VME bus, TKO, Fastbus and CAMAC standard bus system, linked with workstations. The VME bus was used as a main backend system. All of the data were collected on the one-board computer on VME bus. TKO was used to read data from TKO ADC/TDC modules. Almost the data from the detectors was collected via this bus system. This bus system was developed and has been used as a standard at KEK. Fastbus was used to read data from LeCroy multi-stop TDC modules and home-made transient digitizer(wave form analyzer) system. CAMAC was used only as a condition monitoring and a trigger control. Workstations were used for online monitors. The configuration of DAQ system is shown in Fig.3.2. A data transfer speed of each system is shown in Table 3.2. TKO and Fastbus have intelligent controllers and buffer memories. They work independently crate by crate. The KEK-PS beam has a spill structure that is 0.7sec beam on and 3.0sec beam off. We will call a time period during beam on flat-top-on and the other time period flat-top-off. The DAQ system works with good performance by using this structure. During the flat-top-on, the system performed only reading data from the front-end modules and storing them onto local memories in every crates. During the flat-top-off, the stored data were transfered to the back-end system, and gathered by the managing process. The gathered data was stored in a large main buffer which has typically about 16 Mbytes capacity and then, all of the data were recorded onto a DLT tape drive. And a part of the data were distributed to a few analysis processes via Ether-Net for online monitoring.

DAQ configration
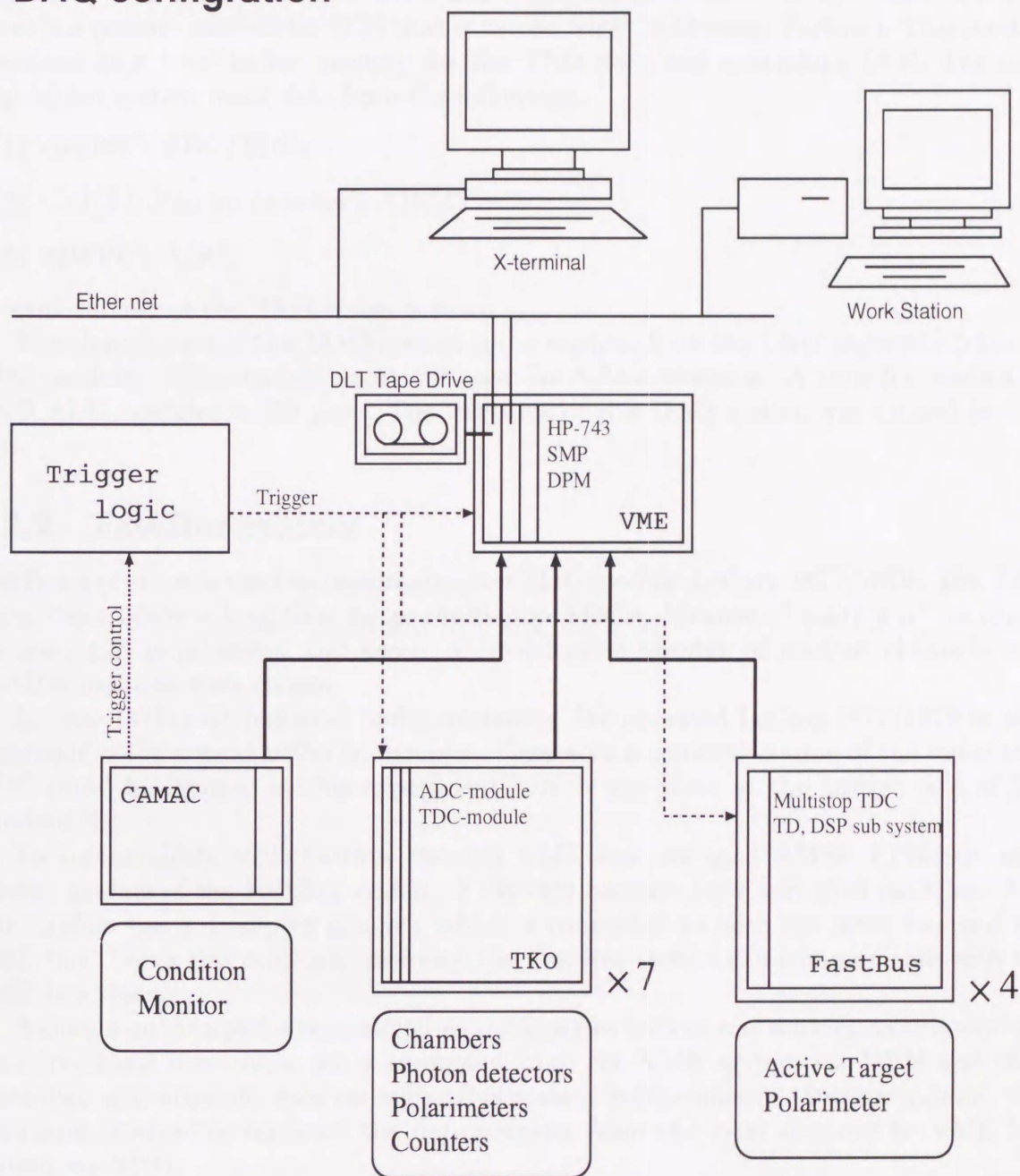
Figure 3.2: A schematic view of DAQ configuration

3.2.1 TKO system

TKO is a KEK standard bus system that was developed by the KEK electronics group. Many useful TKO ADC/TDC modules are available. There is an intelligent sequencer which is named SCH (S Control Header). SCH has many functions for reading modules and works as a bridge between TKO and VME bus in a crate. In the VME bus side, there is a partner module for SCH that is named SMP (S Memory Partner). This module functions as a local buffer memory for the TKO data and controlling SCH. The data acquisition system reads data from the followings.

(1) counter's ADC/TDCs

(2) $CsI(Tl)$ Photon detector's ADC/TDCs

(3) MWPC's ADCs

A total number of the TKO crates is seven.

The slowest part of this DAQ system is the readout from the TKO crate which has 16 ADC modules. This module needs 100 μsec for A/D conversion. A time for reading 16 TKO ADC modules is 350 μsec. The live time of this DAQ system was limited by this fact.

3.2.2 FastBus system

FastBus system was used to read multi-stop TDC module LeCory 1877/1879. The E246 experiment needs a long time range multi-stop TDC's, because of waiting μ^+ to decay. To meet this requirement and accept a considerable number of readout channels, this FastBus modules were chosen.

LeCroy 1877/1879 has local buffer memories. We operated LeCroy 1877/1879 in pipe line mode using a local buffer in modules. Therefore a conversion time of the multi-stop TDC could be ignored in this experiment, which was done at the trigger rate of few hundred Hz.

To communicate with Fastbus through VME bus, we used AMSK FPI68020 as a master module of the FastBus system. FPI68020 controls 1877 and 1879 modules. And this module has a dual-port memory which is connected to both the inner bus and the VME bus. Using this dual-port memory, the FastBus system can communicate with the VME bus system.

A command interpreter for controlling the FastBus system was working on this module. This command interpreter got a command from the VME system via DPM and then controlled and acquired data on a FastBus system independently. During spill-off, this command interpreter initiated the data transfer from the local memory to VME bus system via DPM.

A total number of the FastBus crates is four.

3.2.3 CAMAC system

The CAMAC system was used as a trigger control and condition monitor. In the CAMAC system, output registers, scalers, input registers, scanning ADCs and a crate controller

were used. The crate controller KineticSystems 3922 has a partner Kinetics 2940 which is in the VME crate. The CAMAC system was controlled from the VME side. The CAMAC system works during flat-top-off. After flat-top-on, the CAMAC system was scanning the spill informations, trigger conditions, and voltages of counters for monitoring.

3.2.4 VME bus system

The VME bus system is a master system of these systems. The VME bus system controlled the other systems and read the data that were collected by each system during flat-top-on. HP-753 VME master module (PA-RISC, 64 Mbyte memory) was used as a main DAQ controller. HP-RT, which was a real time operating system based on LynxOS, was working as a host machine. This module was connected to a DLT tape drive. The data was combined and recorded on the DLT tape. There were some slave modules that were partners for the bus masters of the other bus system. They were seven SMP modules for the TKO system and four AMSK DPM modules for the FastBus system. There were another HP-753 module on VME bus. HP-UX that was an operating system based on UNIX, provided the development environment of HP-RT system. When DAQ system was working, it worked as one of online analysis.

3.2.5 Online analysis system

Several workstations were used for online analysis and monitoring. Some fraction of the data were transfered via TCP/IP network. Ordinarily, three workstations, Sun ipx, Sun ipc and HP-753, were used. But, when we needed more analysis power, other workstations could also be used.

3.3 Software

Software part of this DAQ system was developed based on UNIDAQ. UNIDAQ is a DAQ software on UNIX-like OS which was developed at KEK and TIT. We used a buffer manager and a process control system which were brought from UNIDAQ. The standard memory size of a data buffer was 2 Mbytes and a total number of the buffers was 8. The data which were acquired during one spill were stored onto one buffer.

This DAQ program is an ensemble of the following modular processes, where single functioned process cooperates with each other.

novad : *novad* is a buffer manager. This process accepts requests from the other process, and gives them the pointers of the buffer.

xpc : *xpc* manages a process database, and checks whether the processes are stopped illegally or not.

collector : *collector* is a data collector, which controls many devices and reads data, synthesizes and packs data, and writes data onto a buffer.

operator : *operator* is a system control interface for users. We can start and stop a run by using this process.

recorder : *recorder* is a data recorder, which gets data from a buffer and records them onto a tape.

analyzer : *analyzer* is an online analysis process, which gets a part of the data and makes low-level and high-level histograms.

The schematic view of the DAQ software is shown in Fig.3.3.

3.3.1 Collector

The data collection system consists of two programs. One is working on HP-753, and the other is working on 68020FPI. The former is called "collector". The latter is called "CIP".

The function of "collector" is as follows;

(1) communicate with buffer manager

(2) control TKO and collect data from TKO

(3) communicate with CIP, control CIP and get data from FastBus via CIP

The function of "CIP" is as follows;

(1) communicate with "collector"

(2) control FastBus modules and collect data from them

The data collection system was working under a cooperation of the above two programs.

3.3.2 Online analysis

The online monitor system consists of two programs. One is to get data from buffer manager via networks and analyze and make histograms, which is called "analyzer". The other is a histogram viewer. The analyzer could work any UNIX based computers which was connected to networks. The required functions were Sun compatible IPC (Internal Process Control) and socket libraries. Usually, the two workstations were used for this purpose. But, at setup and tuning stage, another workstations were used for spectial analysis. PAW which was an analysis tool developed by CERN was used as a histgram viewer. Many powerful functions included in PAW could be used at online analysis.

The analyzer and histogram viewer worked independently with shared data.

3.4 Performance of DAQ system

3.4.1 Data Size

This experiment used about 2000 channels detector's outputs in total. The data size of one event is about 1600 words(word = 32bit). A typical trigger rate is about 380/spill. The data size of one spill is about 2.4Mbytes.

Schematic View of DAQ software
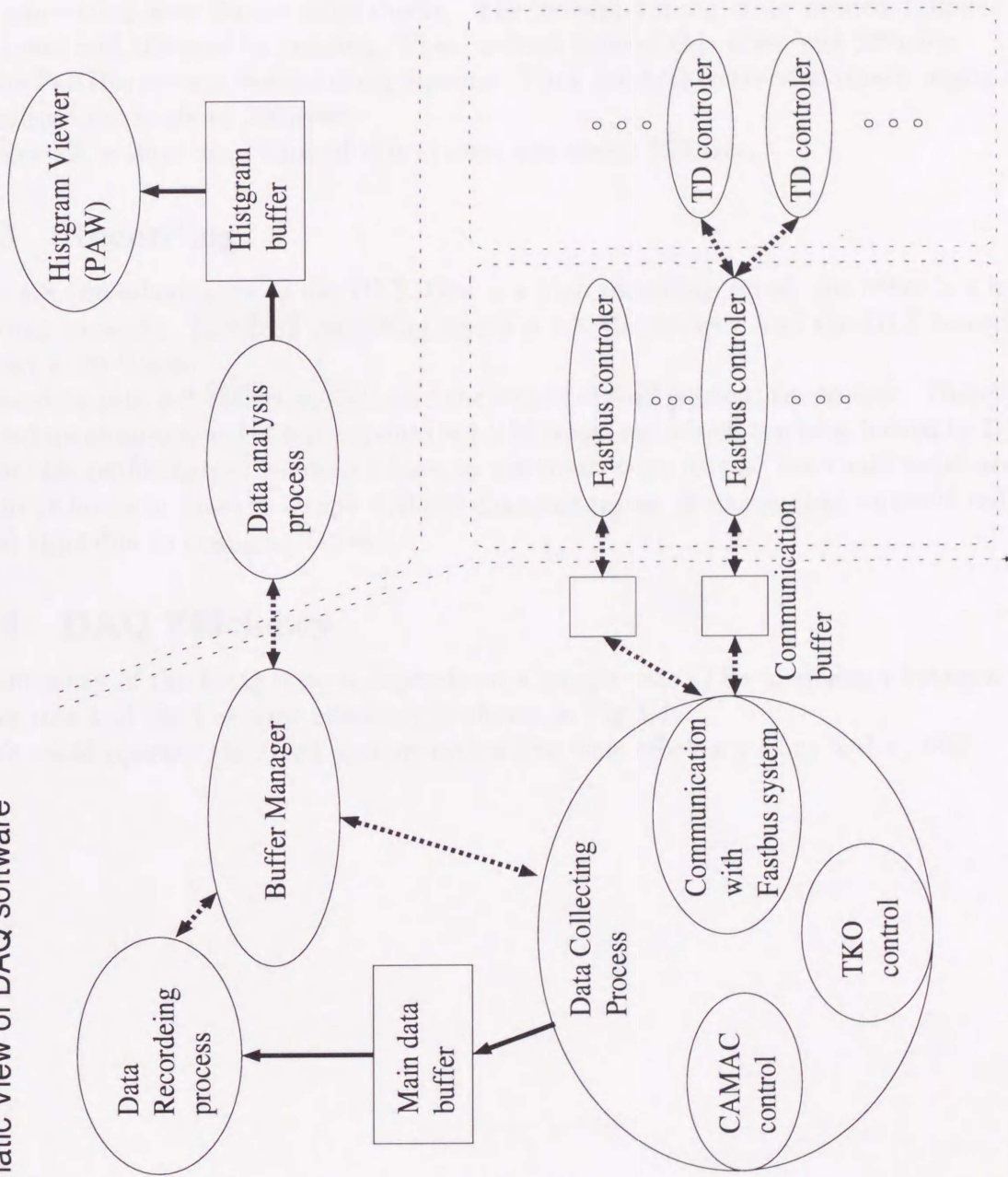
Figure 3.3: The schematic view of DAQ software

3.4.2 Dead Time

A data taking speed of the TKO system is different in each crate. This is because each crate has different module configuration. The trigger timing and the waiting time of A/D conversion were tuned individually. The slowest timing crate needed $120\mu sec$ for conversion and $400\mu sec$ for reading. Then, a dead time of this crate was $520\mu sec$.

The FastBus system worked using pipeline. Thus, an A/D conversion time is negligible. A reading time is about $500\mu sec$.

After all, a total dead time of this system was about $520\mu sec$.

3.4.3 Recording

There are two advantages to use DLT. One is a high recording speed, the other is a large recording capacity. The DLT recording speed is 1.5 Mbyte/sec. And the DLT recording capacity is 20 Gbyte.

The data rate is 2.4Mbytes/spill, and the length of spill is from 2sec to 4sec. Therefore, required maximum speed of writing data is 1.2 Mbytes/sec, which can be achieved by DLT.

For this performance, we didn't have to use multi-tape drives. We could write about 15 runs (8 hours in time) in a tape without changing tapes. It means that we could reduce a dead time due to changing tapes.

3.4.4 DAQ Efficiency

The efficiency of the DAQ system depends on a trigger rate. The correlation between the trigger rate and the live time efficiency is shown in Fig.3.4.

We could operate the DAQ system with a live time efficiency from 70% to 90%.
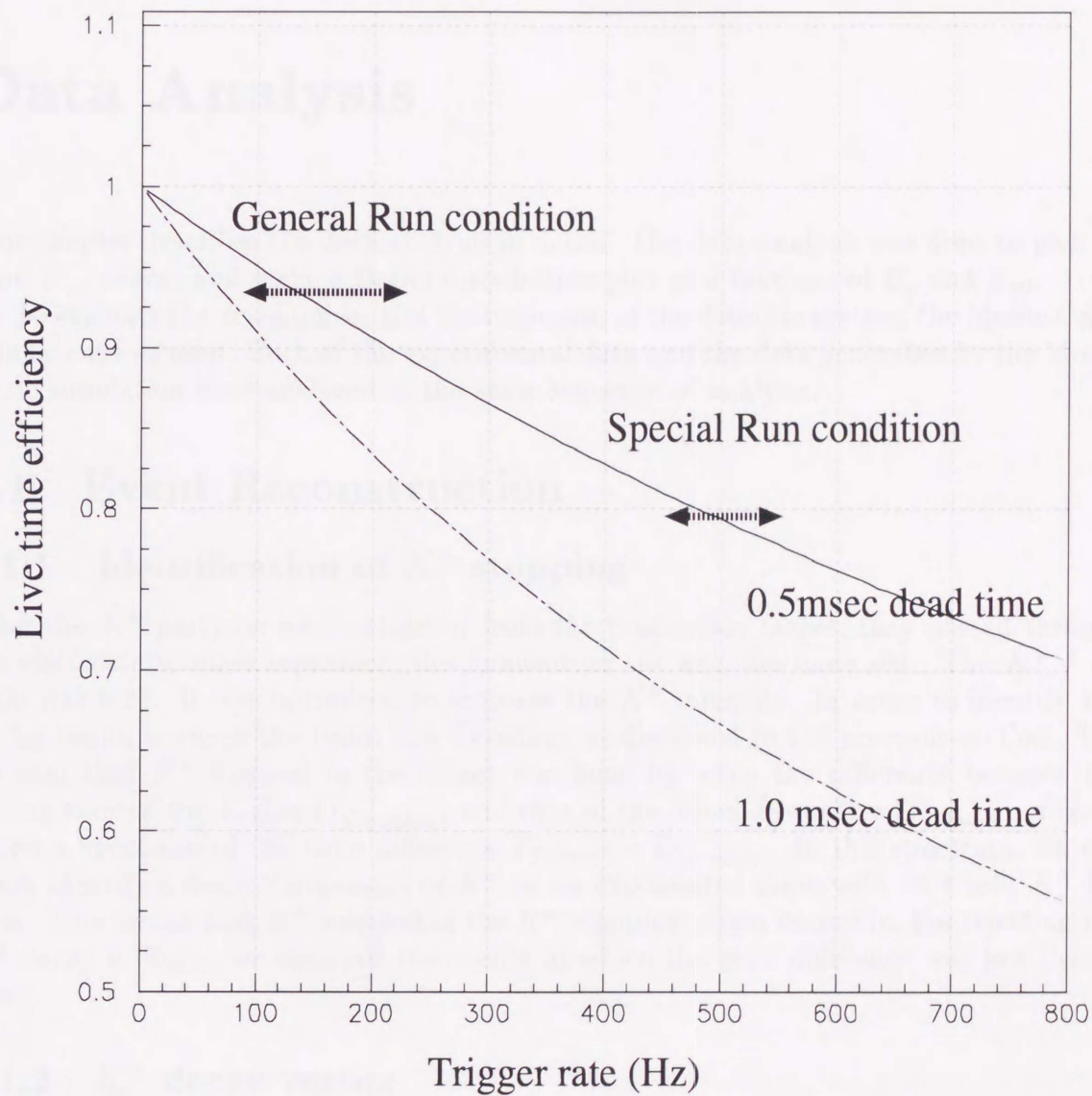
Figure 3.4: DAQ efficiency, where x-axis is trigger rate and y-axis is the efficiency of DAQ

Chapter 4

Data Analysis

This chapter describes the data analysis in detail. The data analysis was done to pick up good $K_{\mu 3}$ events and make a Dalitz distribution plot as a function of E_μ and $E_{\pi 0}$.

To evaluate the acceptances and the responses of the detector system, the Monte Carlo simulation was used. Both of the experimental data and the data generated by the Monte Carlo simulation were analyzed in the same sequence of analysis.

4.1   Event Reconstruction

4.1.1   Identification of K^+ stopping

After the K^+ particles were extracted from the production target, they passed through the electrostatic mass separator, the momentum slit and the mass slit. The K^+ / π^+ ratio was 0.25. It was optimized to increase the K^+ intensity. In order to identify K^+ in the beam, we used the beam line Čerenkov as discussed in the previous section. The decision that K^+ stopped in the target was done by using the difference between the hitting time of the K-ring ($T_{\check{C}erenkov}$) and that of the fiducial counters ($T_{fiducial}$). Fig.4.1 shows a spectrum of the time difference $T_{fiducial} - T_{\check{C}erenkov}$. In this spectrum, we can easily identify a decay component of K^+ as an exponential slope with 12.4 nsec K^+ life time. This means that K^+ stopped in the K^+ stopping target correctly. For rejecting the K^+ decay in flight, we removed the events in which the time difference was less than 3 nsec.

4.1.2 K^+ decay vertex

The K^+ decay vertex was measured by the active K^+ stopping target. The active K^+ stopping target traces the locus of K^+ and μ^+ by observing the deposited energy of each particle. The typical ADC and TDC spectrum of each fiber are shown Fig.4.2.

The K^+ stopping position is identified as a maximum energy deposited one among the fibers which have gotten energy over 10MeV. The fibers which have gotten energy less than 5MeV were grouped as decay particles' loci because of the decay particles can be assumed passing with the minimum ionization. For selecting a good event, we required the following conditions.
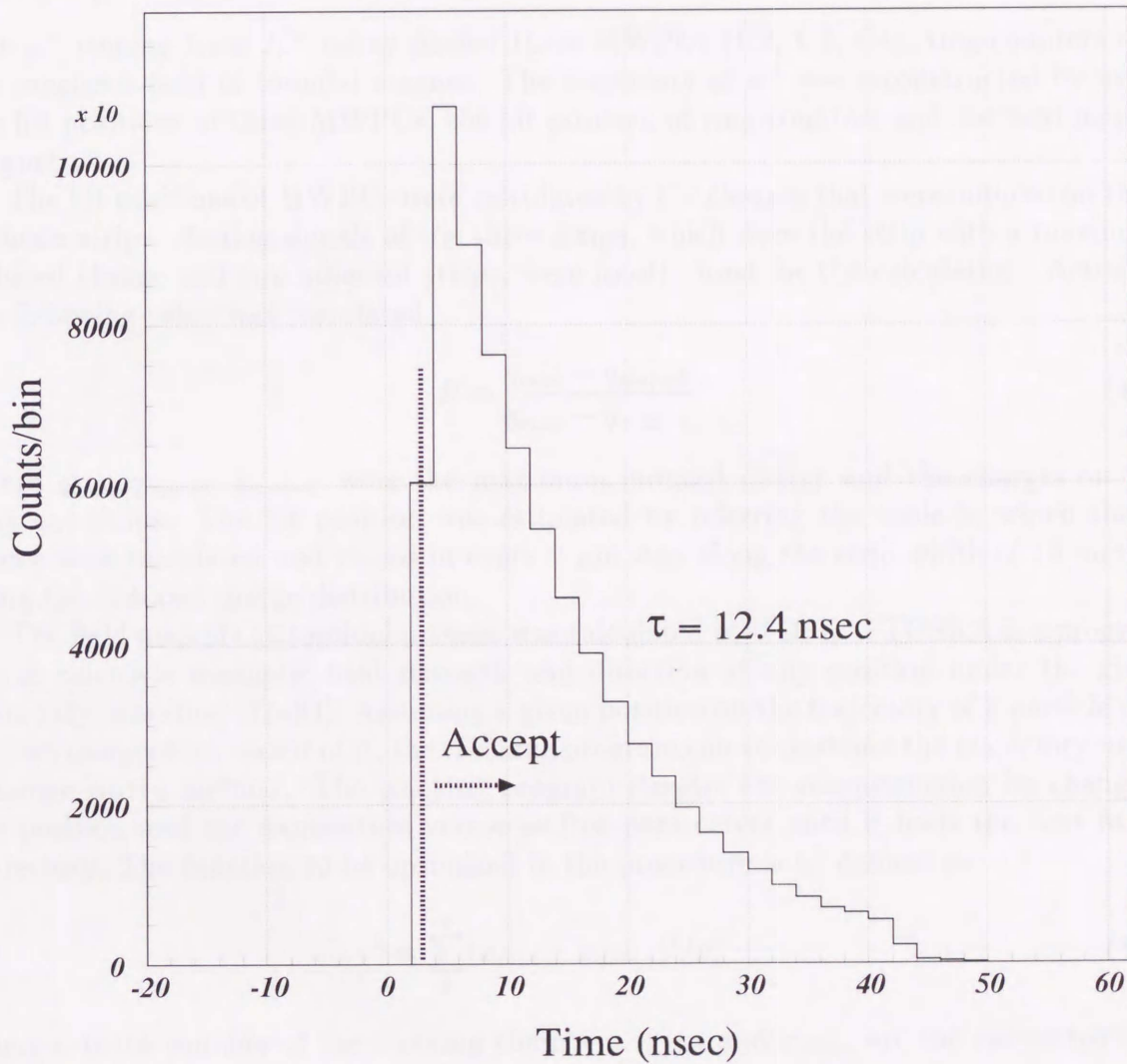
Figure 4.1: Spectrum of the time difference between the Čerenkov counter and the target fiducial counter. The events with greater than 3 nsec difference were accepted as true ones.

- The event has only one K^+ decay vertex.

- The decay particle's loci align along a straight line from the K^+ decay vertex to the fiducial counter.

4.1.3 μ^+ momentum analysis

The μ^+ coming from K^+ decay passed three MWPCs (C2, C3, C4), ring-counters and the magnetic field of toroidal magnet. The trajectory of μ^+ was reconstructed by using the hit positions of three MWPCs, the hit position of ring-counters and the field map of magnet.

The hit positions of MWPCs were calculated by the charges that were induced on their cathode strips. Analog signals of the three strips, which were the strip with a maximum induced charge and two adjacent strips, were mostly used for the calculation. Actually, the following value was calculated.

$$R = \frac{q_{max} - q_{max+1}}{q_{max} - q_{max-1}} \tag{4.1}$$

where $q_{max}, q_{max+1}, q_{max-1}$ were the maximum induced charge and the charges on the adjacent strips. The hit position was estimated by referring the table in which the R values were calculated and stored in every 2 μm step along the strip width of 10 mm by using the induced charge distribution.

The field map of the toroidal magnet was calculated by TOSKA. TOSKA is a program which calculate magnetic field strength and direction at any position under the given boundary condition [Tos93]. Assuming a given position on the trajectory of a particle and a given momentum vector of it, the tracking program can reconstruct the trajectory using a Lunge-Kutta method. The tracking program iterates the reconstruction by changing the position and the momentum vector as free parameters until it finds the best fitted trajectory. The function to be optimized in the procedure is χ^2 defined as

$$\chi^2 = \sum_i^n (x_{fit,i} - x_{data,i})^2 / \sigma_i^2 \tag{4.2}$$

where n is the number of the tracking chambers. $x_{fit,i}$ and $x_{data,i}$ are the calculated and experimental hit positions of the i-th chamber. σ_i is the weighting factor due to the detector resolution. The resolution used for the tracking was 200 μm in common for C2, C3, and C4 chambers. Each iteration works so that the first derivatives of χ^2 become zero gradually step by step. It stops when the current value of χ^2 changes only in a range less than 1, or the χ^2 diverges after 15 steps. The distribution of χ^2 was shown in Fig.2.10. The χ^2 region of success in tracking was under 150.

The momentum resolution of the charged particle which was passed the spectrometer was evaluated by π^+ of $K_{\pi 2}$ two body decay. Fig.4.3 showed the momentum spectrum of the particles which were collected as π^+. In this figure, the resolution of the momentum was given as a width of $K_{\pi 2}$ monochromatic peak (205Mev). Thus the momentum resolution of the charged particle was $\sigma \sim 3.0 MeV$.
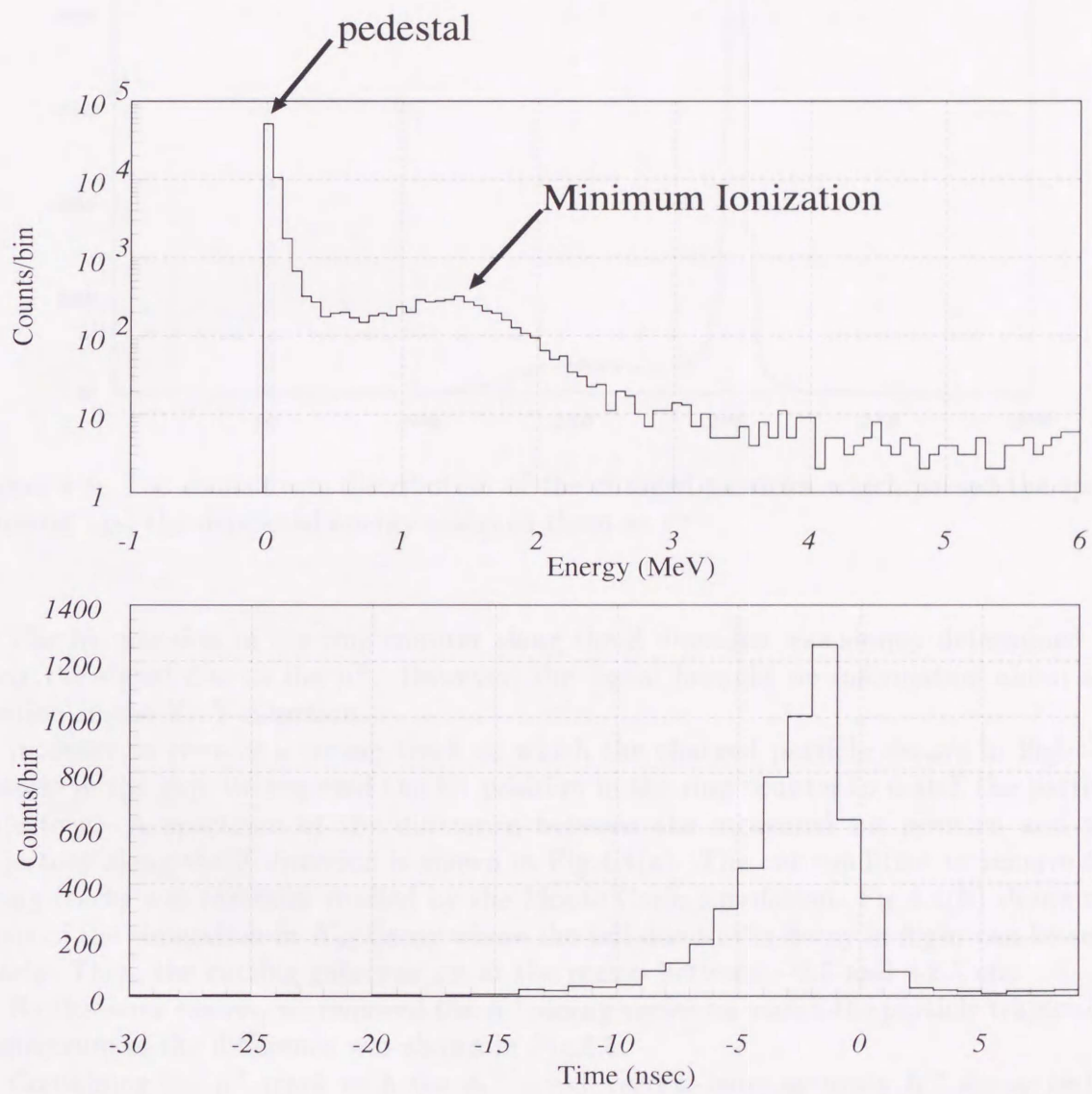
Figure 4.2: Typical ADC and TDC spectra measured by the target fiber.
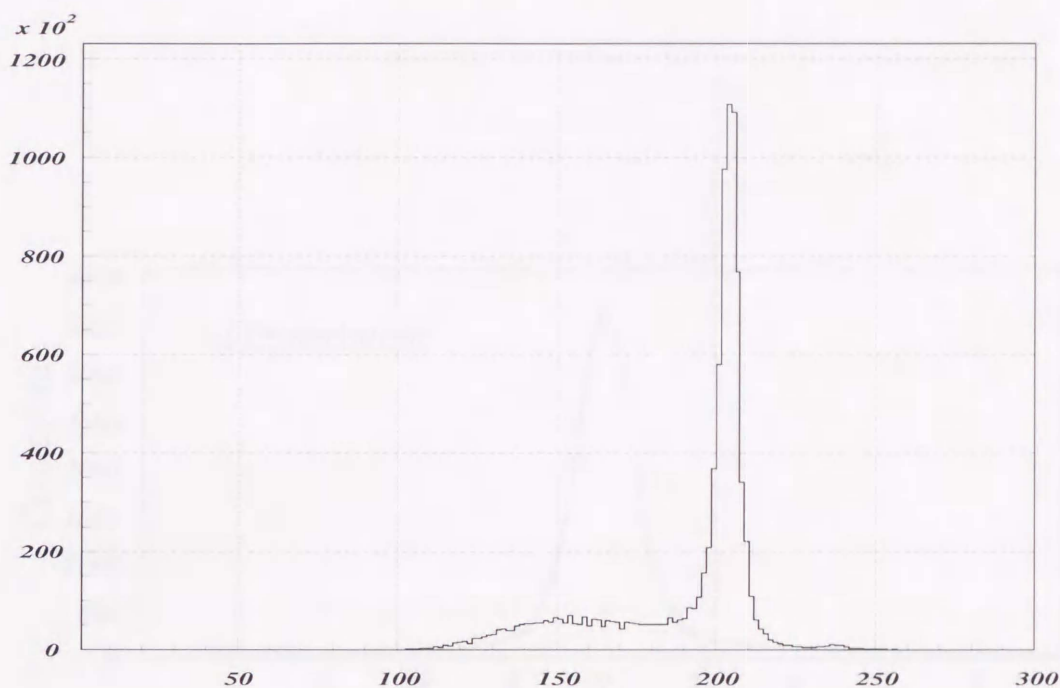
Figure 4.3: The momentum distribution of the charged particles which passed the spectrometer and the deposited energy assigned them as π^+.

The hit position of the ring counter along the Z direction was simply determined by using the signal due to the μ^+. However, the signal brought no information about the position in the X−Y direction.

In order to remove a wrong track in which the charged particle decays in flight or scatters in the gap, we required the hit position in the ring counter to match the particle trajectory. A spectrum of the difference between the measured hit position and the trajectory along the Z direction is shown in Fig.4.4(a). The cut condition to remove the wrong tracks was carefully studied by the Monte Carlo simulation. Fig.4.4(b) shows the result of the simulation in $K_{\pi2}$ decay where the tail due to the decay in flight can be seen clearly. Then, the cutting gate was set at the region between −2.5 and +2.5 cm.

By the same reason, we required the K^+ decay vertex to match the particle trajectory. A spectrum of the difference was shown in Fig.4.5.

Combining the μ^+ track with the K^+ decay vertex, more accurate K^+ decay vertex could be calculated. The decay vertex was redefined as the nearest point to the trajectory.

4.1.4 TOF analysis

In the acceptance of the toroidal magnet, there were some particles coming from other decay modes. They were μ^+ from $K_{\mu3}$, e^+ from K_{e3}, π^+ from $K_{\pi2}$ and μ^+ from $K_{\mu2}$. Using the momentum measured by the spectrometer and the velocity calculated by using both the TOF and the flight length of the particle, we could reconstruct the particle mass.
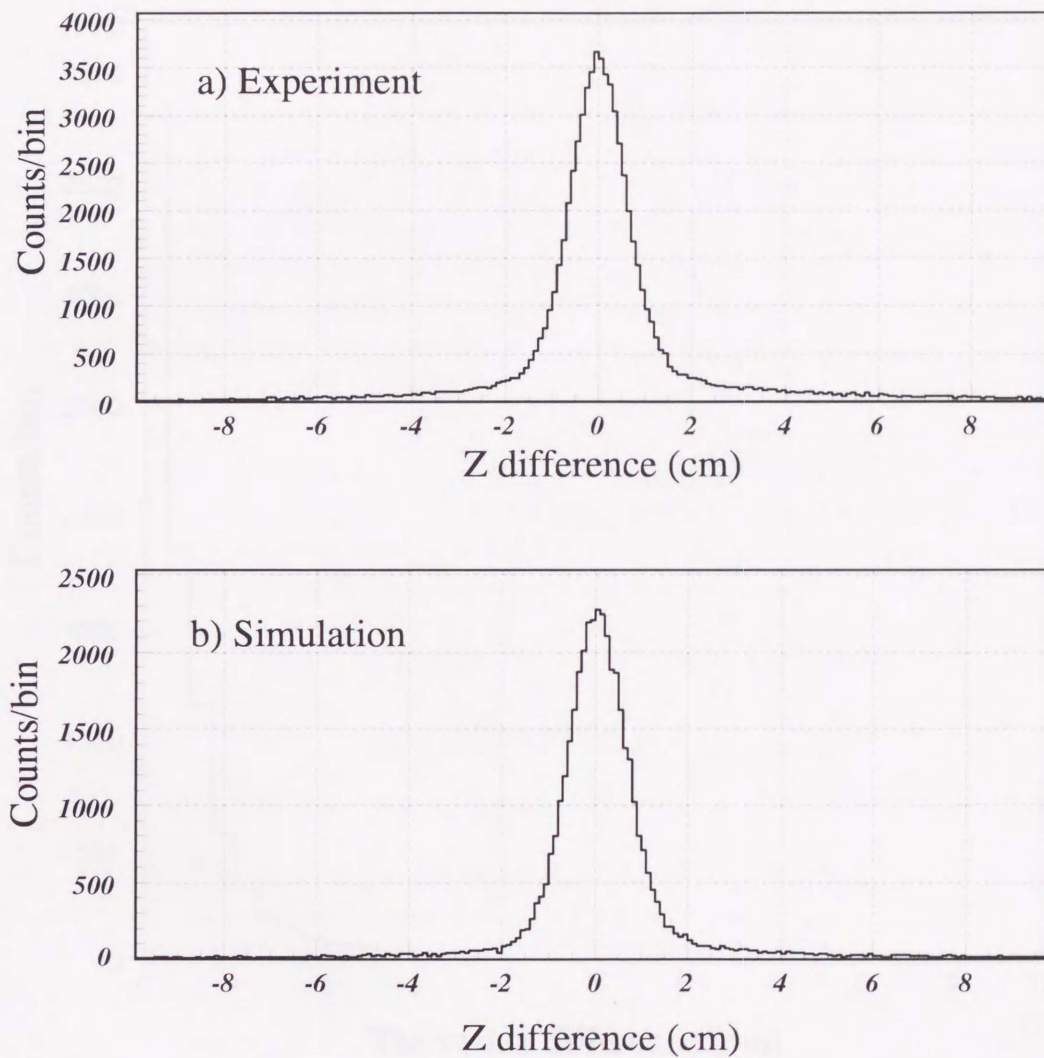
Figure 4.4: Z-difference between the hit position in the ring counter and the trajectory. (a): experiment. (b): simulation.
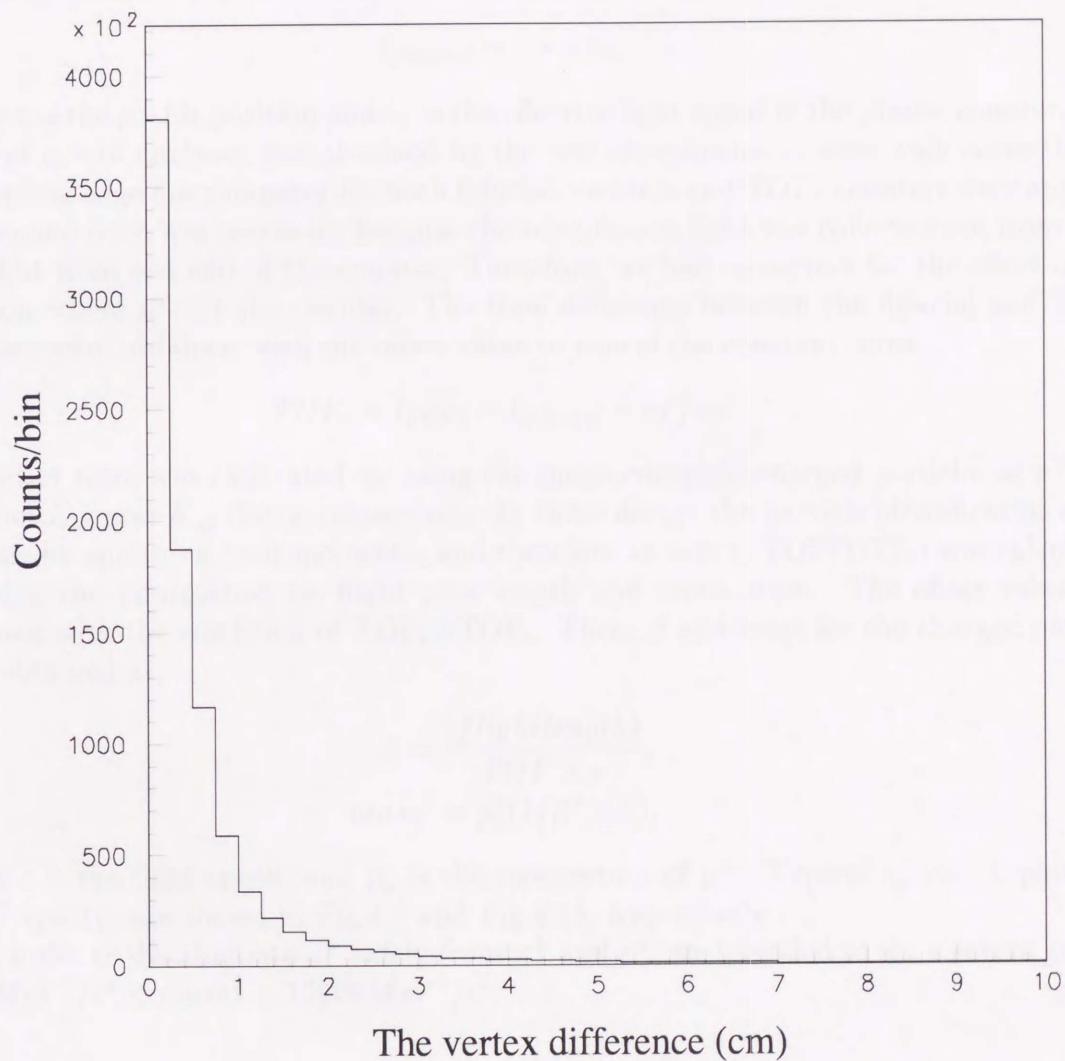
Figure 4.5: The difference between the K^+ decay vertex determined by the active target and one determined by the trajectory of the track

Observing the reconstructed mass, we could extract μ^+ from $K_{\mu 3}$.

For the TOF measurement, we used TOF2 counters and fiducial counters. The time (t_{TOF2}) when the TOF2 counter detected a particle was defined as an average value of the times measured by the inner PMT (t_{inner}) and the outer PMT (t_{outer}) as follows.

$$t_{TOF2} = (t_{inner} + t_{outer})/2 \tag{4.3}$$

The time $t_{fiducial}$ when the fiducial counter detected a particle was defined as Eq.(4.4).

$$t_{fiducial} = t + x/c_n \tag{4.4}$$

where x is the μ^+ hit position and c_n is the effective light speed in the plastic counter. The value of c_n=18 cm/nsec was obtained by the test experiment. A time-walk correction of the leading edge discriminator for both fiducial counters and TOF2 counters were applied. The second term was necessary because the scintillation light was collected not from both ends but from one end of the counter. Therefore, we had to correct for the effect of the position where μ^+ hit the counter. The time difference between the fiducial and TOF2 counters were obtained with the offset value to cancel the constant term.

$$TOF_a = t_{TOF2} - t_{fiducial} + offset \tag{4.5}$$

The offset term was calibrated by using the mono-energetic charged particles of π^+ and μ^+ from $K_{\pi 2}$ and $K_{\mu 2}$ decay, respectively. In these decays the particle identification could be done by analyzing their momenta, and therefore an actual TOF(TOF_b) was calculated by using the information on flight pass length and momentum. The offset value was obtained with the condition of TOF_a=TOF_b. Then, β and mass for the charged particle were obtained as,

$$\beta = \frac{(flightlength)}{TOF \times c}, \tag{4.6}$$

$$mass^2 = p_\mu^2(1/\beta^2 - 1). \tag{4.7}$$

where c is the light speed, and p_μ is the momentum of μ^+. Typical p_μ v.s. β plot and $mass^2$ spectra are shown in Fig.4.6 and Fig.4.18, respectively.

In order to discriminate μ^+ safely from π^+ and e^+, we intended to set a severe gate of $8000 MeV^2/c^4 < mass^2 < 15000 MeV^2/c^4$.

4.1.5   CsI(Tl) photon detector

Photons from the π^0 decay were detected by the CsI(Tl) crystals. These photons produced the electro-magnetic shower in the CsI(Tl) crystals, sharing their energy into several modules (photon cluster). Therefore, the photon energy was obtained by summing up the energies of these modules belonging to the photon cluster while the hit position of photon was calculated by an energy-weighted centroid of the modules. The photon cluster was constructed by the following procedure. First, seed crystals which had a large energy deposit (larger than 20 MeV) were searched, and a seed cluster was formed by grouping adjacent seed crystals. Then, the crystals adjacent to the seed cluster were assigned as a member of the photon cluster. Fig.4.8 shows a typical example of the cluster construction.
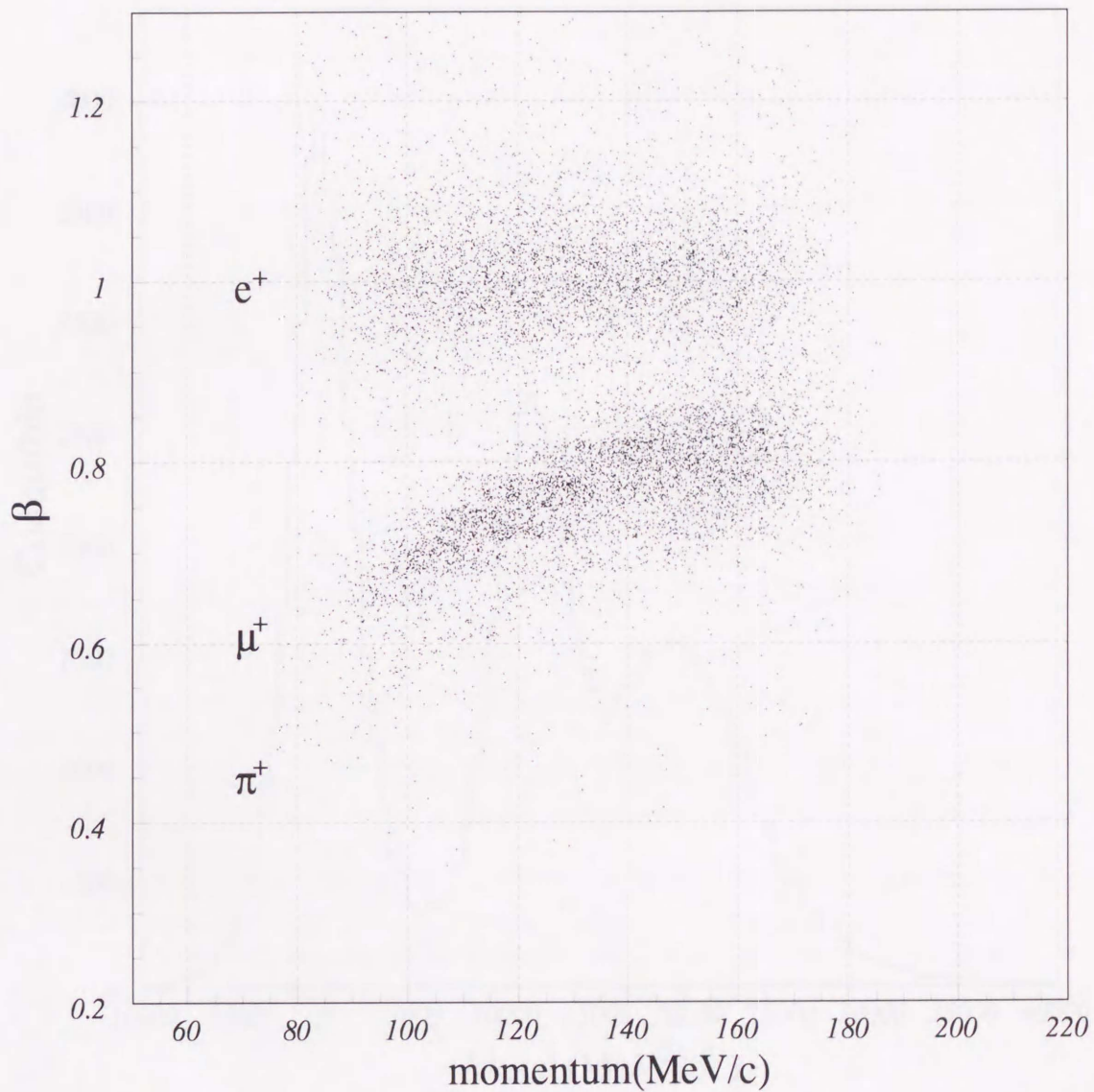
Figure 4.6: β (velocity) obtained by the TOF measurement and the momentum plot for the e^+, μ^+, and π^+ particles.
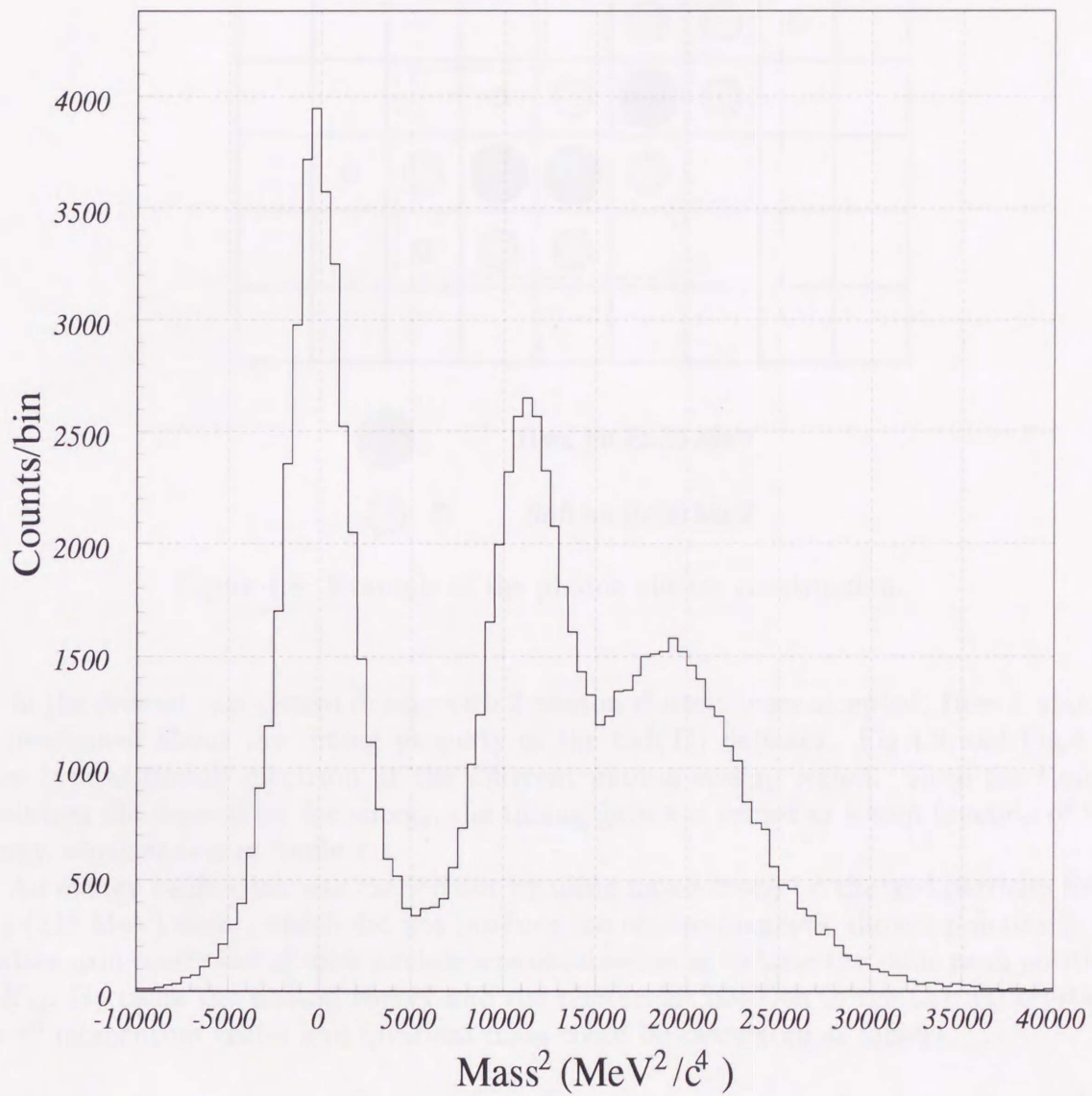
Figure 4.7: Typical mass^2 spectrum obtained by the TOF measurement. e^+, μ^+, and π^+ peaks can be seen clearly.
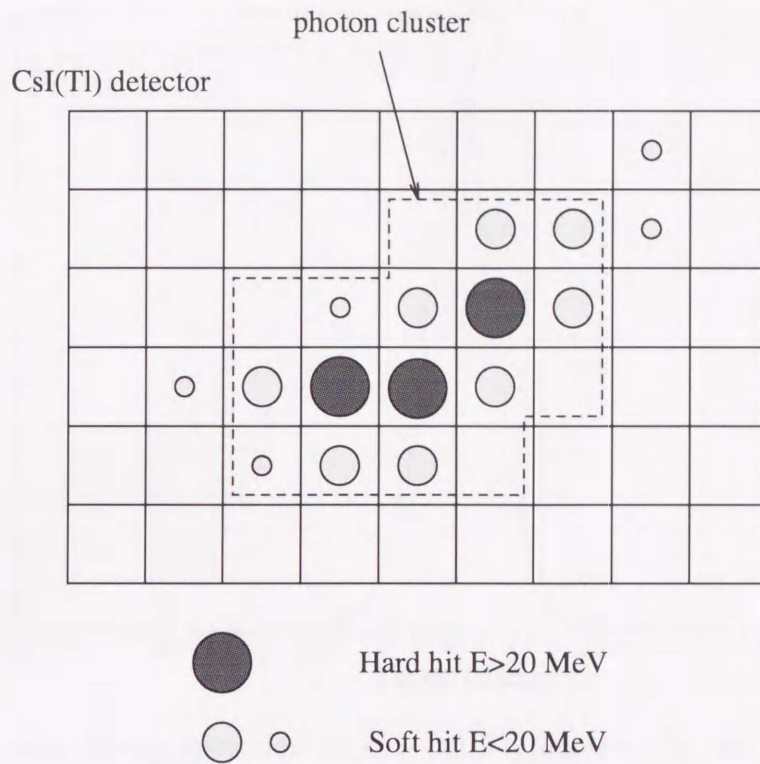
Figure 4.8: Example of the photon cluster construction.

In the present experiment events with 2 photon clusters were accepted. Here it should be mentioned about the timing property of the CsI(Tl) detector. Fig.4.9 and Fig.4.10 show typical timing spectrum at the different photon energy region. Since the timing resolution did depend on the energy, the timing gate was varied as a step function of the energy which shown in Table 4.1.

An energy calibration was carried out by using mono-energetic charged particles from $K_{\pi 2}$ (245 MeV) decay, which did not produce the electro-magnetic shower practically. A relative gain coefficient of each module was obtained so as to have the same peak position of $K_{\pi 2}$. By using the photon energy and the photon hit position in the CsI(Tl) crystals, the π^0 momentum vector and invariant mass could be calculated as follows.

$$\vec{p}_{\pi^0} = \vec{p}_{\gamma_1} + \vec{p}_{\gamma_2}, \tag{4.8}$$

$$E_{\gamma\gamma} = E_{\gamma_1} + E_{\gamma_2}, \tag{4.9}$$

$$M_{\gamma\gamma} = \sqrt{2 \cdot E_{\gamma_1} E_{\gamma_2} (1 - \cos\theta)}. \tag{4.10}$$

where p is the momentum vector, E is the photon energy, and θ is the opening angle of photons. Fig.4.11 and Fig.4.12 show typical energy spectrum ($E\gamma\gamma$) and mass spectrum ($M_{\gamma\gamma}$) of the π^0 from the $K_{\pi 2}$ decay, where the π^0 energy is 245 MeV. An absolute gain coefficient was determined by comparing experimental $E_{\gamma\gamma}$ of the π^0 from the $K_{\pi 2}$ decay with the simulation. The low energy tail of $E_{\gamma\gamma}$ spectra is due to the shower leakage. The
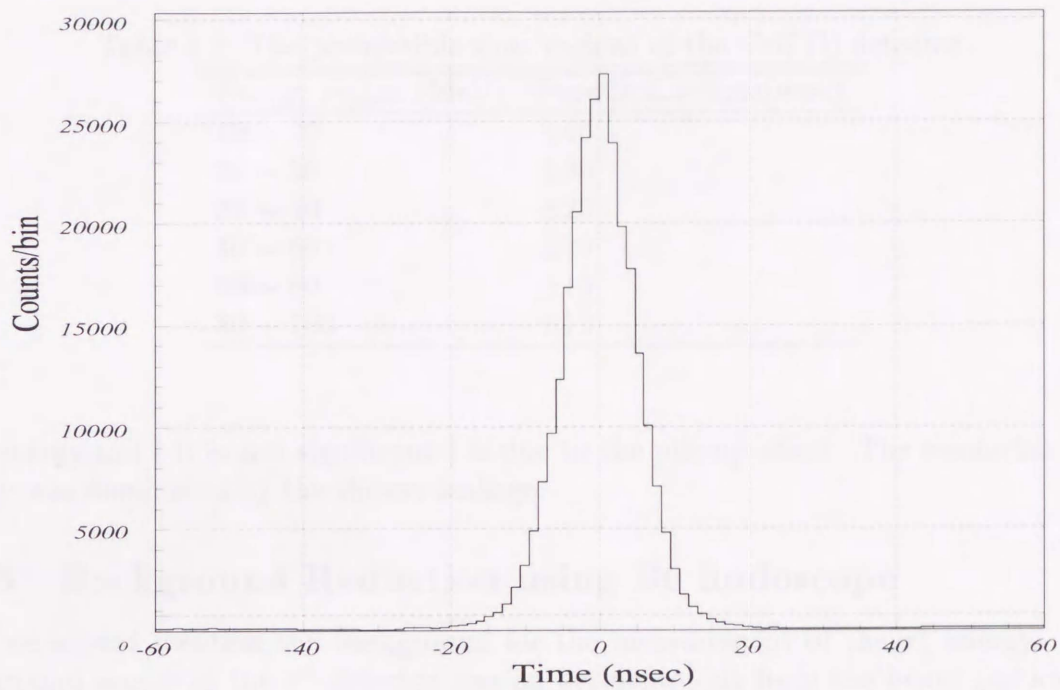
Figure 4.9: Typical timing spectrum of the CsI(Tl) detector in the region, 40MeV< E_γ <60MeV
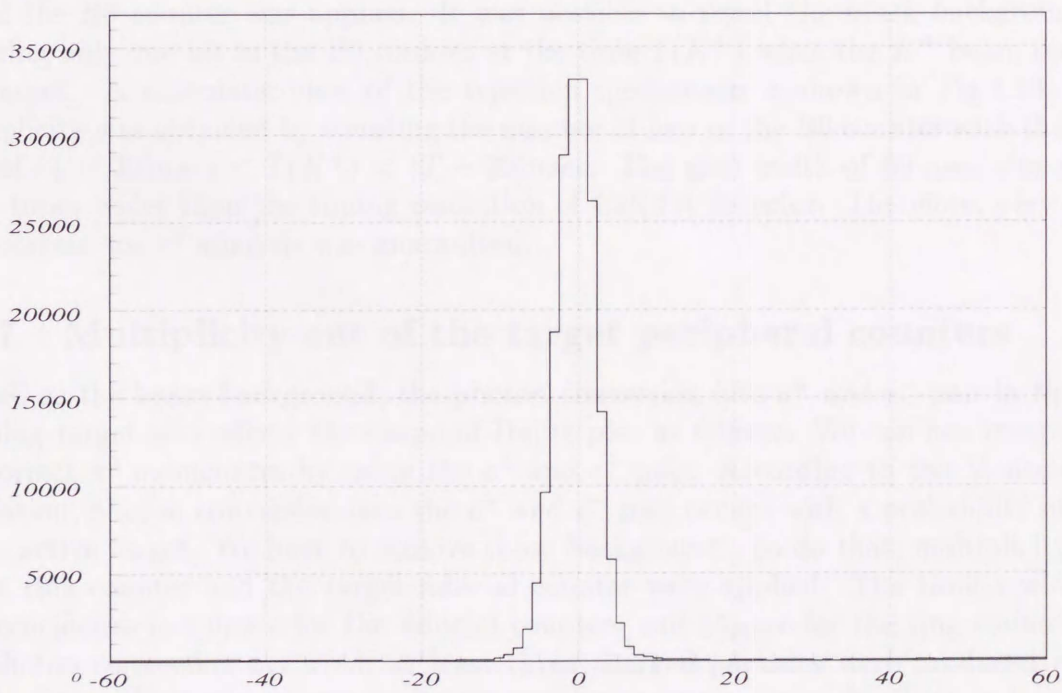
Figure 4.10: Typical timing spectrum of the CsI(Tl) detector for the γ ray, E_γ >100MeV.

Table 4.1: The permissible time regions of the CsI(Tl) detector

Energy region (MeV)	Permissible time(nsec)
$10 \sim 20$	± 45
$20 \sim 30$	± 30
$30 \sim 40$	± 25
$40 \sim 60$	± 20
$60 \sim 80$	± 15
$80 \sim 100$	± 12

high energy tail (it is not significant) is due to the pile-up effect. The resolution of π^0 energy was dominated by the shower leakage.

4.1.6 Background Reduction using B0 hodoscope

Here we should mention the background for the measurement of the π^0 energy. Main background source of the π^0 detector was an accidental hit from the beam particles. If one of two photons from the π^0 decay passed through a hole and a beam particle hits the CsI(Tl) barrel within the timing gate accidentally, such a event could be accepted as the true ones from the π^0 decay. Even though we can reject the accidental hit by using the TDC of the CsI(Tl) modules to some extent, background must remain in the accepted region as shown in Fig.4.9. In order to remove these events, the multiplicity cut of the B0 counter was applied. It was possible to reject the beam background by requiring only one hit in the B0 counter at the time $T(K^+)$ when the K^+ beam reached the target. A schematic view of the rejection mechanism is shown in Fig.4.13. The multiplicity was obtained by counting the number of hits in the B0 counter with the time gate of $(T - 30)nsec < T(K^+) < (T + 30)nsec$. The gate width of 60 nsec was about three times wider than the timing resolution of CsI(Tl) detector. Therefore, very clean environment for π^0 analysis was guaranteed.

4.1.7 Multiplicity cut of the target peripheral counters

As well as the beam background, the photon conversion into e^+ and e^- pair in the K^+ stopping target also affects the shape of Dalitz plot as follows. We can not reconstruct the correct π^0 momentum by using the e^+ and e^- pair. According to the Monte Carlo simulation, photon conversion into the e^+ and e^- pair occurs with a probability of 14% in the active target. We have to remove those background. To do that, multiplicity cuts of the ring counter and the target fiducial counter were applied. The timing width of the coincidence is $1.0\mu sec$ for the fiducial counters and $14\mu sec$ for the ring counters. If the photon conversion occurred, at least three charged particles were produced in the target. Thus, those events were easily rejected by requiring the multiplicity to be one in both the ring counter and the fiducial counter. After applying the multiplicity cuts of the B0 counter, the fiducial counter and the ring counter, the contamination of the above
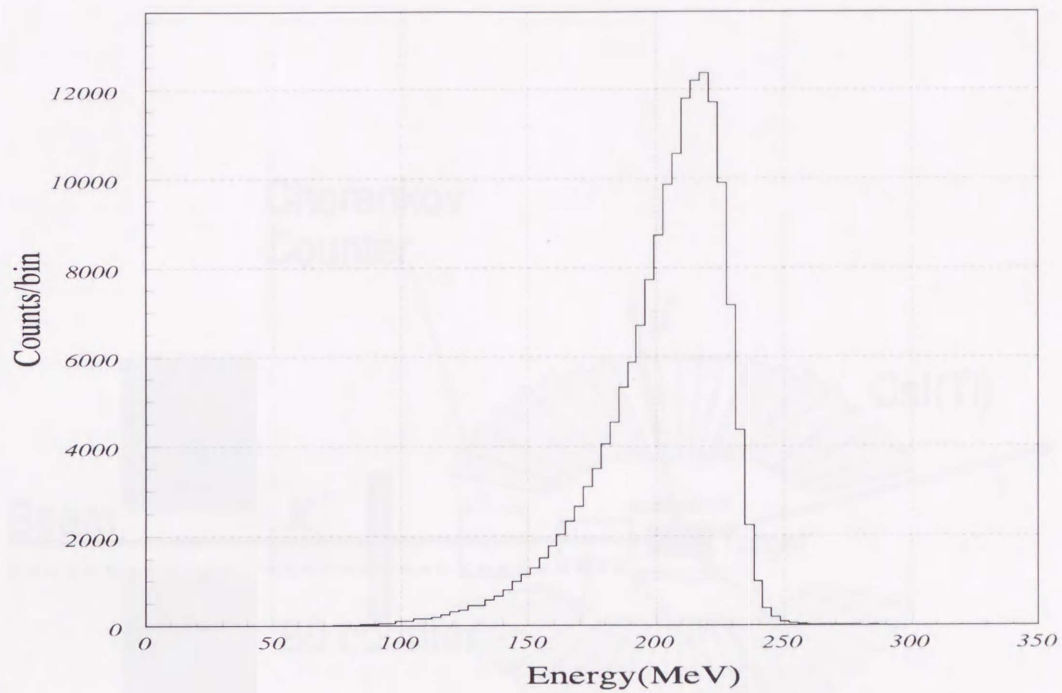
Figure 4.11: Energy sum of two photons from π^0 in $K_{\pi 2}$ decay.
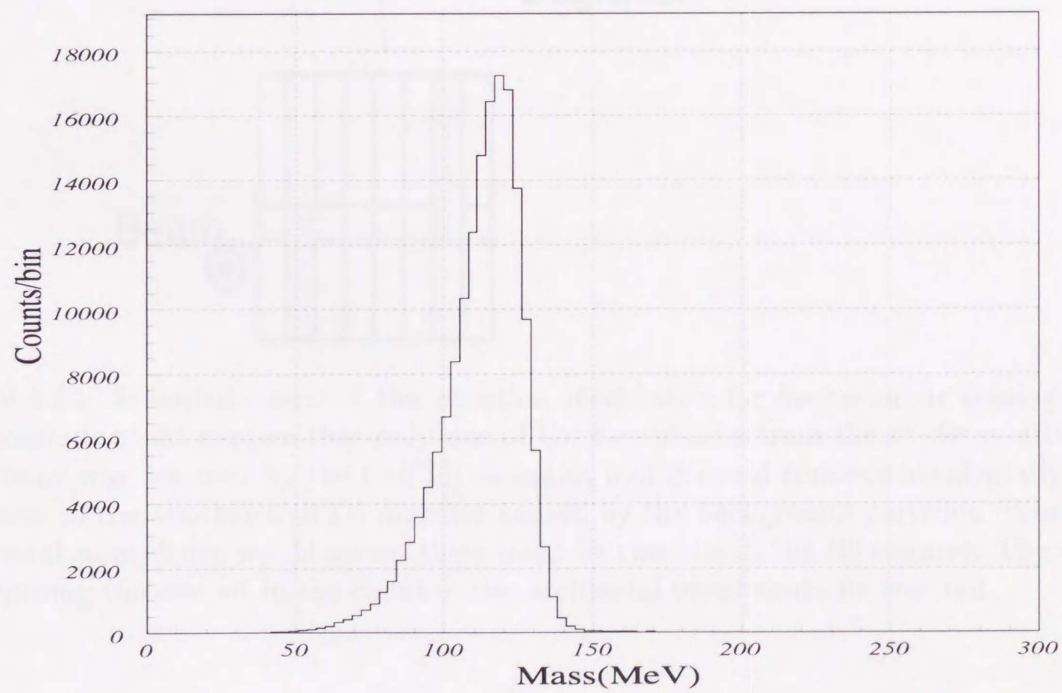
Figure 4.12: Reconstructed π^0 mass spectrum from $K_{\pi 2}$ decay.
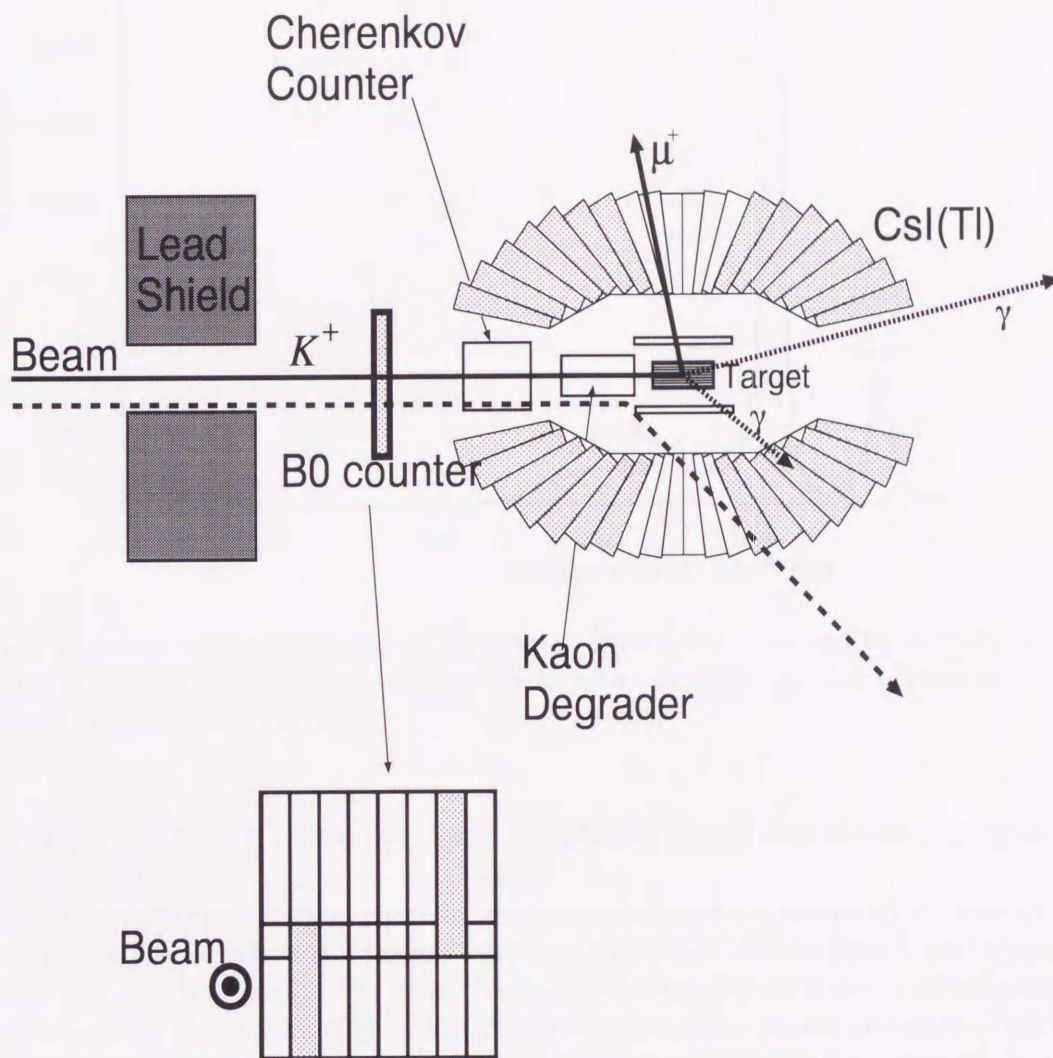
Figure 4.13: Schematic view of the rejection mechanism for backgrounds coming from the beam. It could happen that only one of the two photon from the π^0 decay after the $K_{\mu 3}$ decay was detected by the CsI(Tl) detector, and it could coincide accidentally with the event of the another CsI(Tl) detector caused by the background particles. When the accidental coincidence would occur, there must be two hits in the B0 counter. Therefore, by requiring the one hit in the counter, the accidental event could be rejected.
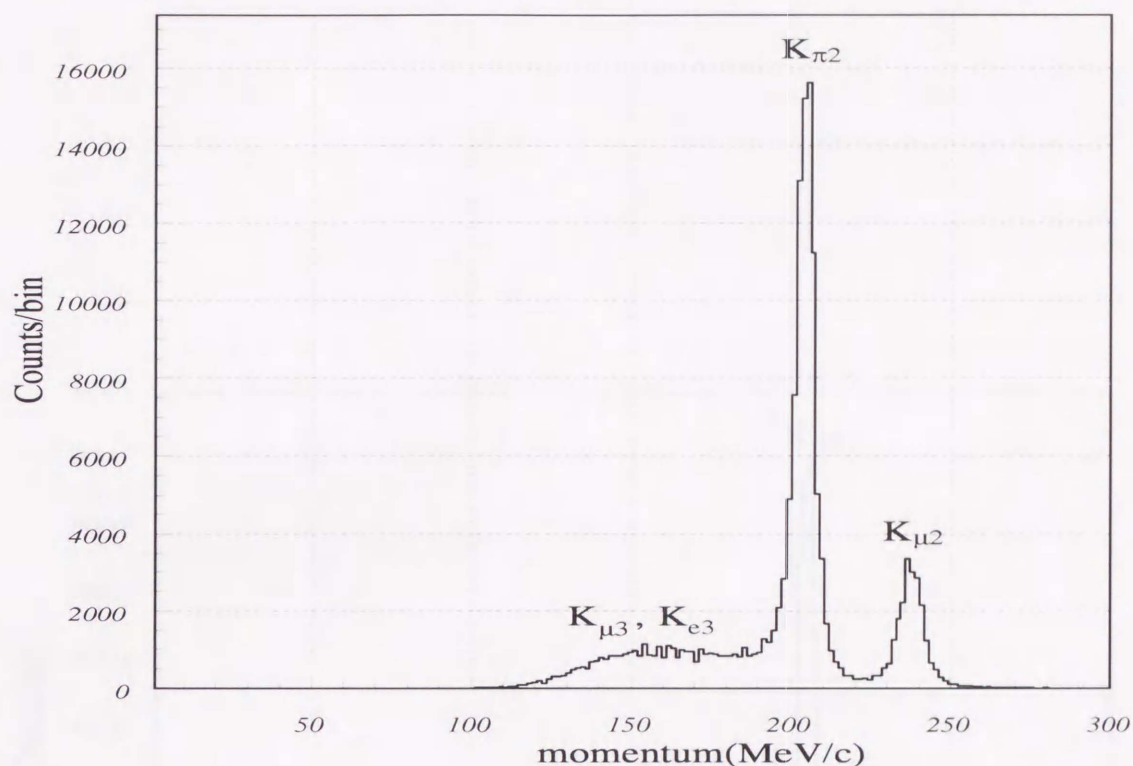
Figure 4.14: Momentum spectrum of the charged particles obtained by correcting for the energy loss in the target. Mono—energy peaks of π^+ and μ^+ particles from the $K_{\pi 2}$ and $K_{\mu 2}$ decay, respectively, are seen.

mentioned accidental hit of the beam and the photon conversion was estimated less than 0.5%.

Fig.4.14 shows the charged particle momentum spectrum obtained by correcting for the energy loss in the active K^+ target. Mono-energy peaks due to the π^+ and μ^+ particles from the $K_{\pi 2}$ and $K_{\mu 2}$ decays are seen. We required two photon clusters at online trigger. Here, the peak of $K_{\mu 2}$ was caused by any backgrounds on the photon detector. Further cut of multiplicity of the B0 counter, the fiducial counter and the ring counter could exclude μ^+ peak as shown in Fig.4.15.

4.2 $K_{\mu 3}$ and $K_{\pi 2}$ Event Selection

4.2.1   back ground reduction

The event selection which works to pick up good events of $K_{\mu 3}$ and $K_{\pi 2}$ decays is summarized as follows.

(1) K^+ energy deposit in the stopping target must be lager than 5 MeV to select the stopped K^+ and to reject the events due to the K^+ decay in flight in the BeO degrader.
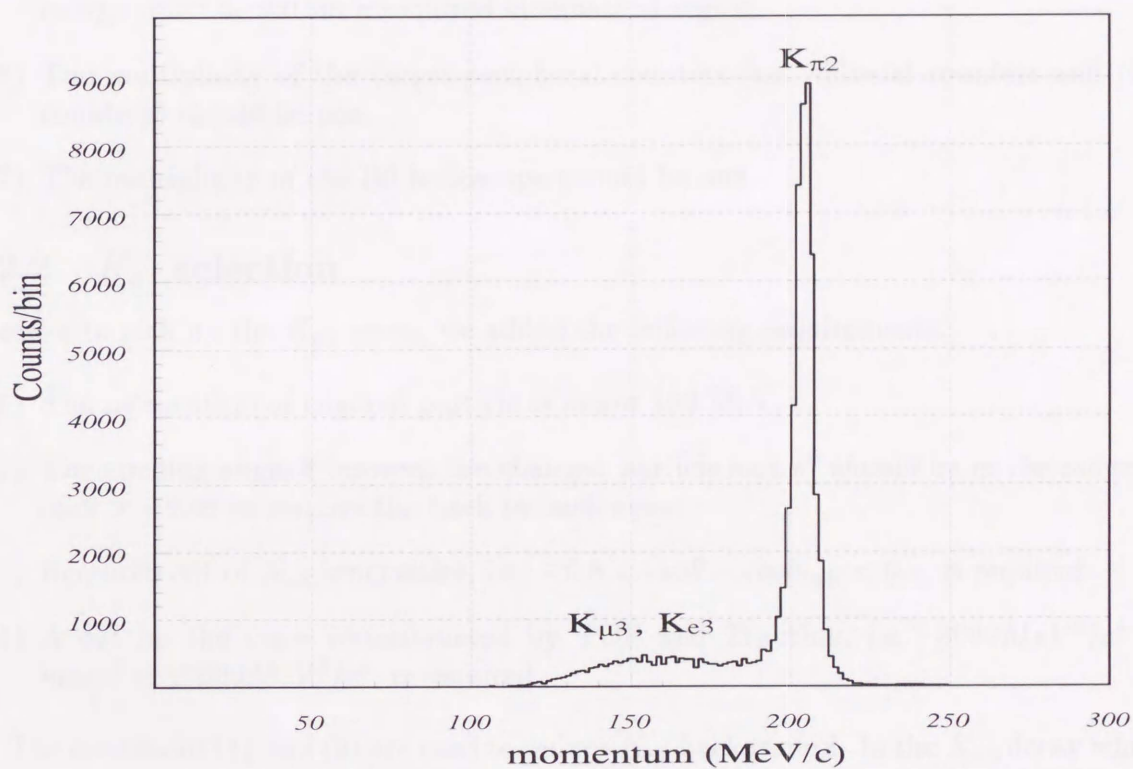
Figure 4.15: Momentum spectrum of the charged particles from K^+ decays obtained by requiring the multiplicity cuts of the B0 counter, the fiducial counter, and the ring counter. It should be noted that the events from the $K_{\mu2}$ decay were removed.

(2) The timing of K^+ decay should be at least 3 nsec after the timing of K^+ coming to reject the events due to K^+ decay in flight.

(3) An extrapolation of charged particle trajectory reconstructed by C2, C3, and C4 chambers' hits should match the charged particle hit position in the ring counter within 2.5cm.

(4) An extrapolation of charged particle trajectory should match the K^+ vertex position in the fiber target within 2.5cm.

(5) π^0 can be reconstructed. There must be two photon clusters and the reconstructed energy must be within a required kinematical region.

(6) The multiplicity of the target-peripheral counters (i.e. fiducial counters and ring counters) should be one.

(7) The multiplicity of the B0 hodoscope should be one.

4.2.2 $K_{\mu 3}$ selection

In order to pick up the $K_{\mu 3}$ event, we added the following requirements.

(1) The momentum of charged particle is below 180 MeV/c.

(2) The opening angle θ between the changed particle and π^0 should be in the range of $cos\theta > -0.96$ to remove the back to back event.

(3) Requirement of $K_{\mu 3}$ kinematics, i.e. $-0.8 < cos\theta - cos\theta_{byE} < 0.1$, is required.

(4) A cut on the mass reconstructed by TOF and Tracking, i.e. $8000 MeV^2/c^4 < mass^2 < 15000 MeV^2/c^4$, is required.

The conditions (1) and (2) are used to reduce $K_{\pi 2}$ background. In the $K_{\pi 2}$ decay which is a two body decay, decay products have a monochromatic momentum (205MeV/c) and their directions are back-to-back. The distribution of the opening angle was shown in Fig.4.16. The condition (3) is the condition of the kinematical constraint. Our photon detector can measure the directions and the energies of the photons. Therefore, the opening angle between K^+ and π^0 is measured by the two methods, the direct reconstruction and the reconstruction from the photon energies, under the assumption of $K_{\mu 3}$ decay as shown in the following equation.

$$cos\theta_{byE} = \frac{M_{K^+}^2 + M_{\pi^0}^2 + M_{\mu^+}^2 - 2M_{K^+}(E_{\pi^0} + E_{\mu^+}) + 2E_{\pi^0}E_{\mu^+}}{2\sqrt{E_{\pi^0}^2 - M_{\pi^0}^2}\sqrt{E_{\mu^+}^2 - M_{\mu^+}^2}} \qquad (4.11)$$

where $M_{K^+}, M_{\pi^0}, M_{\mu^+}$ were the mass of the each particles and E_{π^0}, E_{μ^+} were the energies of one. The event in which the opening angles obtained by these two methods agree each other was identified as a true event. The distribution of the opening angle is shown in Fig.4.17.
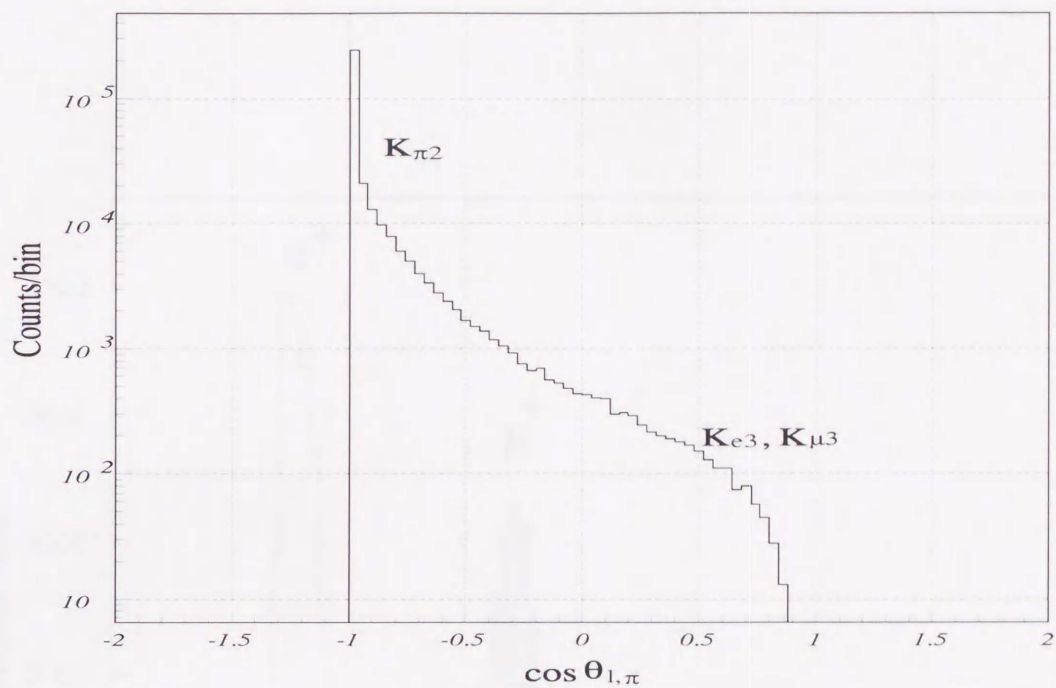
Figure 4.16: Opening angle distribution between the charged particle and the π^0.
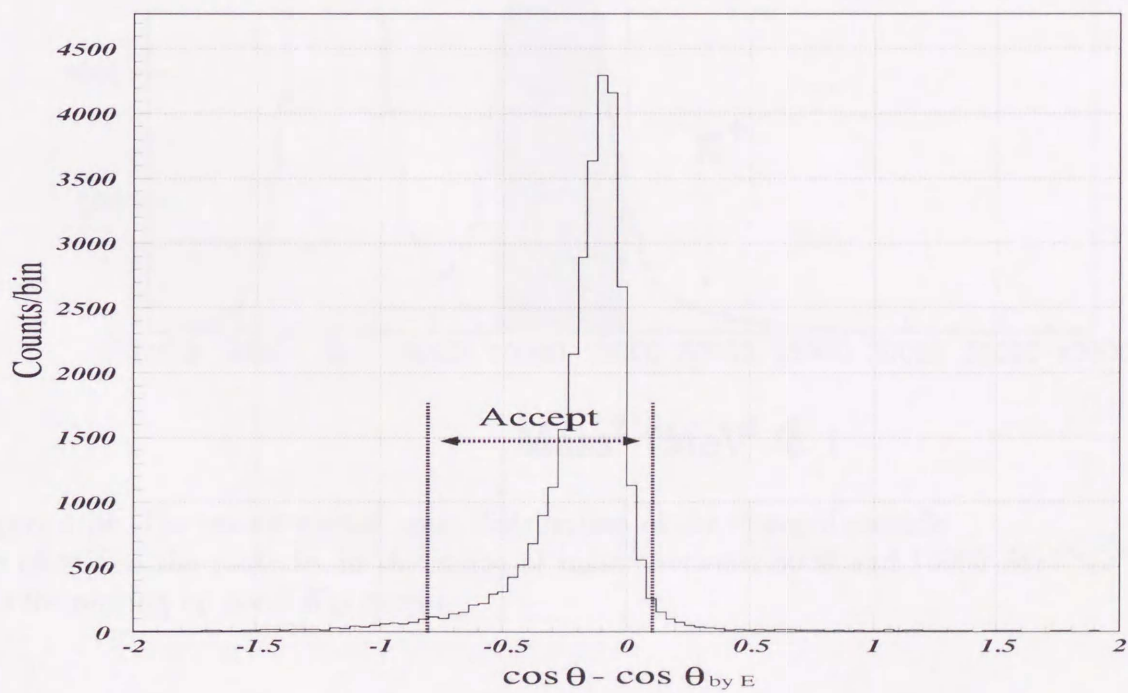
Figure 4.17: The distribution of $cos\theta - cos\theta_{byE}$, where $cos\theta$ is an opening angle between the charged particle and the π^0. $cos\theta_{byE}$ is reconstructed from the photon energies.
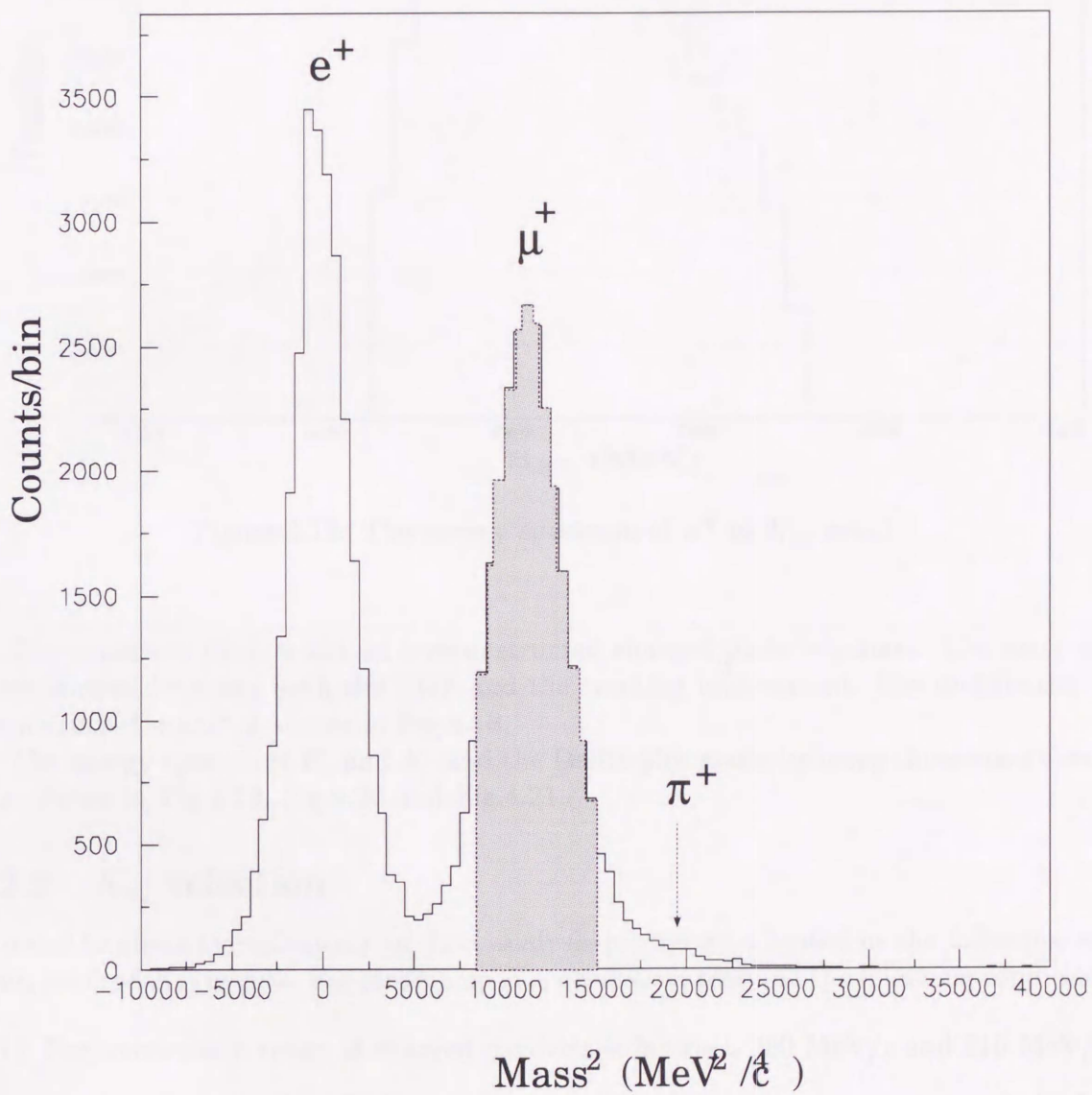
Figure 4.18: The reconstructed mass distribution of the charged particle.
We identified the particles in the range of mass^2 between 8000 and 15000 MeV^2/c^4 as μ^+s for picking up good $K_{\mu3}$ events
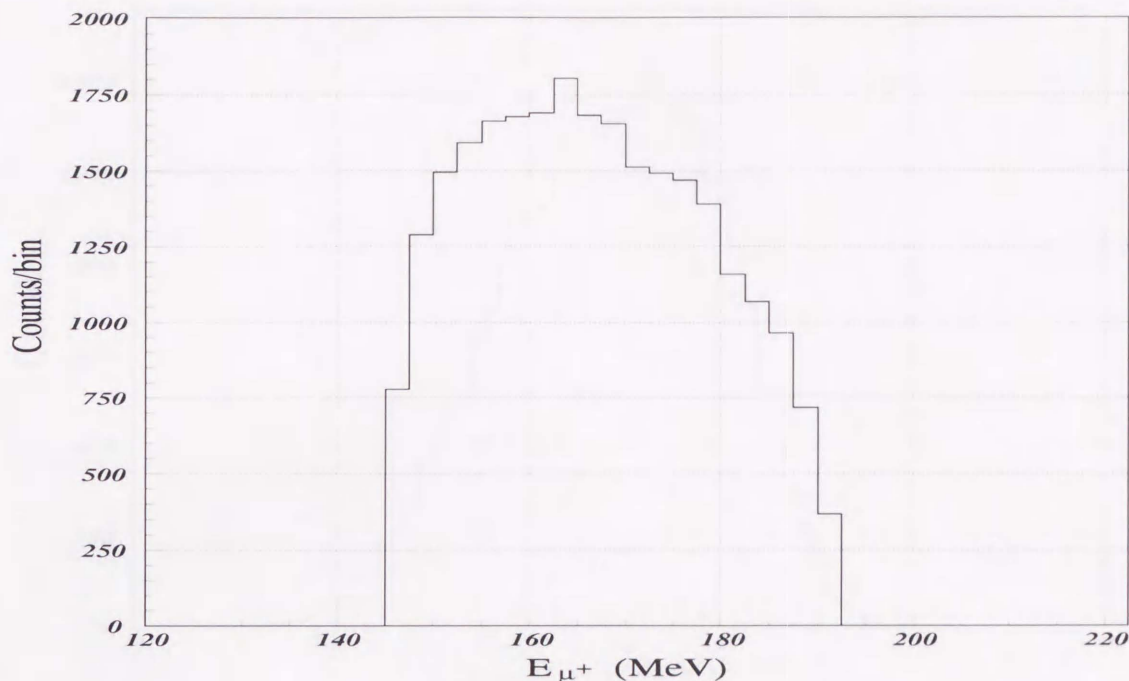
Figure 4.19: The energy spectrum of μ^+ in $K_{\mu 3}$ event

The condition (4) is a cut on a reconstructed charged particle's mass. The mass was reconstructed by using both the TOF and the tracking information. The distribution of reconstructed $mass^2$ is shown in Fig.4.18.

The energy spectra of E_μ and E_π and the Dalitz plot made by using these good events were shown in Fig.4.19, Fig.4.20 and Fig.4.21.

4.2.3 $K_{\pi 2}$ selection

In order to check the adequacy of data analysis procedure adopted in the following sections, we used $K_{\pi 2}$ events. For picking up $K_{\pi 2}$ events, we required the following conditions.

(1) The momentum range of charged particles is between 200 MeV/c and 210 MeV/c

(2) For $mass^2$ obtained by TOF measurement, $15000 MeV^2/c^4 < mass^2 < 40000 MeV^2/c^4$

(3) Cosine of opening angle between charged particle and π^0 is smaller than -0.98

4.3   Monte Carlo Simulation

In order to obtain the form factors from the measured data, it was needed to understand precisely the experimental acceptance and the responses of the spectrometer and the photon detectors. For this purpose, a Monte Carlo simulation was used.
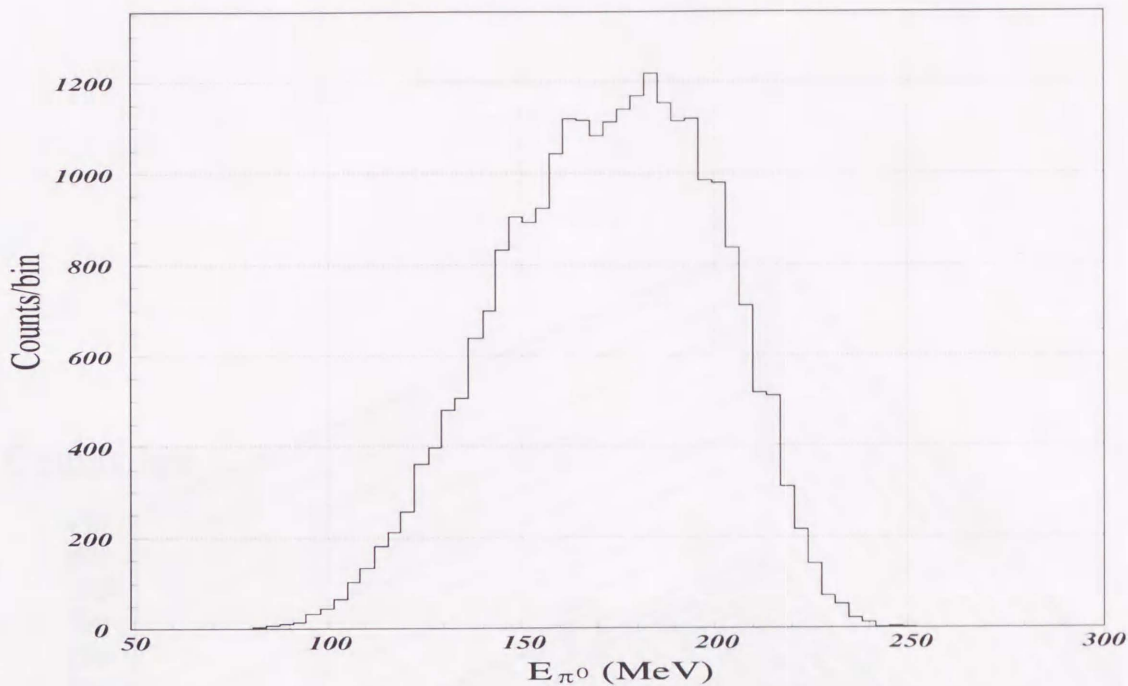
Figure 4.20: The energy spectrum of π^0 in $K_{\mu 3}$ event

The simulation program was developed based on GEANT. GEANT is a general simulation libraries for high energy physics. It was developed and distributed by CERN. The accuracy of the basic interaction incorporated and the behavior of GEANT were known to be correct. Many experiments have also proved that GEANT was reliable. In this program, all the detector materials, all the detector subsystem, the toroidal magnet and the magnetic field are included as they are in reality. (Fig.4.22) This program simulates all daughter particles from K^+decay in the K^+ stopping target until being vanished or escaping the detector.

In this section, a fairly well agreement of the Monte Carlo simulation program to the real experiment is presented and an estimation of the possible background events obtained by the same Monte Carlo simulation is discussed.

4.3.1 Study of $K_{\pi 2}$ decay

In this analysis, we examined the accuracy of our Monte Carlo simulation by comparing the experimental spectrum with the spectrum obtained by the simulation in $K_{\pi 2}$ decay mode. The $K_{\pi 2}$ decay mode is a two-body decay which is well known and any uncertain parameter does not exist. Therefore, in the comparison of the spectrum of the real experiment with the spectrum obtained by Monte Carlo simulation, we were able to examine the accuracy of the data generated by Monte Carlo simulation.

The total energy of $\pi^0(E_{\gamma\gamma})$ in $K_{\pi 2}$ decay is shown in Fig.4.23. The energy spectrum of a photon(E1) with lower energy from π_0 decay is shown in Fig.4.24. The energy
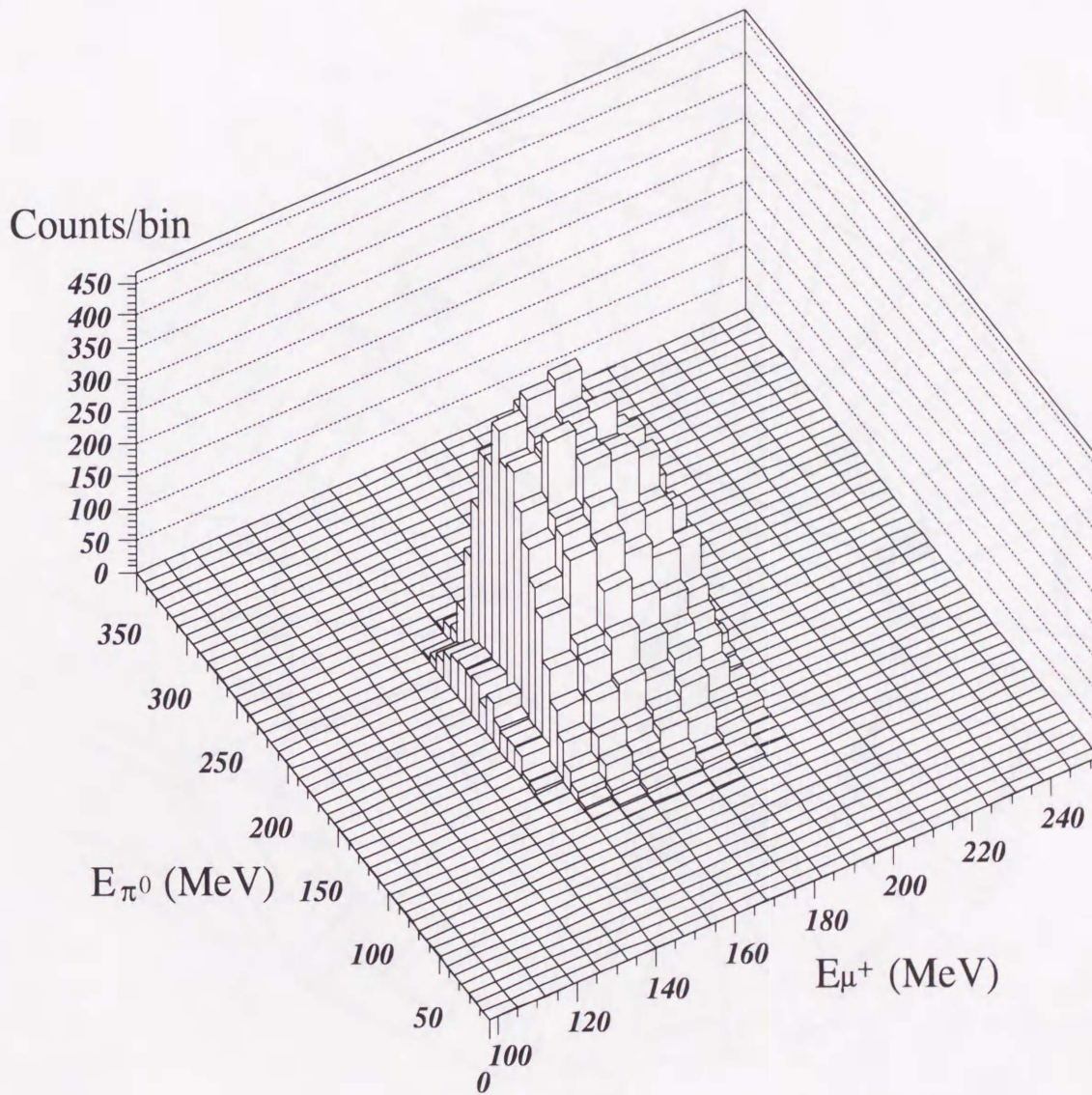
Figure 4.21: The Dalitz plot of $K_{\mu 3}$ event made by using the energies of μ^+ and π^0
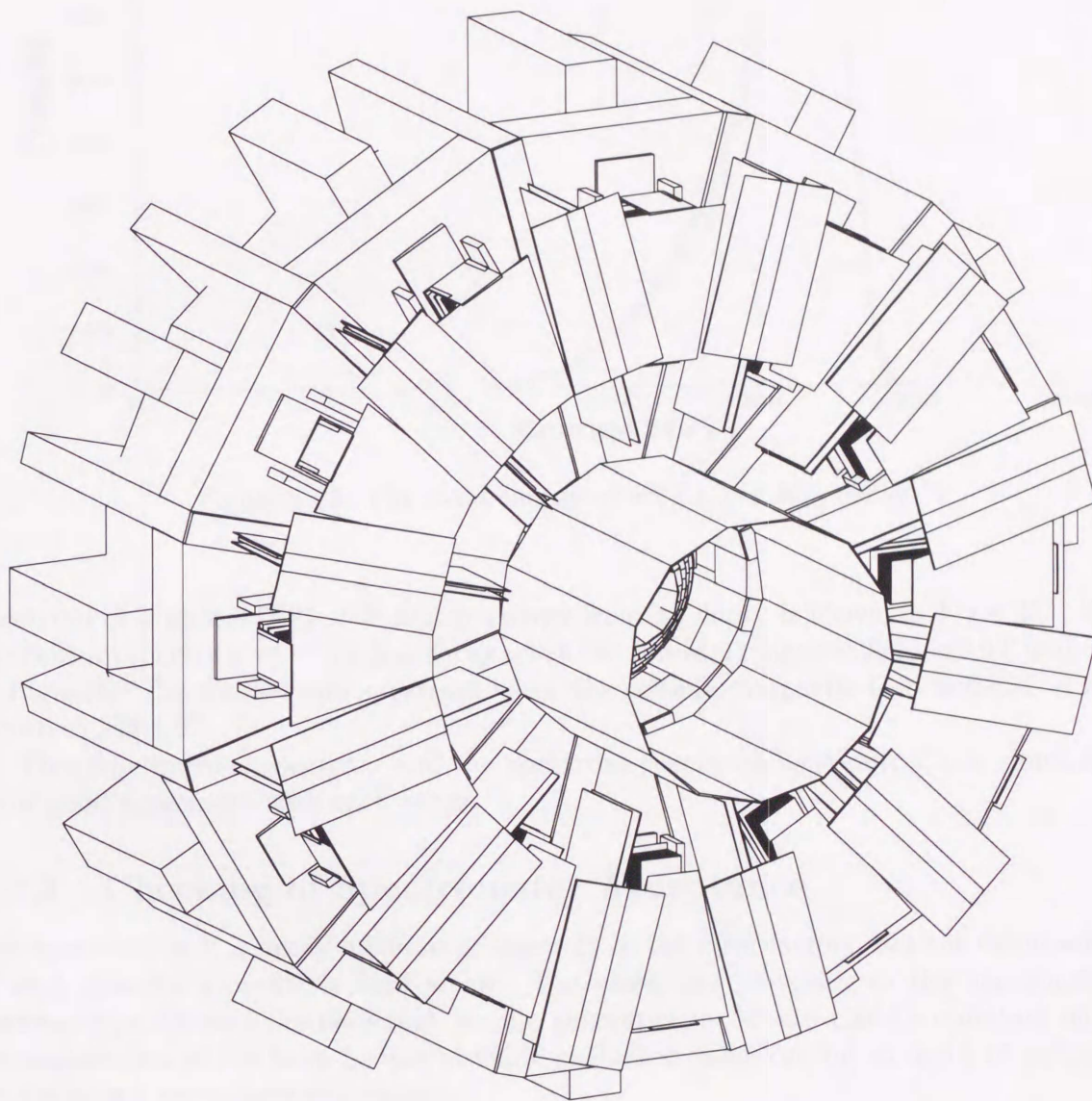
Figure 4.22: Detector components included in the Monte Carlo simulation program
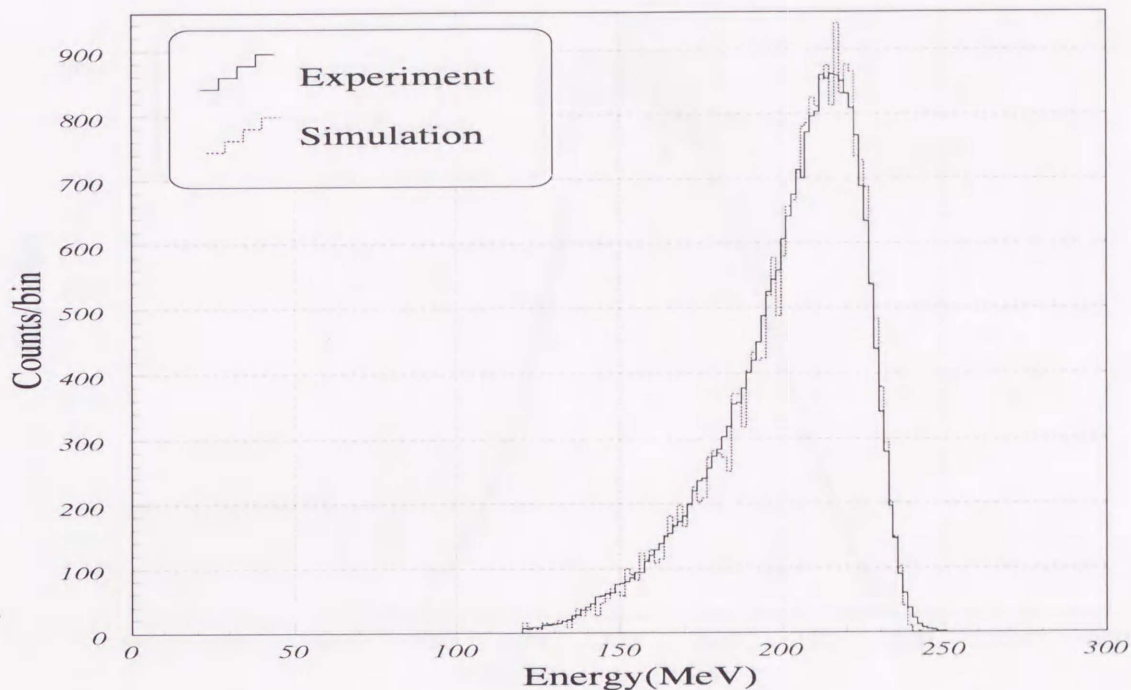
Figure 4.23: The total energy of $\pi^0(E_{\gamma\gamma})$ in $K_{\pi 2}$ decay

spectrum of a photon(E2) with higher energy from π_0 decay is shown in Fig.4.25. The momentum spectrum of π^+ in $K_{\pi 2}$ decay when the toroidal magnetic field is 0.9T is shown in Fig.4.26. The momentum spectrum when the toroidal magnetic field is 0.65T is also shown in Fig.4.27.

The experimental spectrum and the spectrum generated by Monte Carlo simulation show good agreement with each other.

4.3.2 Checking of Spectrometer Acceptance

The spectrum in $K_{\mu 3}$ decay mode itself depends on the form factors, but the deformation of each detector's profile is kept small. Therefore, the matching of the experimental detector's profile and the detector's profile generated by Monte Carlo simulation under the assumption of the form factors of world-evaluated value can be an index of accuracy for detector's acceptance estimation.

The particle hit position profiles of C2 in z direction, of C3 in r direction and of C4 in r direction under the toroidal magnetic field of 0.9T are shown in Fig.4.28, Fig.4.29 and Fig.4.30,respectively.

The particle hit position profiles of C2 in z direction, of C3 in r direction and of C4 in r direction under the toroidal magnetic field of 0.65T are shown in Fig.4.31, Fig.4.32 and Fig.4.33,respectively.

The opening angle spectrum between μ^+ and π^0 under the toroidal magnetic field of 0.9T is shown in Fig.4.34 and the one under the toroidal magnetic field of 0.65T in
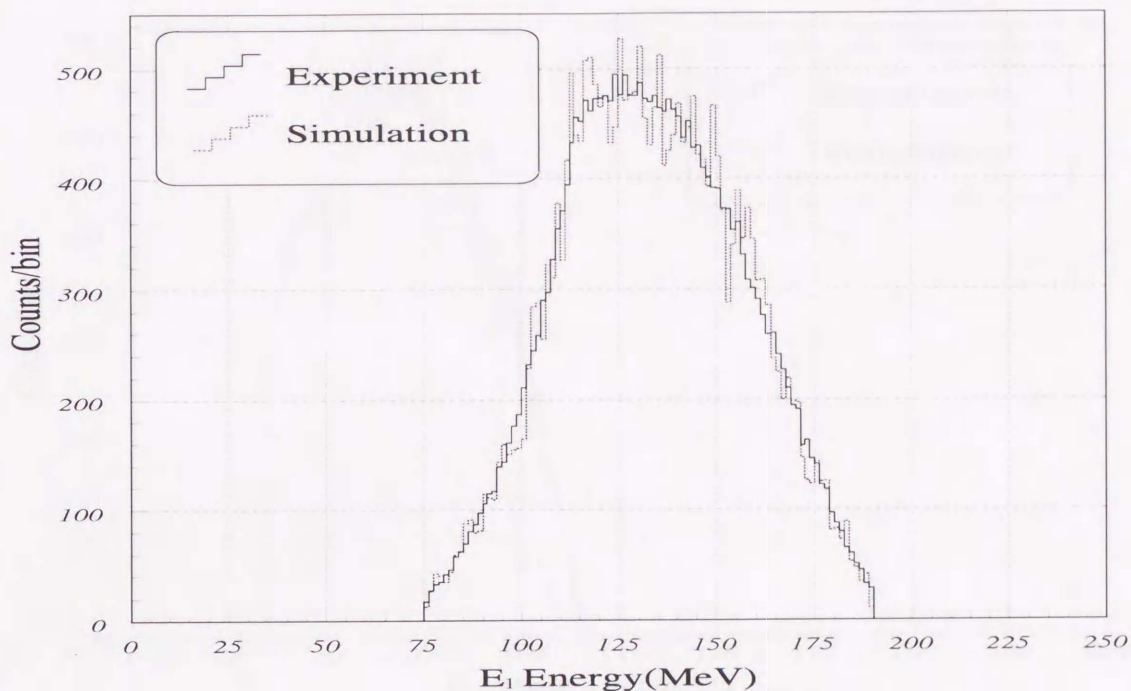
Figure 4.24: The energy spectrum of a photon with lower energy from π_0 decay in $K_{\pi 2}$ decay

Fig.4.35.

Both the experimental spectrum and the spectrum generated by Monte Carlo simulation show a fairly good agreement with each other.

4.3.3 Background Estimation

The purity of event samples is not perfect. Some amounts of background events leak into a set of the good $K_{\mu 3}$ events by being passed through the event-selection cuts. The leakage of background events would deform the Dalitz plot spectrum to some extent. This could be one of the sources of systematic error. But, this error can be corrected under the precise estimation of backgrounds.

The major sources of backgrounds are as follows.

- $K_{\pi 2}$ decay

- K_{e3} decay

- accidental hits of beam particles

The main background source is the miss-identification of the $K_{\pi 2}$ decay mode. π^+ from $K_{\pi 2}$ decay will decay into μ^+ and ν with 99.99% branching ratio and $2.60 \times 10^{-8} sec$ life time. If π^+ decays in this mode in front of the spectrometer, our detectors can not
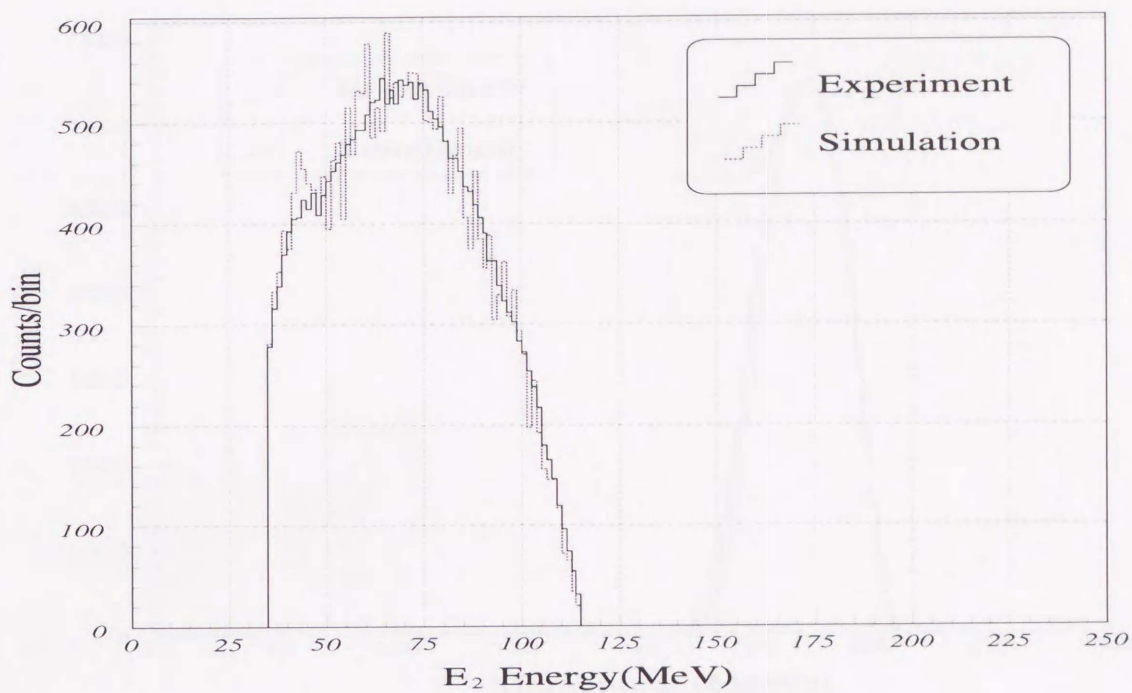
Figure 4.25: The energy spectrum of a photon with higher energy from π_0 decay in $K_{\pi 2}$ decay
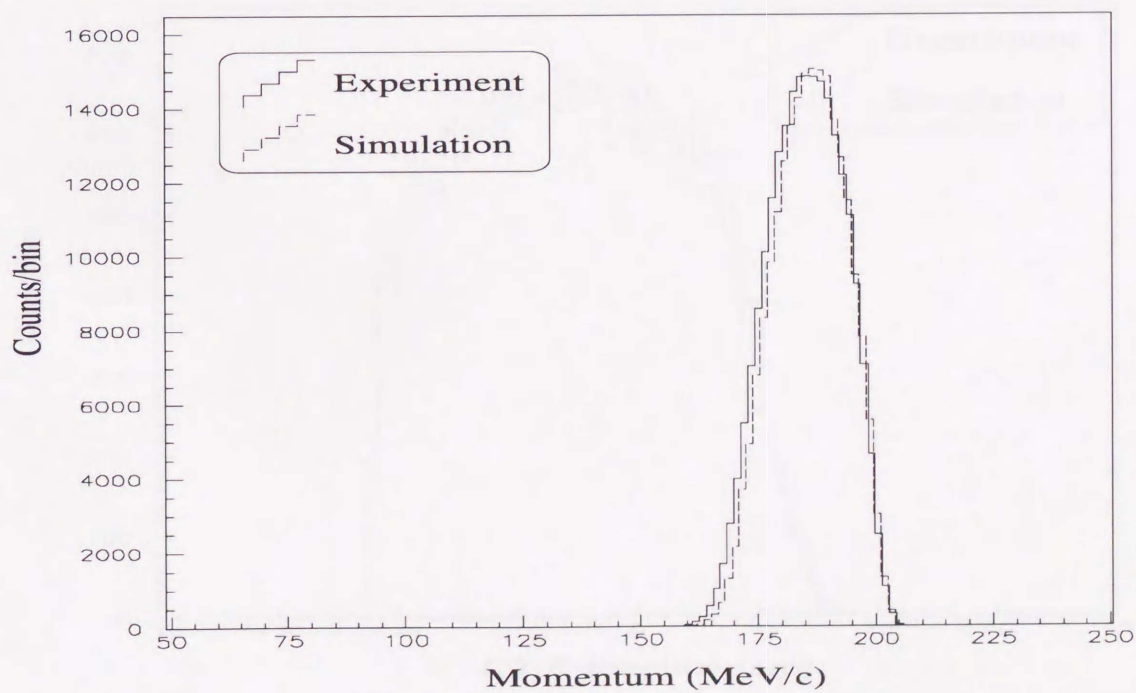
Figure 4.26: The π^+ momentum in $K_{\pi 2}$ decay (0.9T)
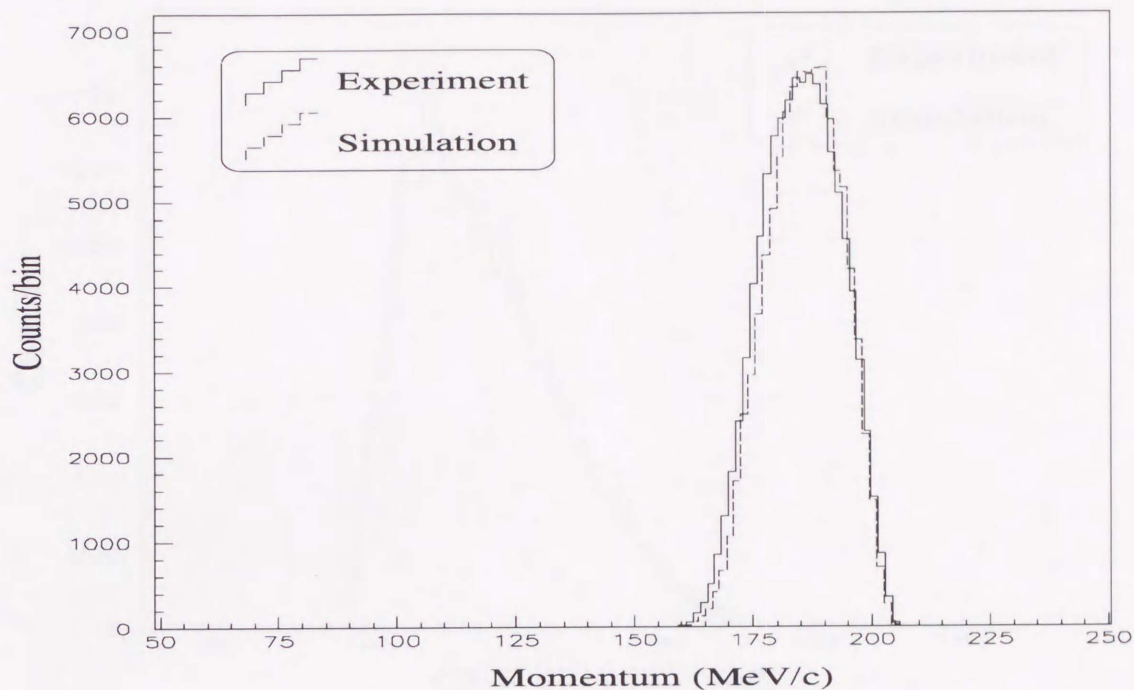
Figure 4.27: The π^+ momentum in $K_{\pi 2}$ decay (0.65T)
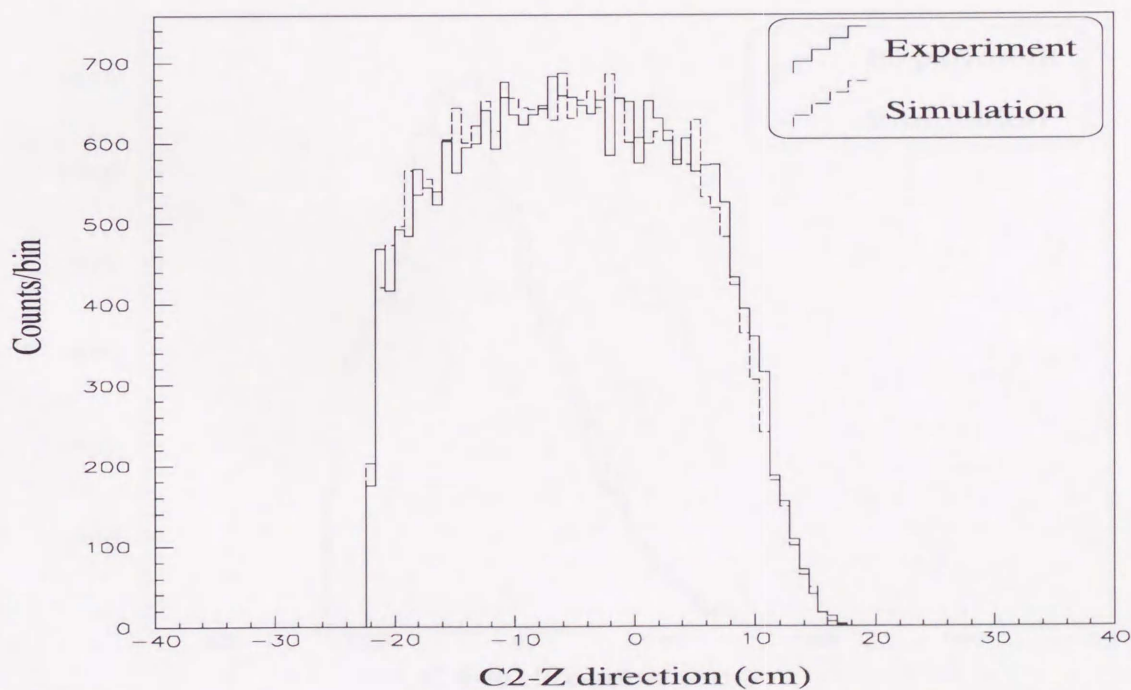
Figure 4.28: The profile of C2 in z direction(0.9T)
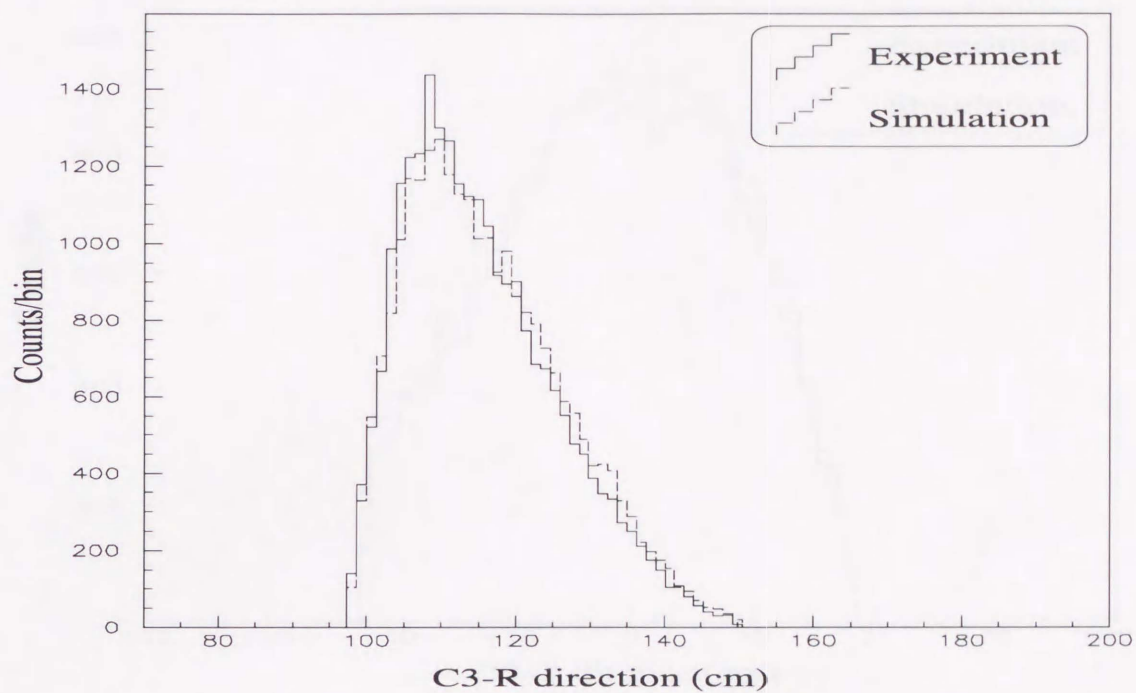
Figure 4.29: The profile of C3 in r direction(0.9T)
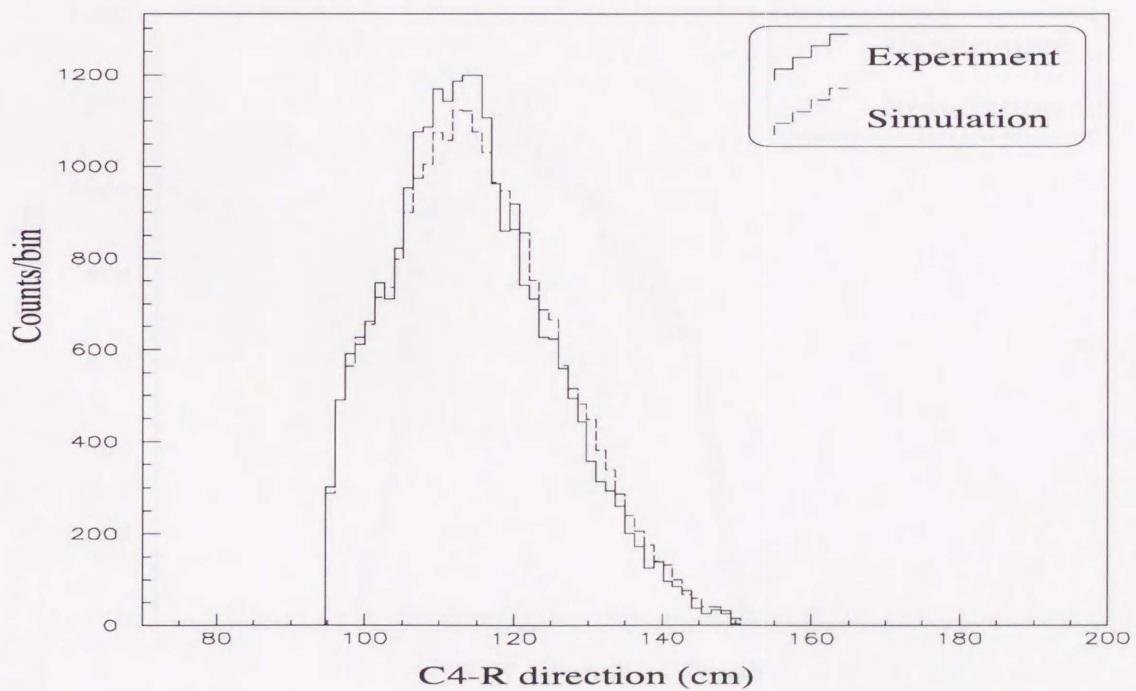
Figure 4.30: The profile of C4 in r direction(0.9T)
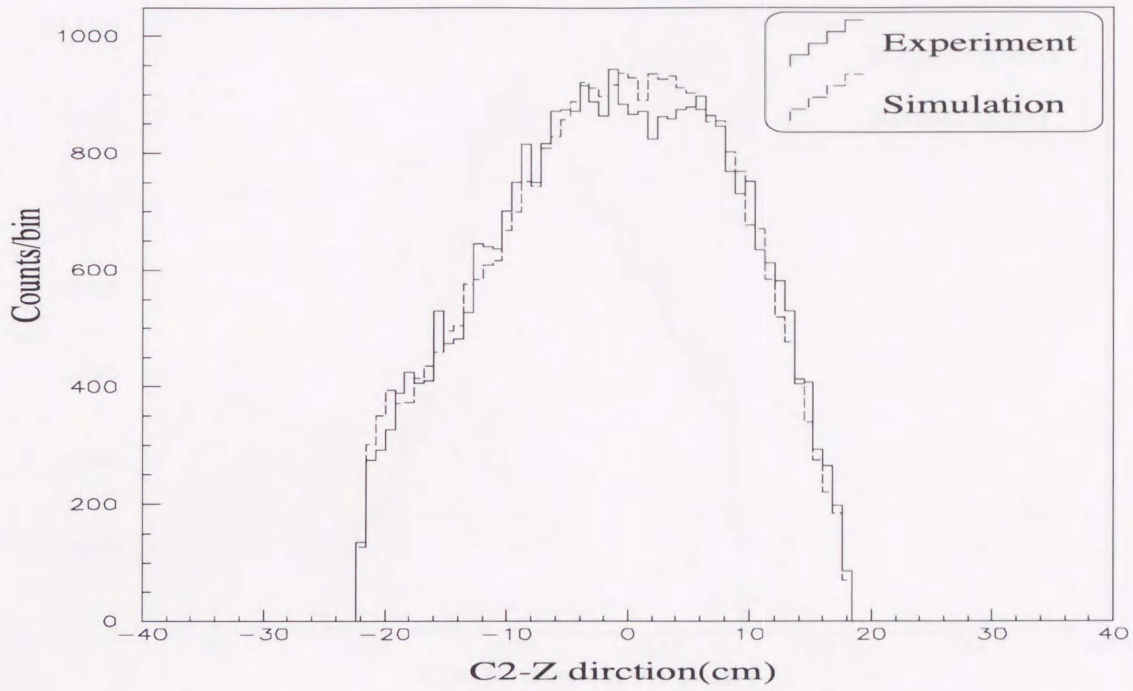
Figure 4.31: The profile of C2 in z direction(0.65T)
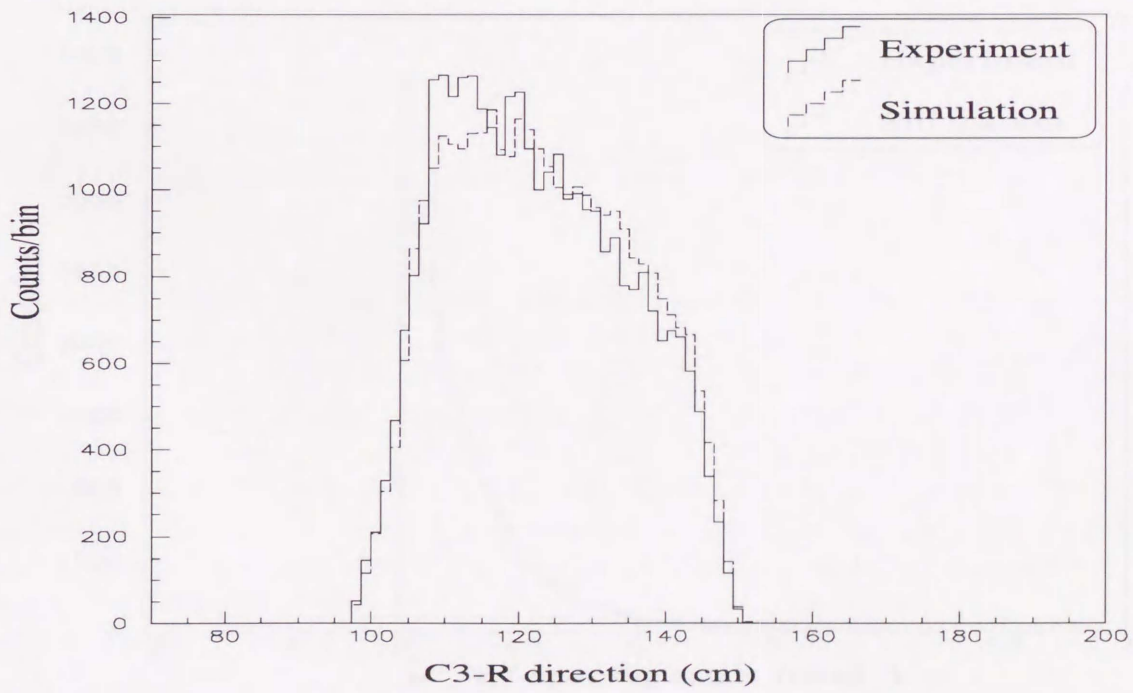
Figure 4.32: The profile of C3 in r direction(0.65T)
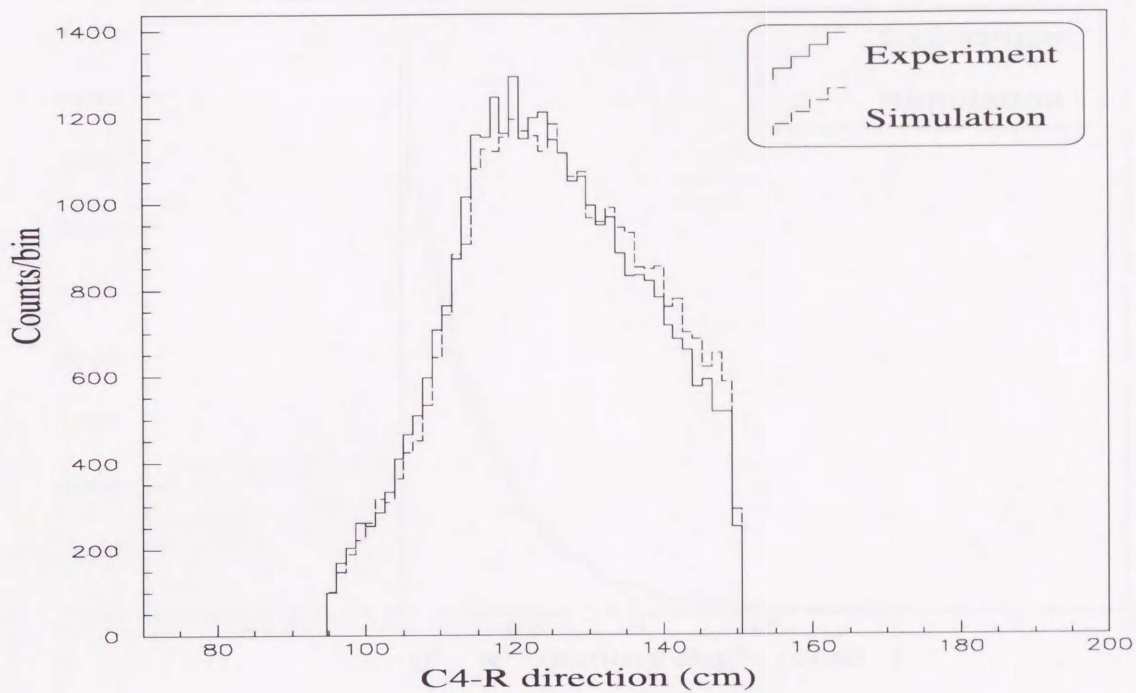
Figure 4.33: The profile of C4 in r direction(0.65T)
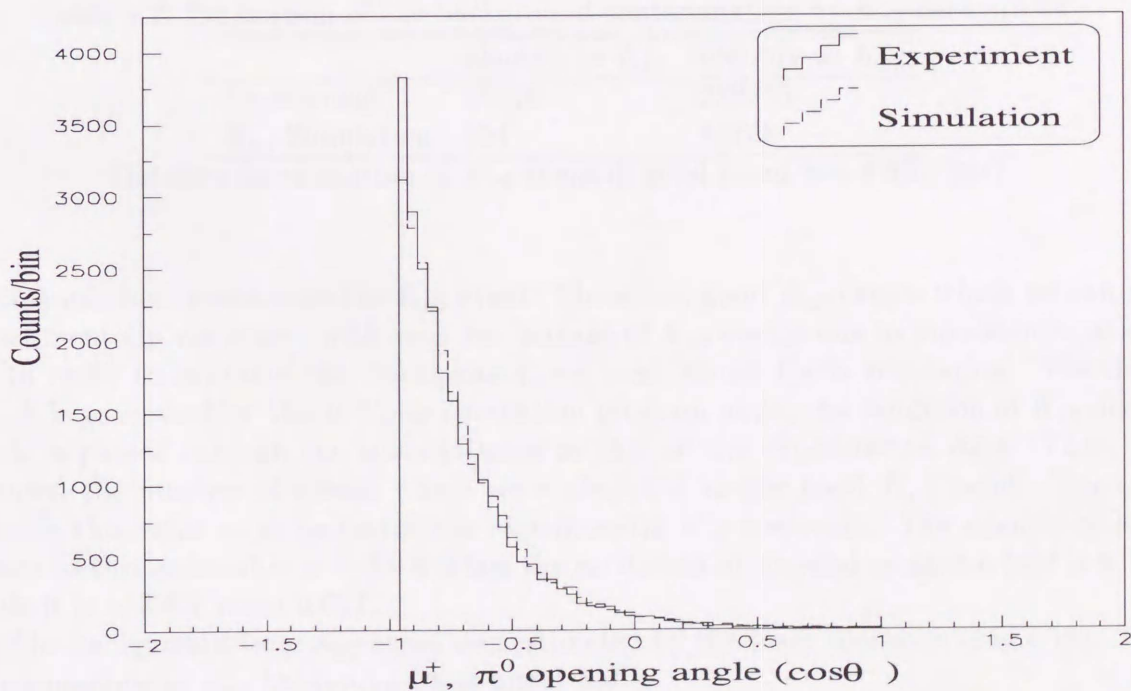
Figure 4.34: The opening angle spectrum between μ^+ and π^0
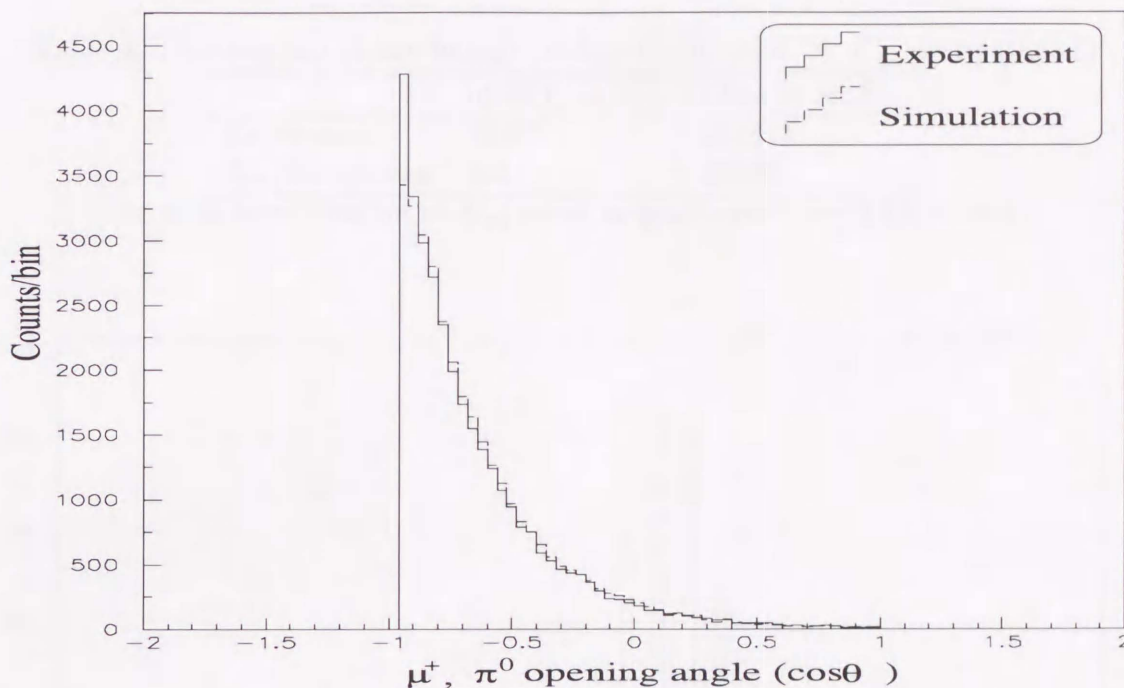
Figure 4.35: The opening angle spectrum between μ^+ and π^0

Table 4.2: Estimation of the background contamination by $K_{\pi2}$ decay (0.9T)

	identify as $K_{\mu3}$	identify as $K_{\pi2}$
Experiment	21716	228355
$K_{\pi2}$ Simulation	154	44768

The miss identification of $K_{\pi2}$ event in good event $=\sim 3.6\%$ (0.9T)

distinguish such event from the $K_{\mu3}$ event. Therefore, good $K_{\mu3}$ events which we can get experimentally, are mixed with such few leakage of $K_{\pi2}$ events due to miss-identification.

In order to estimate this background, we used Monte Carlo simulation. The data which is generated by Monte Carlo simulation program under the condition of $K_{\pi2}$ decay mode is passed through the analysis same as that of the experimental data. Then, we counted the number of events which were identified as the good $K_{\mu3}$ event. Then,we re-scale this value so as to match the experimental $K_{\pi2}$ spectrum. The amount of leak events in this estimation is $\sim 3.6\%$ when the excitation of toroidal magnetic field is 0.9T, while it is $\sim 3.6\%$ when 0.65T.

The background from K_{e3} event was estimated by the mass spectrum (Fig.4.18). The contamination of K_{e3} background was under 0.3%.

Table 4.3: Estimation of the background contamination by $K_{\pi 2}$ decay (0.65T)

	identify as $K_{\mu 3}$	identify as $K_{\pi 2}$
Experiment	22595	101418
$K_{\pi 2}$ Simulation	281	38556

The miss identification of $K_{\pi 2}$ event in good event $=\sim 3.3\%$ (0.65T)
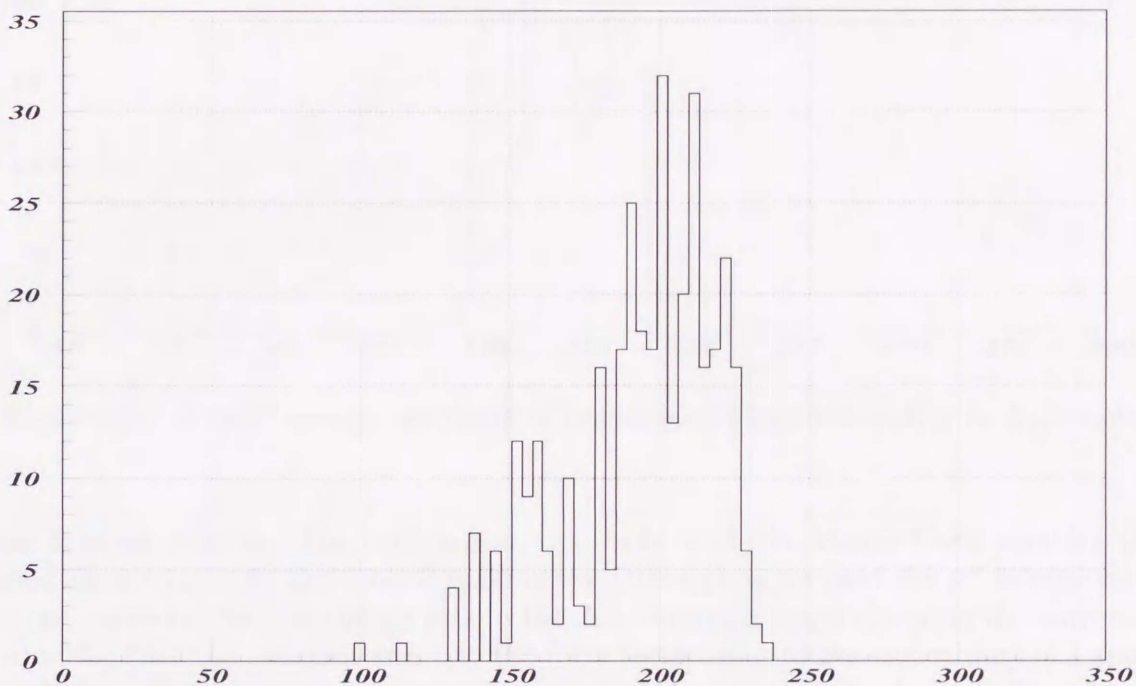
Figure 4.36: The π^0 energy spectrum of events miss-identified as $K_{\mu 3}$ in $K_{\pi 2}$ event

4.3.4   Background subtraction

The background which was understood to some extent can be estimated and subtracted by using Monte Carlo simulation. The contamination of the main background mode $K_{\pi 2}$ was estimated in the previous section. The spectra of the miss identified $K_{\pi 2}$ events are shown in Fig.4.36 and Fig.4.37. The effect of deformation on the experimental Dalitz plot caused by miss-identified $K_{\pi 2}$ events was removed by subtracting the background spectrum from the experimental spectrum.

4.4   Fitting Method

In order to obtain the values of $K_{\mu 3}$ form factors, we compared the Dalitz plot which was made experimentally by measured energies of π^0 and μ^+ with that generated by Monte Carlo simulation. The Monte Carlo simulation data were processed under the
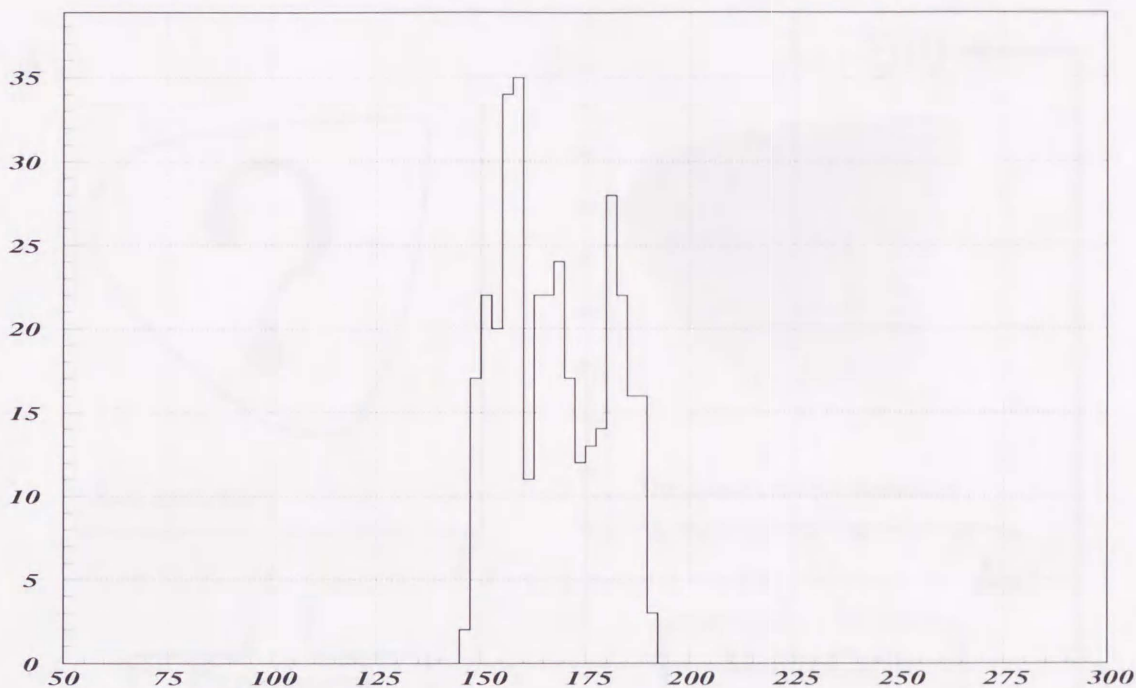
Figure 4.37: The π^+ energy spectrum of events miss-identified as $K_{\mu3}$ in $K_{\pi2}$ event

same analysis criteria. The comparison was made with the Monte Carlo samples that passed all the cuts. At the time of making the Dalitz plot, we used the μ^+ energy which was not corrected for the energy loss in the K^+ stopping target, because the correction would introduce the spurious effect to the form factors due to the uncertainty of Landau fluctuation. This comparison is an alternative to the comparison of the Dalitz plots at birth. Because the Monte Carlo simulation reproduces the experimental acceptance and response properly,the transformation from the Dalitz plot at birth condition to the one on the measured condition, i.e. the deformation of the Dalitz plot,is same in the experiment and in the Monte Carlo simulation.

The form factors were obtained by searching for the point of minimum value of χ^2. χ^2 was defined as,

$$\chi^2 = \sum_i^n \frac{(N_{Exp,i} - cN_{MC,i})^2}{\sigma_{Exp,i}^2 + (c\sigma_{MC,i})^2} \tag{4.12}$$

where n is the number of bins in the Dalitz plot histogram and c is introduced to normalize the calculated events to the measured one. $N_{Exp,i}$ and $N_{MC,i}$ are the number of counts in the i-th bins in the experiment and the Monte Carlo simulation, respectively. $\sigma_{Exp,i}$ and $\sigma_{MC,i}$ are the weight factor due to the statistical error in each bin. For the determination of statistical error mainly from the statistics of experimental data ,the total count of the Monte Carlo simulation data in each bin was chosen to be about four times larger than those of the experimental one.

The schematic diagram of the fitting procedure is shown in Fig.4.38. The fitting
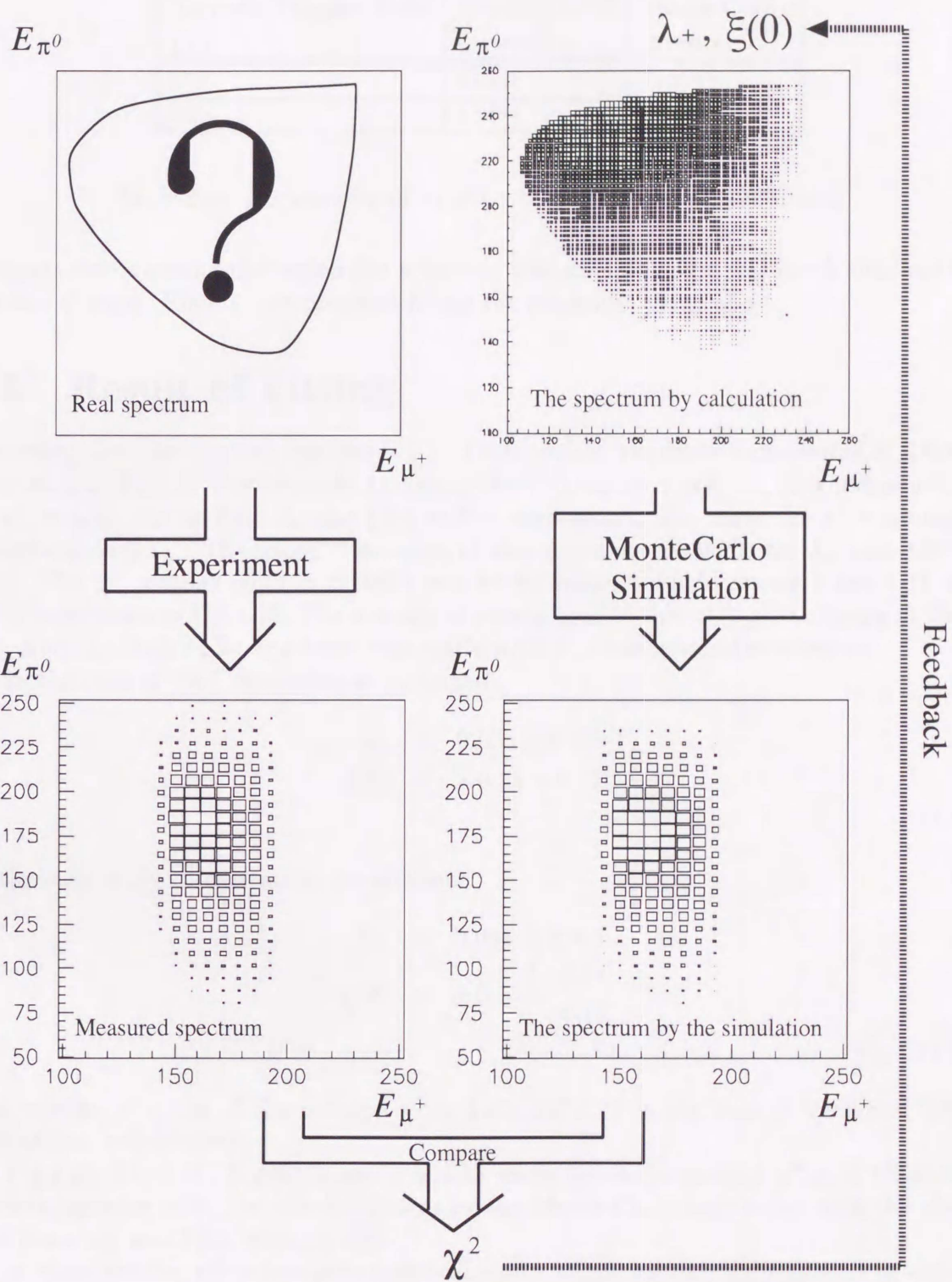
Figure 4.38: The schematic diagram of the fitting procedure. By varying the parameters in the form factors, we can reconstruct the measured Dalitz plot. The optimum values were obtained by searching for the minimum value of the χ^2.

Toroidal Magnet Field (T)	Experimental (events)	Monte Carlo (events)
0.9	21558	173913
0.65	18484	134324

Table 4.4: The number of events which were used in the fitting

program was scanning the region like a lattice. The scanning step was much smaller than statistical error. Finally, the program found the minimum value of χ^2.

4.5   Result of Fitting

Assuming that the weak interaction is $V - A$ interaction, the matrix element of $K_{\mu 3}$ decay is written as Eq.1.2. Furthermore assuming the T-invariance and the f_-'s independence on q^2, we can choose only λ_+ and $\xi(0)$ as free parameters. We made the χ^2 scanning in 2-dimensional $(\lambda_+, \xi(0))$ space. The steps of this scanning are 0.001 for λ_+ and 0.01 for $\xi(0)$. The χ^2 contour plots in which the toroidal magnetic field strength are 0.9T and 0.65T are shown in Fig.4.39. The number of events used in this fitting was shown in Table 4.4. And the Dalitz plot spectrum was made with $K_{\pi 2}$ background subtraction.

In the case of 0.9T excitation, we obtained.

$$\lambda_+ = 0.033 \pm 0.009$$
$$\xi(0) = -0.38 \pm 0.11$$

$$(4.13)$$

In the case of 0.65T excitation, we obtained

$$\lambda_+ = 0.035 \pm 0.011$$
$$\xi(0) = -0.43 \begin{cases} +0.14 \\ -0.12 \end{cases}$$

$$(4.14)$$

The minimum values of the reduced χ^2 is 1.65 and 1.37 in the case of 0.9T and 0.65T excitations, respectively.

Fig.4.40, Fig.4.41, Fig.4.42, and Fig.4.43 show the experimental μ^+ and π^0 energy spectra together with the calculated ones by the Monte Carlo simulation with the above best fitted λ_+ and $\xi(0)$, respectively.

In these results, the errors are statistical errors which include the statistics of experimental data and the Monte Carlo simulation data. The discussion and estimation of the systematic error will be described in the next section.
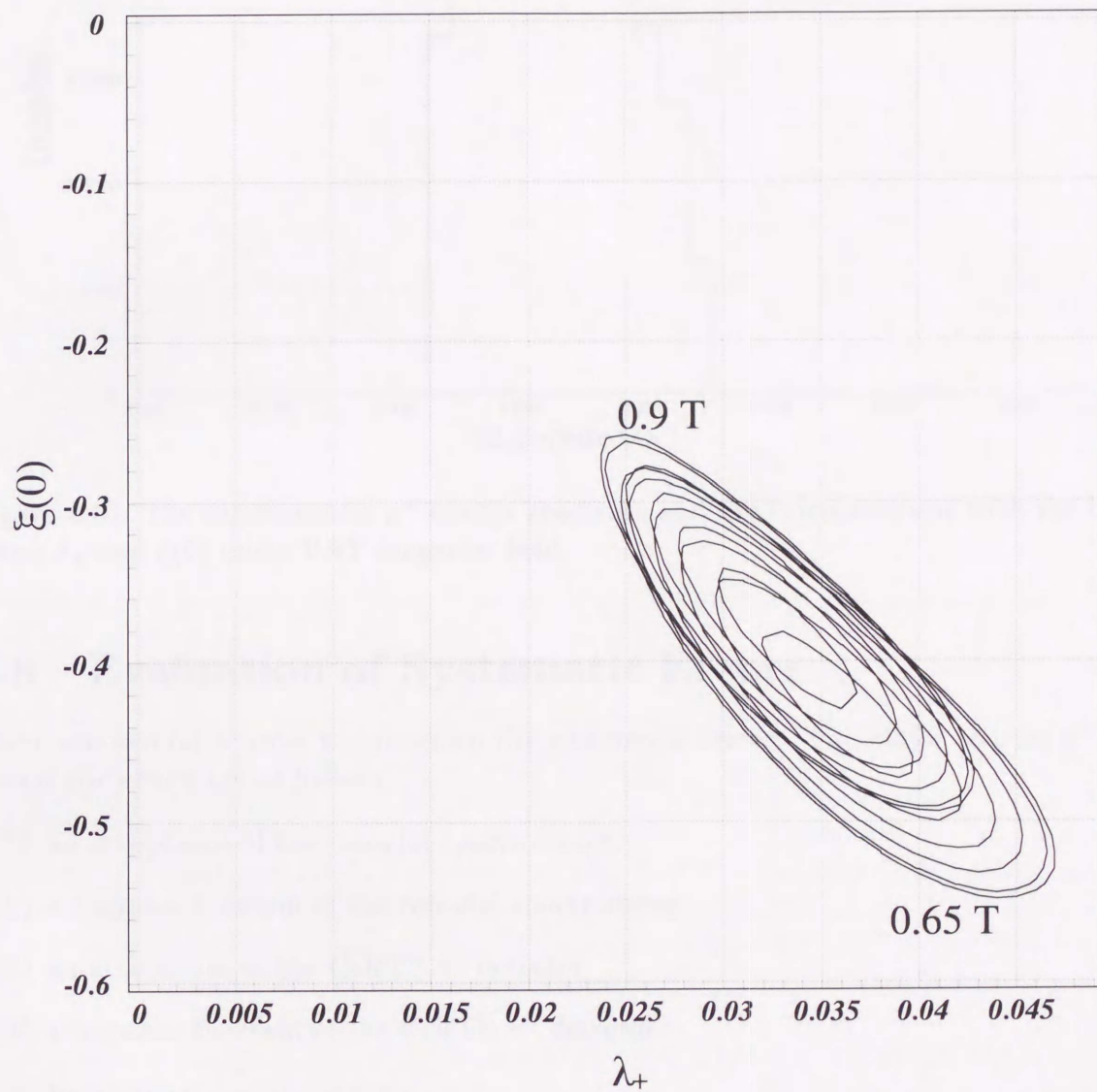
Figure 4.39: The χ^2 contour plot (0.9T, 0.65T) The x-axis is λ_+. The y-axis is $\xi(0)$. The inside of outermost circle is one σ region. The contours are drawn by 0.2 step in χ^2 value.
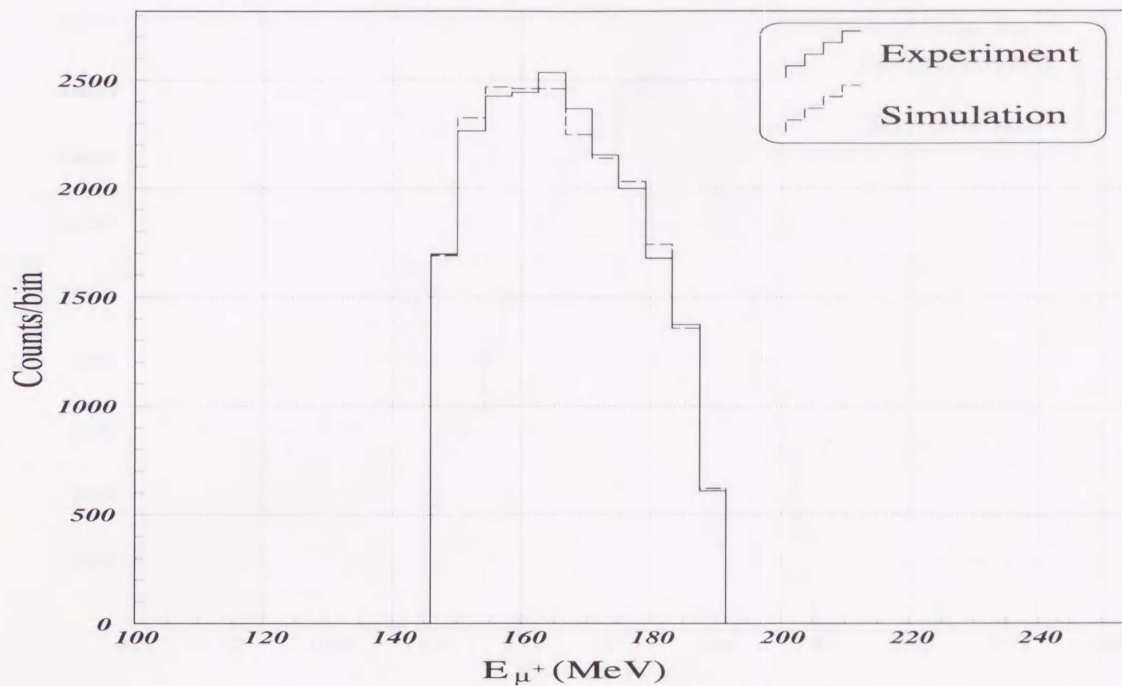
Figure 4.40: The experimental μ^+ energy spectrum and the calculated one with the best fitted λ_+ and $\xi(0)$ under 0.9T magnetic field.

4.6   Evaluation of Systematic Errors

There are several sources to introduce the systematic errors. The major sources of the systematic errors are as follows.

(1) an acceptance of the toroidal spectrometer

(2) a response function of the toroidal spectrometer

(3) an acceptance of the CsI(Tl) π^0 detector

(4) a response function of the CsI(Tl) π^0 detector

(5) background contaminations

(6) a stopped K^+ profile in the K^+ stopping target

(7) error in estimation of the energy loss in the active target

(8) photon conversion in the target

In these, (3) and (5) have a large influence to the form factors. Especially, the $K_{\pi2}$ event contamination and the gain of CsI(Tl) π^0 detector are important.
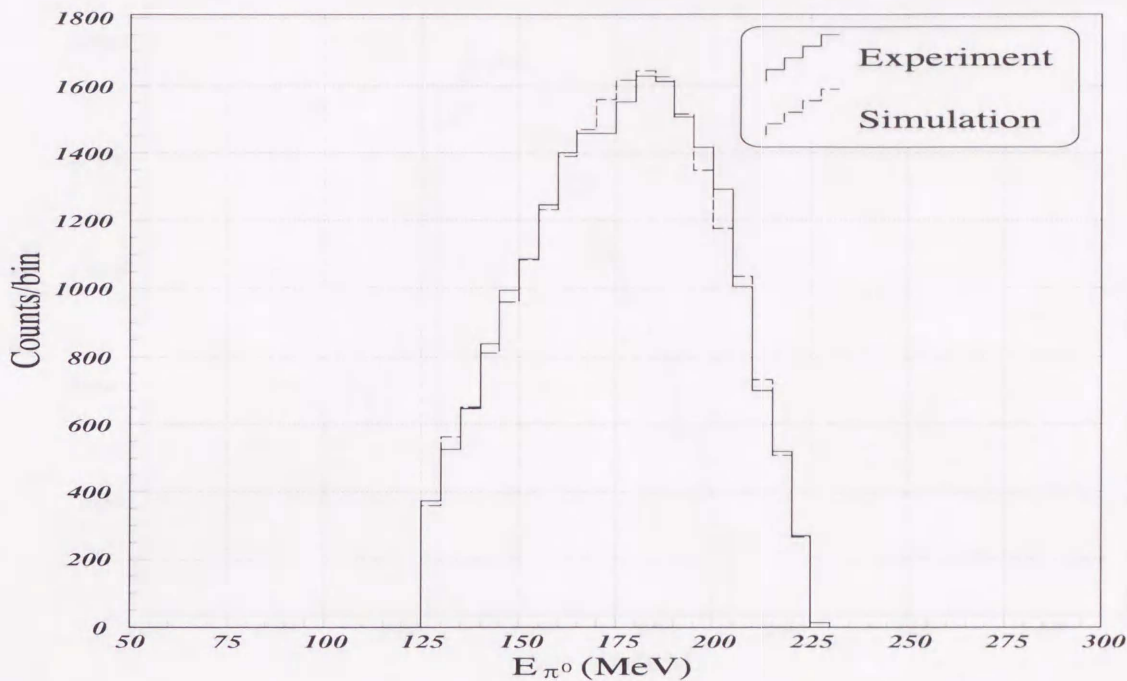
Figure 4.41: The experimental π^0 energy spectrum and the calculated one with the best fitted λ_+ and $\xi(0)$ under 0.9T magnetic field.

The behavior of the contamination from π^+ decay in flight in $K_{\pi 2}$ decay mode

The largest source of the systematic errors is from the background contamination, especially the back ground from $K_{\pi 2}$ decay mode. The behavior of the form factors under the contamination of $K_{\pi 2}$ event can be estimated by the Monte Carlo simulation study.

Fig.4.44 shows the behavior of the fitted results under the various contamination of $K_{\pi 2}$ events. The figure shows a χ^2 contours obtained by the same fitting procedure for different samples with backgrounds. The circle marked "0% BG" is the fitted result with no contamination of $K_{\pi 2}$ decay events. The circle marked "2% BG" is the fitted result with 2% of contamination of $K_{\pi 2}$ decay events. The circle marked "5% BG" is the fitted result with 5% of contamination of $K_{\pi 2}$ decay events.

The contamination of $K_{\pi 2}$ event is 3.6%(0.9T) or 3.3%(0.65T) by Monte Carlo simulation study. And then, this background was subtracted with background energy spectrum shape. The statistical ambiguity of $K_{\pi 2}$ background spectrum was under 10%. Even if included other mode and ambiguity of estimation by Monte Carlo simulation, the total background contamination was under 2%. The effect on the form factor by the contamination of other modes was smaller than one of $K_{\pi 2}$ mode. Therefore the effect on the form factor parameters caused by the back ground contamination is less than 0.011 for λ_+ and less than 0.063 for $\xi(0)$ as one σ.
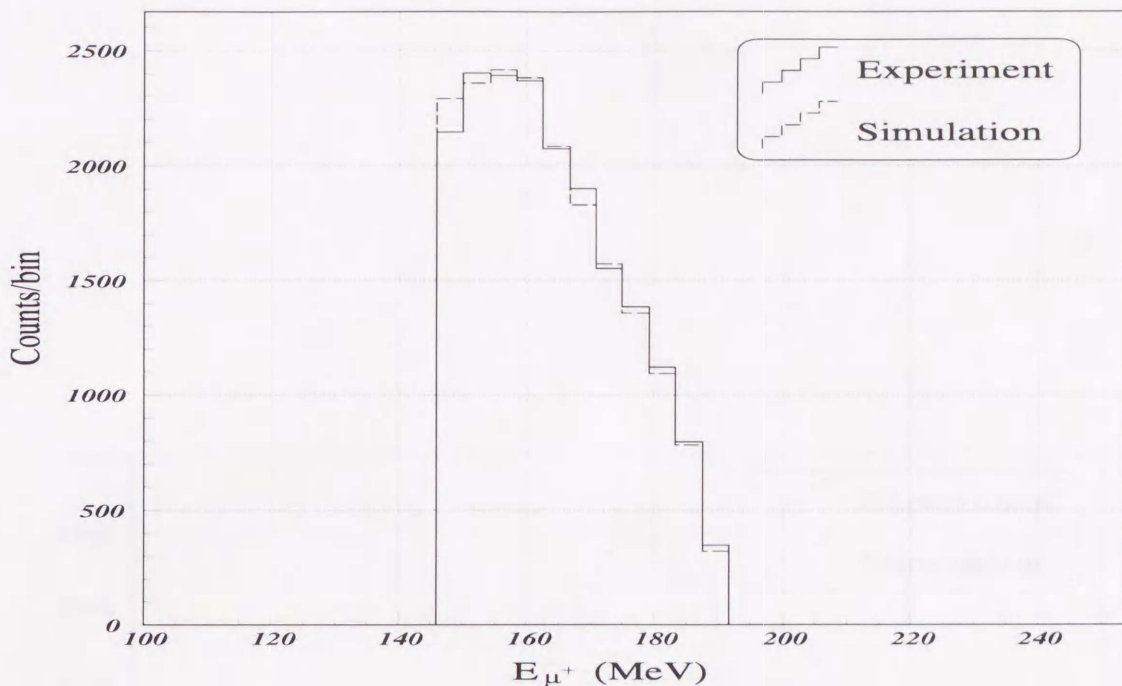
Figure 4.42: The experimental μ^+ energy spectrum and the calculated one with the best fitted λ_+ and $\xi(0)$ under 0.65T magnetic field.

The behavior of the gain drift of the photon detector

Another large source of systematic error is wrong energy calibration of the CsI(Tl) photon detector. The CsI(Tl) photon detector measures π^0 energy directly. Therefore, the wrong energy calibration of the photon detector deforms the Dalitz plot. To investigate influences on the form factors, we examined the fitting under the condition where the energy calibration of photon detector was changed artificially. The χ^2 plot of π^0 energy in $K_{\pi 2}$ mode for the experimental data is shown in Fig.4.45. The x-axis shows the energy calibration factor of the photon detector. Fig.4.46 shows the fitted results under the conditions where the energy calibration of the photon detector was changed as 0.995, 0.998, 1.00, 1.02, and 1.05 times the original value.

The calibration factor of photon detectors were matched within ± 0.001. Therefore, the estimation of the systematic error originated by the wrong calibration of photon detector is estimated as $\Delta\lambda_+ = \pm 0.004$ and $\Delta\xi(0) = \pm 0.02$. The gain correction factor 1.001 was used by the fitting.
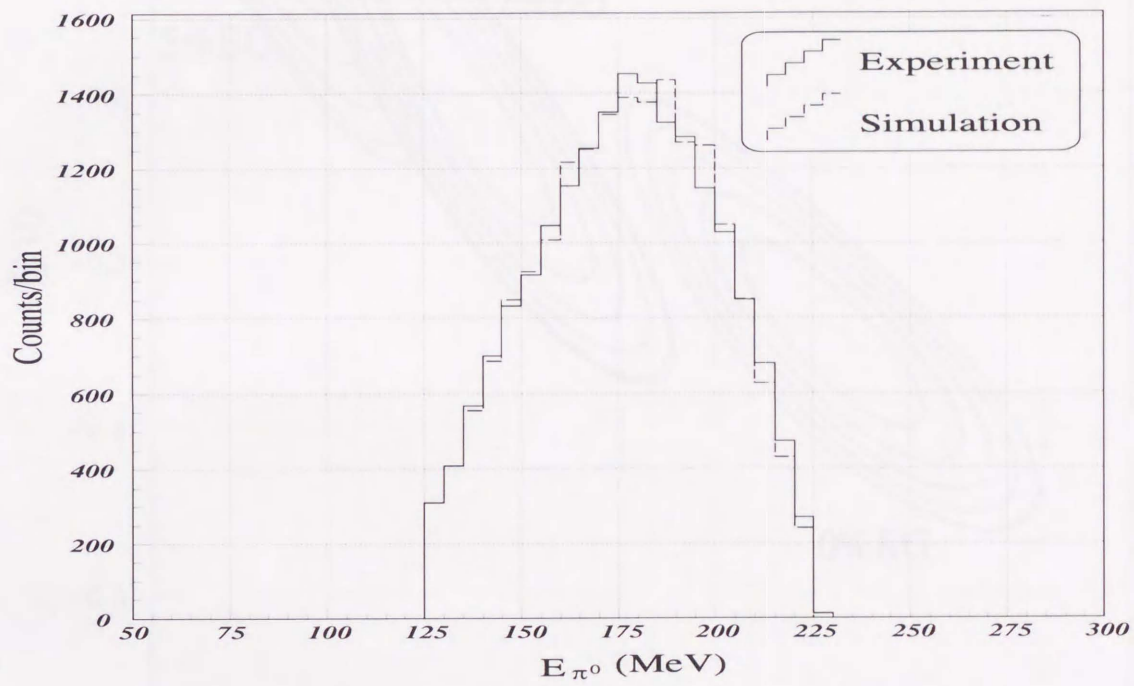
Figure 4.43: The experimental π^0 energy spectrum and the calculated one with the best fitted λ_+ and $\xi(0)$ under 0.65T magnetic field.
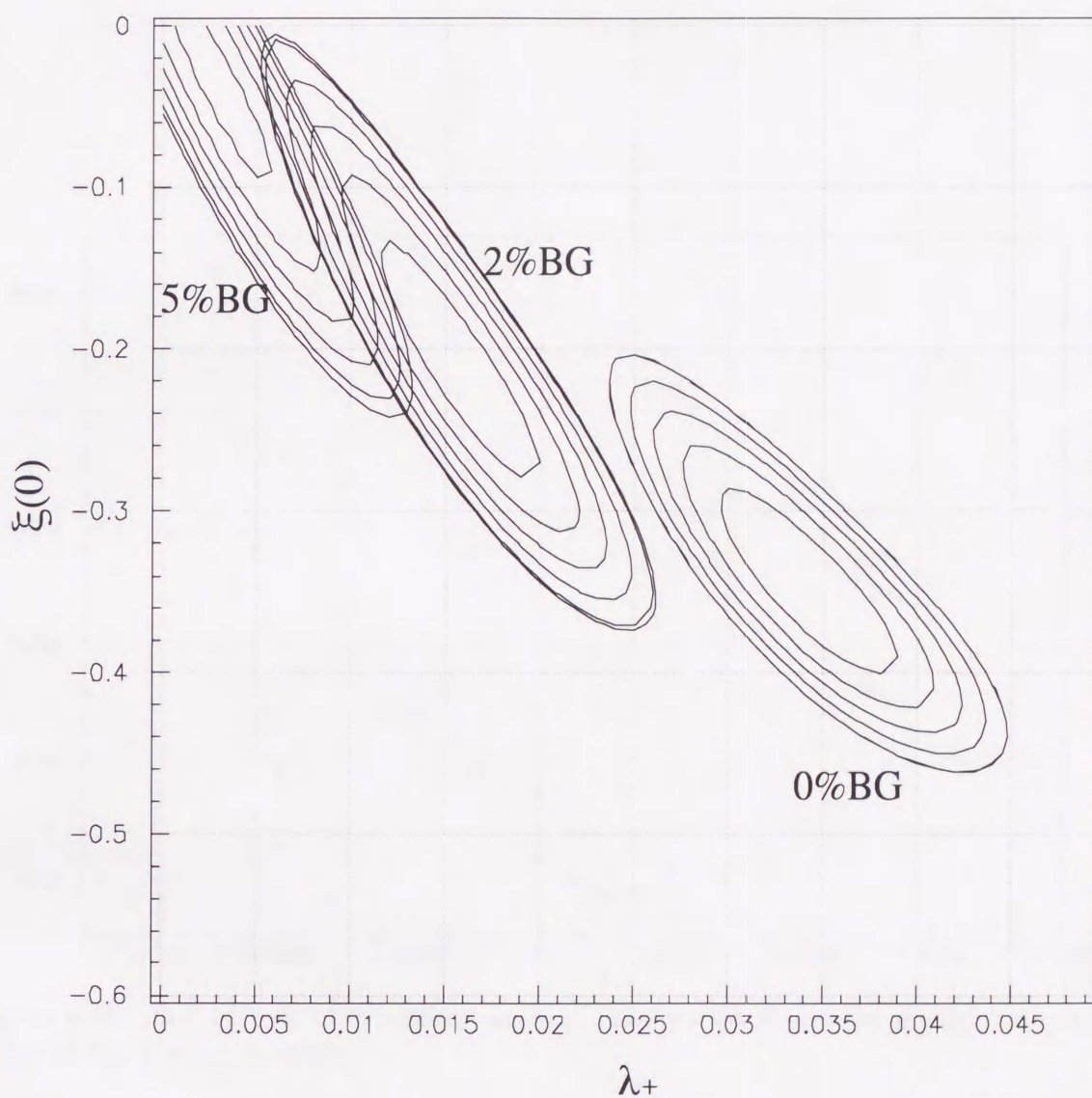
Figure 4.44: The behavior of χ^2 contour with the various contamination of $K_{\pi 2}$ events. The circle marked "0% BG" is $K_{\mu 3}$ M.C. data fitted by $K_{\mu 3}$ M.C. data. The circle marked "2% BG" is M.C. data mixed with 2% $K_{\pi 2}$ in $K_{\mu 3}$ fitted by $K_{\mu 3}$ M.C. data. The circle marked "5% BG" is M.C. data mixed with 5% $K_{\pi 2}$ in $K_{\mu 3}$ fitted by $K_{\mu 3}$ M.C. data.
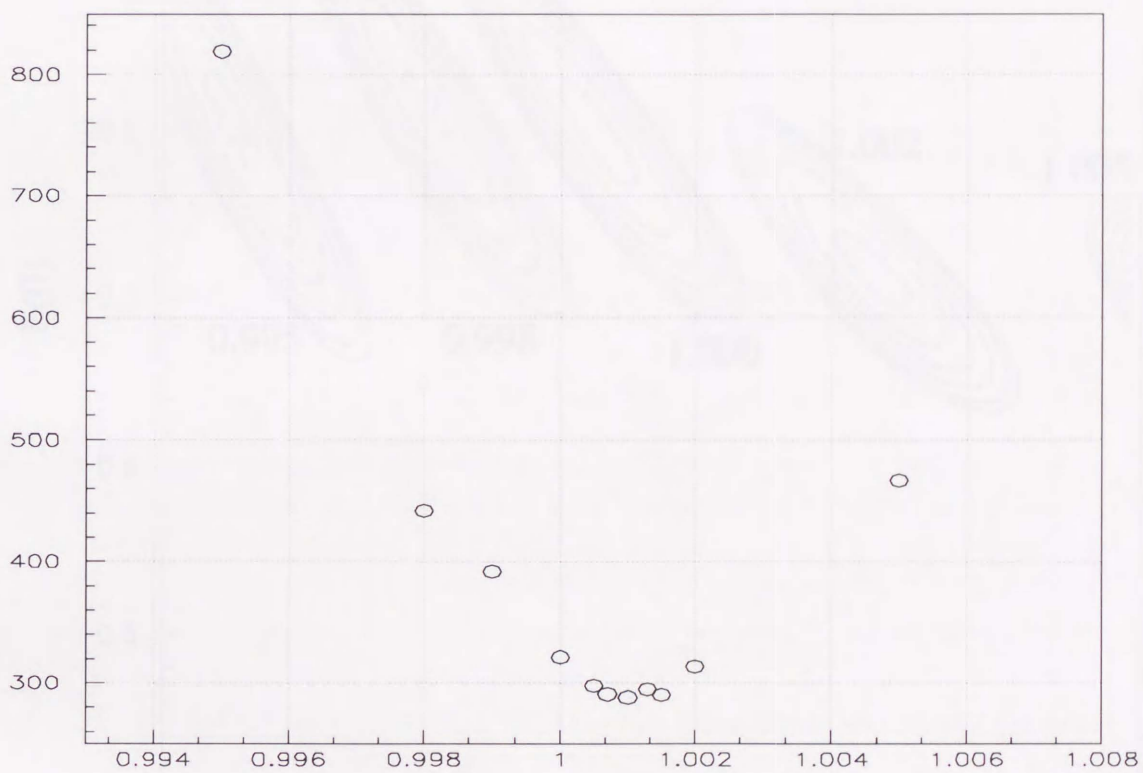
Figure 4.45: The χ^2 plot of π^0 energy in $K_{\pi 2}$. The x-axis shows the energy calibration factor of the photon detector.
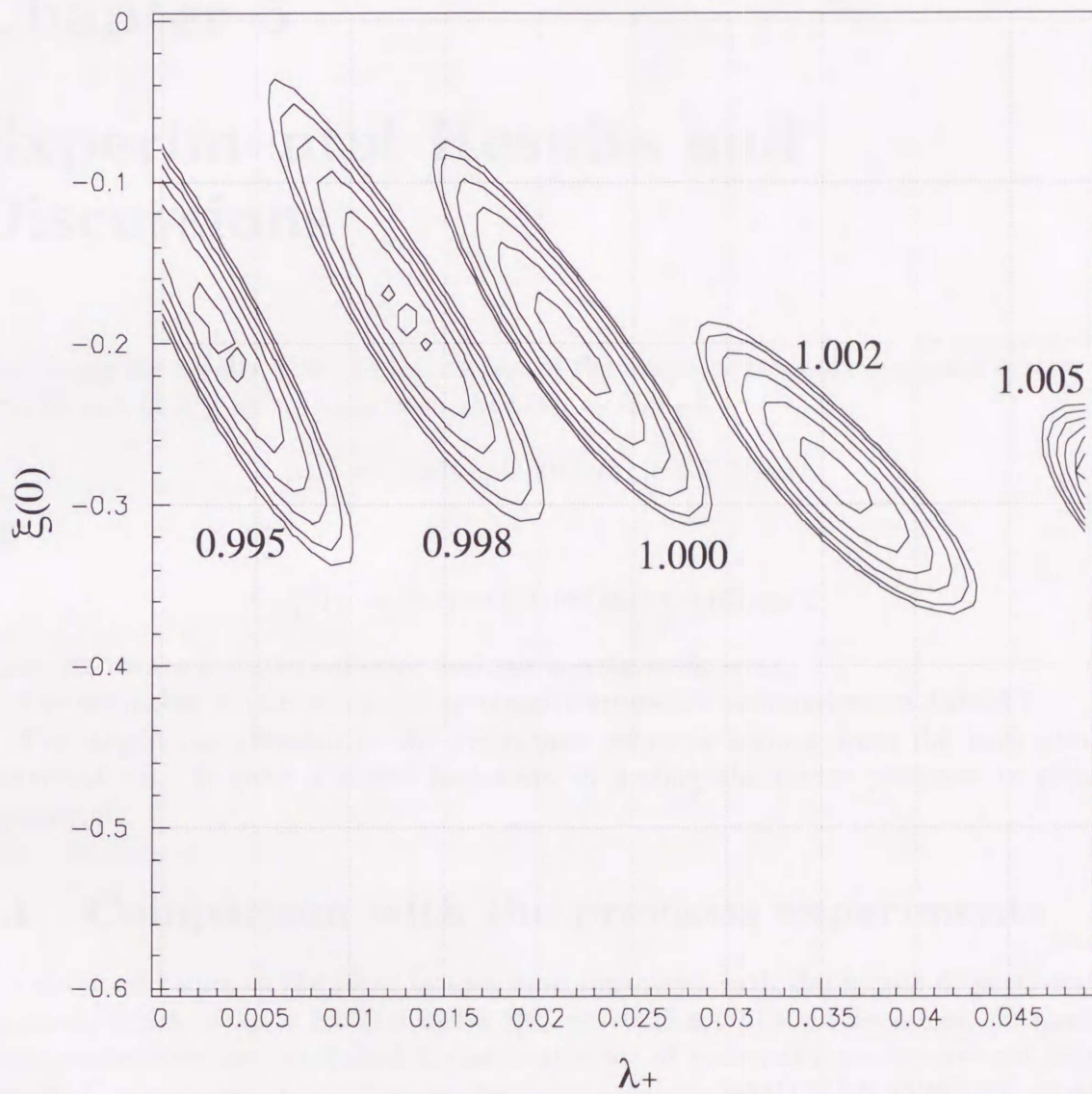
Figure 4.46: The influence induced by wrong energy calibration of the photon detector. The figure shows a χ^2 plot of the form factors fitting.

The gain of photon detector was changed artificially as 0.995, 0.998, 1.00, 1.02, and 1.05 times larger than the calibrated value.

Chapter 5

Experimental Results and Discussions

Combining the results with the estimation of the major sources of systematic errors, the form factors of $K_{\mu3}$ decay have been obtained as follows,

$$\lambda_+ = 0.034 \pm 0.007(sta) \pm 0.012(sys),$$

and

$$\xi(0) = -0.40 \pm 0.08(sta) \pm 0.07(sys),$$

where sta means a statistical error and sys a systematic error.

The estimated major sources of systematic errors are summarized in Table5.1.

The largest contribution to the systematic errors is coming from the back ground contamination. It gives a severe limitation in getting the better precision to present experiment.

5.1 Comparison with the previous experiments

The obtained values of the form factors were consistent with the results of previous experiments which is $\lambda_+ = 0.033 \pm 0.008, \xi(0) = -0.35 \pm 0.015$ within errors. In most of the experiments shown in Table5.2, the treatments of systematic errors were not clearly described. It is uncertain at all except for the experiment WHITMAN 80[Whi80] whether were included in the obtained results or not. As for the statistical error, this measurement

Table 5.1: The origin of the errors

Origin	$\Delta\lambda^+$	$\Delta\xi(0)$
Background contamination	± 0.012	± 0.06
Photon detector gain	± 0.004	± 0.02
Statistics of M.C. simulation	± 0.002	± 0.03

Table 5.2: The values of $K_{\mu 3}$ form factors me-sured by the previous experiments

λ^+	$\xi(0)$	Events	Document ID
0.034 ± 0.014	-0.40 ± 0.11	40042	Present experiment
0.050 ± 0.013	-0.27 ± 0.25	3973	WHITMAN 80 [Whi80]
0.025 ± 0.030	-0.8 ± 0.8	490	ARNOLD 74 [Arn74]
0.027 ± 0.019	-0.57 ± 0.24	6527	MERAN 74 [Mer74]
0.025 ± 0.017	-0.36 ± 0.40	1897	BRAUN 73 [Bra73]
0.024 ± 0.019	-0.62 ± 0.28	4025	ANKENBRANDT 72[Ank73]
-0.006 ± 0.015	$+0.45 \pm 0.28$	3480	CHIANG 72 [Chi72]
0.050 ± 0.018	-1.1 ± 0.56	3240	HAIDT 71 [Hai72]
0.0 ± 0.05	-0.72 ± 0.93	444	CALLAHAN 66 [Cal66]

has achieved a new progress in comparison with the previous experiments, the details of which are summarized in table.5.2.

In K_{e3} only the λ_+ parameter can be determined due to the small mass of the positron. The averaged value of λ_+ obtained in K_{e3} is $\lambda_+ = 0.0286 \pm 0.0022$. The λ_+ obtained by present experiment is consistent with the value obtained in K_{e3}.

5.2 Comparison with the theory

The values of form factor in $K_{\mu 3}$ is sensitive to the renormalized phenomenological coupling constants L_5 and L_9 of CHPT(Table 1.1, 1.2). They provide a severe test for the theory of CHPT. To compare with the prediction of CHPT has two means. One is whether the effective coupling constant is correct or not. The other is whether the CHPT framework to predict the observables other than those included as inputs is correct or not.

5.2.1 Vector form factor

In the space-like interval $\sqrt{-t} < 350 MeV$, the low-energy representation is applicable and the form factor λ_+ is approximated as

$$f_+(t) = f_+(0) \left\{ 1 + \frac{1}{6} <r^2>_V^{K\pi} t + \cdots \right\} \tag{5.1}$$

where $<r^2>_V^{K\pi}$ is a charge radius of kaon in the vector coupling of $K_{\mu 3}$ decay and $t = (p' - p)^2 = (p_l + p_\nu)^2$.

The charge radius is given as follows.

$$<r^2>_V^{K\pi} = <r^2>_V^\pi - \frac{1}{64\pi^2 F^2} \left\{ 3h_1 \left(\frac{M_\pi^2}{M_K^2} \right) + 3h_1 \left(\frac{M_\eta^2}{M_K^2} \right) \right.$$
$$\left. + \frac{5}{2} ln \left(\frac{M_\pi^2}{M_K^2} \right) + \frac{3}{2} ln \left(\frac{M_\eta^2}{M_K^2} \right) - 6 \right\} \tag{5.2}$$

where

$$< r^2 >_V^\pi = \frac{12 L_9}{F^2} - \frac{1}{32\pi^2 F^2} \left\{ 2ln\frac{M_\pi^2}{\mu^2} + ln\frac{M_K^2}{\mu^2} + 3 \right\} \tag{5.3}$$

$$h_1(x) = \frac{1}{2} \frac{(x^3 - 3x^2 - 3x + 1)}{(x-1)^3} ln\ x + \frac{1}{2} \left(\frac{x+1}{x-1} \right)^2 - \frac{1}{3} \tag{5.4}$$

$< r^2 >_V^\pi$ in the above expression is a charge radius of pion in the vector coupling of pion decay. To evaluate $f_+(t)$ numerically, the measured charge radius of the pion and the renormalized phenomenological coupling constant L_9 are used as inputs. The obtained prediction is

$$\lambda_+ = \frac{1}{6} M_{\pi+}^2 < r^2 >_V^{K\pi} = 0.031. \tag{5.5}$$

The measured value of λ_+ in present experiment result is good agreement with this theoretical prediction.

5.2.2 Scalar form factor

In the physical region of K_{l3} decay the low-energy representation for the scalar form factor is approximated as

$$f_0(t) = f_0(0) \left\{ 1 + \frac{1}{6} < r^2 >_S^{K\pi} t + \cdots \right\}. \tag{5.6}$$

For the slope $< r^2 >_S^{K\pi}$, which is a charge radius of kaon in the scalar coupling of $K_{\mu3}$ decay, one obtains

$$< r^2 >_S^{K\pi} = \frac{6}{M_k^2 - M_\pi^2} \left(\frac{F_K}{F_\pi} - 1 \right) + \delta_2 + O(\hat{m}, m_s)$$

$$\delta_2 = -\frac{1}{192\pi^2 F^2} \left\{ 15 h_2 \left(\frac{M_\pi^2}{M_K^2} \right) + \frac{19 M_K^2 + 3 M_\eta^2}{M_K^2 + M_\eta^2} h_2 \left(\frac{M_\eta^2}{M_K^2} \right) - 18 \right\} \tag{5.7}$$

where

$$h_2(x) = \frac{3}{2} \left(\frac{1+x}{1-x} \right)^2 + \frac{3x(1+x)}{(1-x)^3} ln\ x,$$

$$h_2(x) = h_2 \left(\frac{1}{x} \right), h_2(1) = 1,$$

$$\hat{m} = \frac{(m_u + m_d)}{2}, \tag{5.8}$$

F_K and $F\pi$ is the decay constants of kaon and pion respectively, and F is the decay constant in the case that the pion mass is assumed to be zero.

Algebraically, the correction δ_2 is of the same order in the low-energy expansion as the term involving $F_K/F_\pi - 1$. Numerically, the correction is however small, i.e. δ_2 reduces the prediction only 11%. With $F_K/F_\pi = 1.22 \pm 0.01$ the low-energy theorem implies

$$< r^2 >_S^{K\pi} = 0.20 \pm 0.05 \, fm^2$$
$$\lambda_0 = \frac{1}{6} M_{\pi+}^2 < r^2 >_S^{K\pi} = 0.017 \pm 0.004 \tag{5.9}$$

where the error is an estimate of the uncertainties due to higher order contributions.

On the other side, converting the values of λ_+ and $\xi(0)$ in the result of present experiment, the experimental value of λ_0 was obtained as

$$\lambda_0^{exp} = 0.002 \pm 0.014(sta) \pm 0.021(sys).$$

Combining the systematic error and the statistic error under the assumption that they were independent, the obtained value and the prediction seem to agree with each other within one standard deviation.

Chapter 6

Conclusion

In conclusion, we measured kinematical distribution of $K_{\mu3}$ from stopped K^+ decay using a CsI(Tl) photon detector system and a large aperture spectrometer of Toroidal magnet. The data were analyzed based on the Dalitz plot spectrum analysis in order to obtain the values of form factor of $K_{\mu3}$ decay. The experimental obtained form factors of $K_{\mu3}$ is as follows,

$$\lambda_+ = 0.034 \pm 0.007(sta) \pm 0.012(sys),$$

and

$$\xi(0) = -0.40 \pm 0.08(sta) \pm 0.07(sys),$$

where sta means a statistical error and sys a systematic error. These values are the most precise one in comparison with the previous experiments.

The obtained values of the form factors are consistent with the results of previous experiments and the prediction of Chiral Perturbation Theory.

Bibliography

[Ank73] C.Ankenbrandt et al., Phys. Rev. Lett. 28, 1472 (1973).

[Aok94] M. Aoki, et al., Phys. Rev. D 50, 69 (1994)

[Arn74] C.L. Arnold, et al., Phys. Rev. D9, 1221 (1974).

[Bra73] H.Braun, et al., Phys. Lett. 47B, 185 (1973).

[Cal66] C.Callan and S.Trieman, Phys. Rev. Lett. 16, 153 (1966) 153.

[Chi72] I-H.Chiang et al., Phys. Rev. D6, 1254 (1972).

[Com83] E.D. Commins and P.H. Bucksbaum, in "Weak interactions of leptons and quarks", 192 (Cambridge 1983)

[Daf95] L. Maiani, G. Pancheri, and N. Paver, "The Second DAFNE Physics Handbook" (1995).

[Dem96] D.V. Dementyev, Nucl. Instr. and Method 379 499 (1996).

[Don74] G. Donaldson el al., Phys. Rev. D 9 (1974) 2690.

[Don89] J.F. Donoghue and B.R. Holstein, Phys. Rev. D 40 (1989) 3700.

[Fey58] R.P. Feynman and M. Gell-Mann, Phys. Rev. 109, 193 (1958). 1681 (1957). Rev. 105, 1415 (1957).

[Gas85] J. Gasser, and H. Leutwyler, Nucl. Phys. B 250 (1985) 465, 517. Rev. 109, 1017 (1958).

[Hai72] D.Haidt et al., Phys. Rev. D3, 10 (1971).

[Ima89] J. Imazato et al., Proc. 11th Int. Conf. on Magnet Technology, August, 1989, Tsukuba, Japan

[Iva97] A.P. Ivashkin, Nucl. Instr. and Method to be published

[Jod86] A. Jodidio, et al., Phys. Rev. D 34, 1967 (1986)

[Kag95] A. Kaga, Master's Thesis, Kanagawa University, 1995.

[Kud92] Y. Kudenko and J. Imazato, KEK-report 92-15 (1992).

[Lee56] T.D. Lee and C.N. Yang, Phys. Rev. 104, 254 (1956).

[Mac62] S.W. Mac Dowell, Annals of Physics, 18, 171 (1962)

[Mer74] S. Merlan, et al., Phys. Rev. D9, 107 (1974).

[Pai57] A. Pais and S. Treiman, Phys. Rev. 105, 1616 (1957).

[Par96] Particle Data Group, Phys. Rev. **D54**, Review of Particle Physics, p.409 and 410.

[PS92] KEK−PS users guide book (1992).

[Sha90] E.P. Shabalin, Sov. J. Nucl. Phys. 51 (1990) 296

[Tan95] K.H. Tanaka, et al., Nucl. Instr. and Method 363, 114 (1995).

[Tos93] Vector Fields Limited, "TOSCA REFERENCE MANUAL", 1993.

[Yok94] T. Yokoi, Master's Thesis, Ibaraki University, 1994.

[Whi80] R. Whitman, et al., Phys. Rev. D21, 652 (1980).

[Wu57] C.S. Wu, et al., Phys. Rev. 105, 1413 (1957).

Acknowledgments

Kodak Color Control Patches

Blue Cyan Green Yellow Red Magenta White 3/Color Black
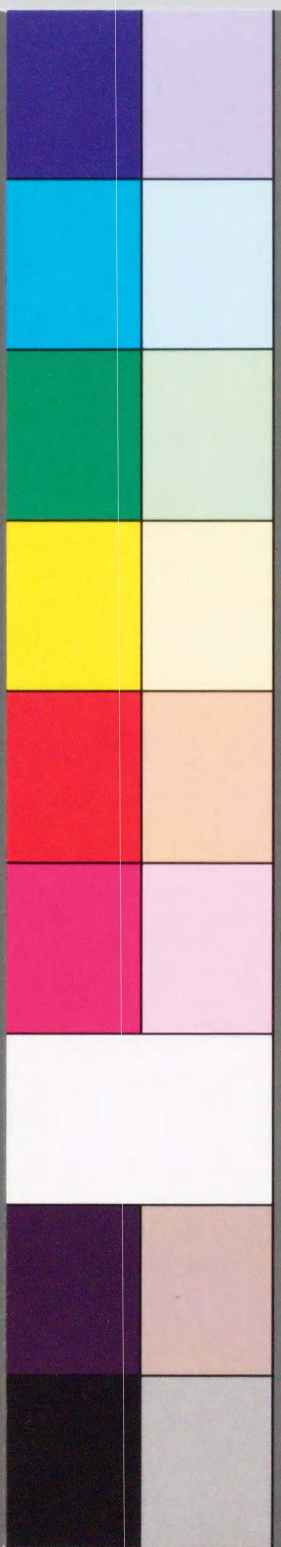
© Kodak, 2007 TM: Kodak

Kodak Gray Scale

A 1 2 3 4 5 6 M 8 9 10 11 12 13 14 15 B 17 18 19

© Kodak, 2007 TM: Kodak

C Y M